SPACECRAFT FORMATION FLIGHT
EXPLOITING POTENTIAL FIELDS

by

Edmund Mun-Choong Kong

B.E., Mechanical and Space Engineering (Hons)
University of Queensland, 1995

S.M., Aeronautics and Astronautics
Massachusetts Institute of Technology, 1999

SUBMITTED TO THE DEPARTMENT OF AERONAUTICS AND ASTRONAUTICS
IN PARTIAL FULFILLMENT OF THE DEGREE OF

DOCTORATE OF PHILOSOPHY

at the

MASSACHUSETTS INSTITUTE OF TECHNOLOGY

February 2002

Signature of Author..
Department of Aeronautics and Astronautics
January 31, 2002

Certified by ....
Associate Professor David Miller
Thesis Committee Chairman

Certified by ....
Professor Daniel Hastings
Thesis Committee Member

Certified by ....
Associate Professor Eric Feron
Thesis Committee Member

Certified by ....
Dr. Raymond Sedwick
Thesis Committee Member

Accepted by ....
Professor Wallace E. Vander Velde
Chair, Committee on Graduate Students

SPACECRAFT FORMATION FLIGHT
EXPLOITING POTENTIAL FIELDS

by

Edmund Mun-Choong Kong

Submitted to the Department of Aeronautics and Astronautics
on January 31, 2002 in Partial Fulfillment of the
Requirements for the Degree of Doctorate of Philosophy
at the Massachusetts Institute of Technology

ABSTRACT

The potential benefits that can be reaped from a distributed satellite system have led to the proposal of several multi-spacecraft missions by both NASA and DoD. One such benefit is the reconfigurability of these multi-spacecraft systems. This ultimately led to additional requirements being levied onto these missions, such as the general astrophysical imaging requirement for the Terrestrial Planet Finder (TPF) mission. Cluster reconfiguration, however, is an effort extensive operation. In this thesis, the operation of multi-spacecraft systems in three different potential fields are exploited such that spacecraft formation can be held with as little effort as possible. The first potential field considered is the Earth's gravitational field. Based upon the sparse aperture radar requirements, the terminal conditions required to keep the Air Force TechSat 21 Earth orbiting clusters in closed formations were derived. Using the Linear Quadratic formulation, the optimal reconfigurations required to initialize and resize the clusters were then determined. Based upon the current system design, the results show that both these maneuvers can be accomplished in as little as half an orbital period with the resizing maneuver costing at least 25% of the budgeted ΔV. The second potential field considered is the operation of a multi-spacecraft interferometer operating in a gravitational free environment. In this case, the optimal trajectories were determined from a combination of the science requirements, being framed as part of the cost function, and the required electrical energy. Based upon the proposed scientific plan, the interferometer that is primarily designed for planet detection should be able to meet its imaging requirement of 1000 images with only 26% of the allocated resources. The final potential field exploited in this thesis is the operation of the TPF interferometer in a self-induced electromagnetic field. Using only electromagnets to control spacecraft formation, this Electromagnetic Formation Flight (EMFF) concept requires no propellant, thus eliminating all pollution and contamination issues that are associated with it. In terms of mass fractions, power demands and volume requirements, the EMFF design is in fact comparable to the currently designed propulsion-based system. To further demonstrate the viability of the EMFF concept, controllability issues for the systems were also investigated.

Thesis Supervisor:
Assoc. Prof. David W. Miller
Dept. of Aeronautics and Astronautics

ACKNOWLEDGMENTS

Here is my opportunity to acknowledge some of those who made this work possible:

Prof. David Miller, for not only giving me the opportunity to work on a wide range of very interesting topics, but also for his advise and guidance over the last five years; Dr. Raymond Sedwick, for his continuos accessibility, advise and most importantly, his friendship; Prof. Daniel Hastings and Prof. Eric Feron, for their time, interest and input to this research; and Prof. Wallace Vander Velde, Prof. Manuel Martinez-Sanchez, Prof. Jonathan How and Prof. Olivier de Weck for slogging through this document.

My friends in the Lab for making life more interesting; especially Cyrus Jilla, who started off being my lab mate, then office mate and now gym mate and apartment mate; and of course the support staff in the Lab, for all their help throughout my stay here.

My mother, father and sister, who have always been there for me and their never ending love.

And of most of all, my girlfriend Amanda Cheng, who has been a great friend and soul mate over the last few years. Without you, this journey would have been very lonely.

NOMENCLATURE

Abbreviations

AFRL	Air Force Research Laboratory
LQ	Linear Quadratic
NASA	National Aeronautics and Space Administration
SVD	Singular Value Decomposition
TPF	Terrestrial Planet Finder

Symbols

A	Area
A_m	Current to cross-sectional area limit for coil
B	Baseline
B_s	Core magnetic flux
C	Distance measure
C_w	Battery specific mass
D	Aperture diameter
E	Energy
EE	Encircle Energy
F	Force
H	Hamiltonian function
H_m	Applied magnetic field
I_{sp}	Specific impulse
J	Cost function (Chapters 2, 3 & 4)
J	Mission efficiency (Chapter 5)
J_a	Augmented cost
M	Number of time steps (Chapters 2, 3 & 4)
M	Number of spacecraft (Chapter 5)
N	Number of spacecraft (Chapters 2, 3 & 4)
N	Number of poles (Chapter 5)
N_s	Number of states
Q	Number of imaging locations
P	Electrical power
P_{sa}	Solar array power
P_w	Specific solar array power
R_e	Earth's radius
T	Torque
a	Acceleration (Chapter 3)
a	Imaging weight (Chapter 4)
a	Coil/Core diameter (Chapter 5)
g	Integrated cost
g_e	Earth's gravity

h	Terminal cost
i	Current
i_{ref}	Reference orbit inclination
l	Half core/coil length
m	Surface terminal condition
$\dot{m}$	Mass flow rate
m_{coil}	Coil mass
m_o	Spacecraft mass without propulsion subsystem
m_{sa}	Solar array mass
m_{sc}	Spacecraft mass
m_{Tot}	Total mass
n	Orbital frequency (Chapter 3)
n	Number of turns (Chapter 5)
p_c	Conductor resistivity
q	Charge
r	Conductor radius
r_o	Projected circle radius
r_{ref}	Reference orbit radius
s	Spacecraft separation
t	Time
u	Control variable
u, v	Image plane variables (Chapter 4)
v	Vector components
x, y, z	Spacecraft position
ΔV	Velocity change
Σ	Relative mission efficiency
$\alpha, \beta, \gamma, \delta, \theta$	Angles
α	Core/Coil aspect ratio (Chapter 5)
β	Applied magnetic field (Chapter 5)
χ	Relative susceptibility
δ	Variation
ε	Quaternion variable
η	Efficiency
λ	Wavelength
μ	Gravitation constant (Chapter 3)
μ_a	Applied magnetic moment
μ_o	Permeability constant ($4\pi \times 10^{-7}$ H/m)
ρ_c	Coil density
ρ_s	Core density
ω	Rotation rate

Matrices and Vectors

A	Linear dynamic matrix
AF	Array Factor
B	Linear control matrix

C	Controllability matrix
$\overrightarrow{\mathrm{F}_{mN,\,mn}}$	Force vector
H	Hamiltonian matrix
I	Identity matrix
$\mathbf{I}_{p,m}$	Principal moment of inertia matrix
I	Intensity map
Q	State multiplier matrix in LQ framework
$R(\text{-})$	Rotation matrix
R	Control multiplier matrix in LQ framework
U	Orthogonal matrix in SVD structure
V	Orthogonal matrix in SVD structure
a	General dynamic vector
f	General function
m	Surface terminal condition vector
p	Co-state vector
r	General terminal condition vector
$\overrightarrow{\mathrm{r}_{mN,\,mn}}$	Position vector
$\mathbf{s}_m$	State and co-state solution vector at m-th time step
u	Control vector
v	Vectors
x	State vector
Σ	Diagonal matrix in SVD structure
φ	State transition matrix

Subscripts and Superscipts

$(\text{-})^{*}$	extremal
$(\text{-})^{T}$	transpose
$(\text{-})_{o}$	Initial time or state
$(\text{-})_{opt}$	Optimal
$(\text{-})_{f}$	Terminal time or state

Chapter 1

INTRODUCTION

1.1 Motivation

The potential benefits that can be reaped from a distributed satellite system have led to the proposal of several multi-spacecraft missions, such as NASA's Terrestrial Planet Finder (TPF) and the Air Force TechSat 21 missions. This distribution concept, borrowed initially from the computing industry, can offer significant improvements in the overall system's reliability, angular resolution and reconfigurability when compared to their single monolith counterpart. With inherent redundancies added through the use of multi-spacecraft systems, failure of a spacecraft in a large constellation does not automatically cripple the entire system. Angular resolutions that are not possible with a single monolith, can now be easily achieved with the use of smaller spacecraft placed far apart. Last, but not least, the capability to reconfigure the array to meet the changes in mission requirements make these multi-spacecraft systems much more desirable.

Due to budgetary constraints for large space missions, additional mission or science requirements have been levied upon some of the currently proposed missions to increase their desirability. For example, the TPF mission, originally proposed to detect Earth-like planets around nearby extrasolar systems, has been given the additional requirement to obtain images of stellar objects as well. In the case of the TechSat 21 mission, a geolocation requirement to quickly locate lost pilots has been added to its original mission of detecting slow ground moving targets. The task to meet these additional requirements can in fact be very challenging, especially with systems that were designed specifically for the original set of requirements.

However, in both these missions, the ability to reconfigure the array makes it possible for these current system designs to meet these new requirements. For the TechSat 21 mission, increasing the size of the array from its original configuration is the solution to meet the geolocation requirement. As for the TPF mission, the collector spacecraft can now be moved to various locations in the imaging plane to collect star light measurements that can then be used to reconstruct the image of the targeted object.

Holding and reconfiguring cluster formation is expensive in terms of the resources required. Traditional analyses have considered a propellant expenditure metric since it corresponds to the lifetime of the system. With the emergence of high specific impulse propulsion systems, the electrical energy required to operate these electrical thrusters must also be considered so that the power subsystem can be appropriately sized. This then determines the propulsion related masses, thus resources, required to reconfigure the cluster.

Instead of expending precious resources to hold the spacecraft formation, the potential fields that the clusters are operating in can be exploited. For Earth orbiting clusters, orbital dynamics that result from the Earth's gravitation field can be exploited to keep spacecraft formation with little or no effort. Previous studies have found effort free elliptical trajectories that will keep the clusters in closed formations without expending resources. The goal is then to determine the best method to place these clusters onto these ellipses.

For clusters operating outside of a potential field, a propulsion system is required to reconfigure the clusters. Traditionally, propellant-based systems have been considered. The limitation with these systems is that the lifetime of the mission is directly dependent on the available propellant. An alternative is to consider the Electromagnetic Formation Flight (EMFF) concept where the relative orientations of the spacecraft are controlled with only a renewable source of energy: electrical energy. Even though this concept is inadequate in terms of controlling the spacecraft absolute orientations, of importance is the control of relative spacecraft orientations.

To ensure that the science requirements for the various multi-spacecraft systems are met with the least amount of resources, the optimal reconfigurations for these spacecraft must be determined. Where possible, the different potential fields are exploited for spacecraft formation flight. In the next section, the objectives and the approach taken in this thesis is presented.

1.2 Research Objectives and Approach

The overall objective of this thesis is to systematically analyze the ability of multi-spacecraft systems to meet the science requirements given the limited resources available to them. To achieve this overall objective, the following objectives must be considered:

- Determine the framework to determine the trajectories for multi-spacecraft systems;
- Understand and formulate the science or mission requirements into the chosen framework;
- Demonstrate the proposed methodology on currently proposed missions;
- Determine the viability of the proposed systems to meet the given requirements.

To analyze the capability of these multi-spacecraft systems to meet the given requirements, it is important to determine the framework in which the analysis can be carried out. When considering reconfigurable systems, such as TPF and TechSat 21, it makes sense to consider the optimal control framework that has been applied to the trajectory determination for single spacecraft systems. Control metrics, such as propellant expenditure or consumption of electrical energy, are still important to evaluate the system's effectiveness in achieving the mission requirements. Though a little more complicated due to the multiple entities, a number of tools that have been developed in the optimal control framework can be readily applied to this study. As an example, the Linear Quadratic (LQ) controller can be used to determine the trajectories for a system with linear dynamics and quadratic cost function.

To determine the effectiveness of a multi-spacecraft system, the science requirements of the mission must seriously be considered. For single spacecraft systems, the mission or science requirements often reside in the design of the onboard payloads and therefore, can be independent factors when trajectories based on control metrics are considered. However, for multi-spacecraft systems, such as TechSat 21, the geolocation requirement levied on the system requires the coordination of all the spacecraft in the cluster. As such, understanding the science requirements for a multi-spacecraft system is that much more important. To ensure that the optimal trajectories obtained do in fact capture the given requirements, the science requirements must be formulated into the framework considered in this thesis.

To demonstrate the capability of the proposed framework to achieve the overall thesis objective, the framework is applied to two currently proposed multi-spacecraft missions: the Air Force Tech-
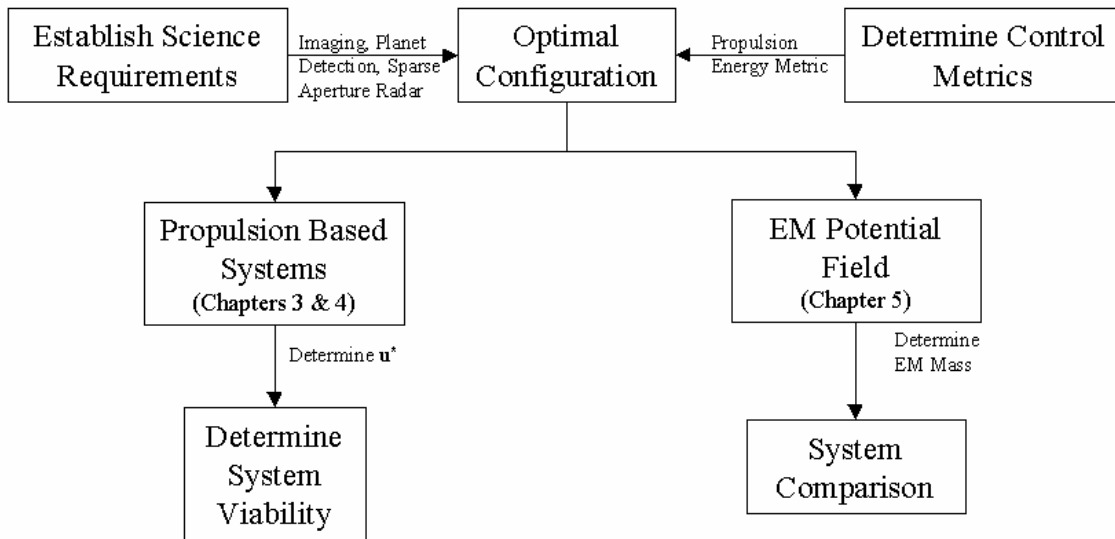
Figure 1.1 Research Approach.

Sat 21 and NASA's TPF missions. Using representative parameters from these missions, the trajectories required to transfer the array as levied by the science or mission requirements are determined. As such, the trajectories obtained here are no longer based only on the traditional control metrics, but also on the science metrics.

Finally, the obtained results are then systematically analyzed to determine the viability of the proposed systems to achieve the mission requirements. Trade studies balancing both the control and science metrics for the various missions are presented with options to maximize the returns of these systems.

The approach taken to meet the objectives of thesis can be summarized by the flow diagram shown in Figure 1.1. First, the science requirements for the multi-spacecraft system are determined. Together with control metrics, the optimal configuration is then determined. For propellant-based systems, this optimal configuration corresponds to the set of optimal controls required to reconfigure the spacecraft. From these controls, the propellant related mass can then be determined, thus the overall system mass. The obtained results are then compared to the current system designs to determine the viability of these proposed systems to meet the given science requirements.

1.3 Literature Review

Review of the literature reveals that trajectory optimization and control work for multi-spacecraft systems can be divided into two groups: Earth orbiting clusters; and arrays placed outside the influence of any major gravitational pull. In this section, works that are pertinent to this research are presented. At the end of this section, it will be revealed that trajectory optimization work for multi-spacecraft systems is significantly lacking, thus motivating this research.

Formation flight work for Earth orbiting spacecraft can be traced back to the 19th century when a linearized set of equations describing the motion of a satellite about a circular reference orbit was published [Hill, 1878]. These equations, derived from a perfectly spherical Earth assumption, are commonly known as Hill equations. An important feature observed in this set of linearized equations is the cross coupling of a spacecraft's motion in the velocity and zenith directions, but not with the cross-track direction. However, they are all related by the orbital frequency of the reference orbit.

The cross coupling of the motions in the two directions, and the orbital frequency relationship, give rise to the possibility of obtaining closed trajectory solutions. Given the appropriate set of initial conditions, a spacecraft can be made to follow one of many natural periodic elliptical trajectories in the Hill frame [Kong, 1998b, Kong et al, 1999a]. The discovery of these trajectories means that the formation of a multi-spacecraft cluster can be naturally preserved without the need for thrusters. In fact, the three TechSat 21 experimental spacecraft are currently designed to operate on one of these elliptical trajectories [Martin et al, 1999]. However, the results obtained are based upon equations that were linearized with respect to a perfectly spherical Earth with no disturbances.

The next largest effect that must be considered in describing the motion of a spacecraft around the Earth is the J_2 effect [Sedwick et al, 1999, Schaub et al, 1999]. This effect is a direct consequence of the Earth's oblateness around the equator. Incorporating this J_2 effect into the equations of motion gives rise to a secular term which causes the spacecraft in the formation to drift apart. Analysis for the TechSat 21 constellation indicates only a 0.5 m/sec/orbit of velocity change is required to counteract these secular terms.

The addition of higher order perturbations onto the Hill equations makes them a non-linear set of equations. Recognizing the existence of linear control tools and the simplicity working with a set of linear equations, the effect of the J_2 perturbation is linearized and added on to the original Hill equations [Schweighart, 2001]. The resulting set of equations are in fact constant coefficients that are dependent only on the radius and inclination of the reference orbit. Comparison with the original Hill equations results in much better prediction of the spacecraft motion except for drift errors in the cross-track direction.

Similar work was also extended to include the more general eccentric reference orbit. Using Lawden equations to describe the relative motions of spacecraft in the eccentric orbit [Lawden, 1963], the conditions required to initialize a multi-spacecraft cluster were presented by Inalhan et al, 2001. Further work by the same researchers concentrated on the development of station-keeping algorithms for nearly circular reference orbits, optimized by posing them as linear control problems [Tillerson et al, 2001]. Even in the presence of J_2 perturbation, the controller derived from the time-varying Lawden equation was acceptable, as only a velocity change of 5 - 15 mm/ sec/orbit is required to hold the spacecraft's position. However, it was also determined that the controller obtained from the time-invariant Hill equations is also adequate in rejecting disturbances while requiring significantly less computation effort. In fact, one may consider the use of the more accurate time-invariant Hill equations modified with the linearized J_2 perturbation.

More recent work in this area addressed the issue of plume impingements due to the close proximity operations of multi-spacecraft clusters [Richards et al, 2001]. Formulating the problem in a mixed integer and linear programming framework, control profiles that successfully avoid spacecraft from directly firing thrusters at each other were obtained. With this added constraint, more effort is obviously required to realize these trajectories.

The concept of using a multi-spacecraft array to image stellar objects through the principle of Michelson stellar interferometry was first proposed by Stachnik [Stachnik et al, 1984]. Due to the cheaper launch cost and shorter communication lag time, the proposed concept was to place the constellation in a low Earth orbit. Since then, a number of feasibility studies have been conducted with emphasis on finding the orbits that require minimal control effort to keep the constellation in formation [Decou, 1991, Kong et al, 1999b]. Coordination and control analysis work were also conducted for these Earth orbiting constellations [Wang et al, 1996, Wang et al, 1999].

A major obstacle that must be overcome by Earth orbiting interferometers is the relatively fast dynamics experienced by the spacecraft. Since nanometer precision control is required for visible systems, interferometers operating from an Earth orbit will require control technologies that are currently not available. As such, some missions have proposed placing these interferometers far away from any major body such that a 'gravitational free' environment is created. One of the more popular locations is the Earth trailing Lagrange point. However, locations as far out as Jupiter's orbit have also been proposed, but for a different reason [Beichman et al, 1999].

Trajectory optimization work for a two collector and one combiner spacecraft Michelson interferometer has been reported by the author in his Masters thesis [Kong, 1998a, Kong, 1998b]. Using the response of a filled aperture as a reference, the optimal imaging locations for the collectors are determined using only a small subset of the available imaging locations. Given these locations, the optimal propellant trajectories for the two spacecraft are then determined. The results compared favorably with the strawman trajectory originally designed for the DS3 interferometer [Linfield, 1997]. However, the obtained results are obviously sub-optimal since the optimal imaging locations are obtained based on the imaging metric while the trajectory optimization was performed afterwards.

In summary, literature search in the area of multi-spacecraft formation flight reveals most work has been concentrated in the area of formation control. Little trajectory planning work has been reported and only relatively simple maneuvers are considered. Even less effort has been placed on spacecraft trajectory planning that considers the science requirements of the mission. As such, this research attempts to fill this gap.

1.4 Thesis Overview

This thesis is divided into six chapters, which include both the introduction and conclusion chapters. In the next chapter, a brief overview of the framework used in this research is presented. The framework is then applied to two different missions in the following two chapters. The fifth chapter is devoted to the proposal and development of the Electromagnetic Formation Flight (EMFF) concept. The following is a brief overview of these key chapters.

	Earth Orbiting	Potential Free	EM Potential
Steady State	Closed elliptical trajectories (Kong SM Thesis)	X	**Rotating Interferometer (Chapter 5)**
Transient	**TechSat 21 Reconfigurations (Chapter 3)**	**Mapping the imaging plane (Chapter 4)**	Spin-up (Sedwick, Schweighart) / Array resizing
	Fixed Geometry Arrays	Variable Geometry Arrays	Fixed Geometry Arrays

Figure 1.2 Application Matrix.

The framework in which most of the analyses are performed is presented in Chapter 2. Even though the focus is not the development of the optimal control framework, an overview of the framework is presented to give the reader a general understanding of the approach used in this thesis. Using the calculus of variation technique, a simple LQ controller is obtained if a linearized set of dynamics and a quadratic cost function are assumed. In the various chapters, these assumptions are further scrutinized to validate the use of the simple LQ controller.

The applications of the framework to the various multi-spacecraft systems operating in the different potential fields is shown in Figure 1.2. In the matrix, steady-state operations refer to nominal operations for fixed geometry clusters. For these clusters, the size of the clusters does not actually change even though they may be rotating about a common center. Transient operations correspond to cluster reconfigurations needed to meet the different mission or science requirements. In the case of the TechSat 21 cluster, the size of the cluster must be increased to fulfill the geolocation requirement. The different studies considered in this thesis is indicated by the various chapter numbers where they are considered.

For Earth orbiting clusters, closed form elliptical trajectories, where no effort is required to maintain spacecraft formation, has determined by Kong [Kong, 1998b]. This piece of work represents the steady-state operation of these clusters. In Chapter 3, the goal is to determine the optimal reconfiguration trajectories for the spacecraft to be placed onto these effort free ellipses. Using the

Air Force Techsat 21 as the sample mission, boundary conditions specific to the requirements of Earth orbiting clusters are developed. The optimal control framework is then applied to determine the optimal reconfigurations for the multi-spacecraft cluster for two possible operational scenarios. These reconfigurations results are then used to determine the viability of the designed system to meet the specified mission requirements.

In the next chapter, the formulation is applied to a stellar imaging system operating in a 'potential free' environment. Since the stellar imaging system is not a fixed geometry cluster, the steady-state operation for this system cannot be defined. However, the reconfigurations of the apertures to maximize the science metric is considered as transient operations. In Chapter 4, a metric that penalizes both redundant and short baseline measurement is developed based upon the general characteristics of several proposed imaging metrics for multi-spacecraft interferometer. Framing this metric in the optimal control context, imaging trajectories for the multi-spacecraft interferometer are then determined. The viability of the currently designed TPF mission to meet the imposed imaging requirements is also examined.

The last potential field considered in this thesis is the self-induced Electromagnetic field as applied to a rotating multi-spacecraft interferometer. In this case, the steady-state operation is to hold the cluster formation while the spacecraft are rotating about a common center. To maintain spacecraft formation, this Electromagnetic Formation Flight (EMFF) concept uses only electrical energy, no consumables, to fully control the relative positions and orientations between the spacecraft. To present this concept, a detailed design exercise for a two spacecraft system using this EMFF concept is carried out. Extending the exercise to the five spacecraft TPF interferometer, the concept is then compared to the currently proposed propulsion-based system. Controllability issues for this EMFF concept are also investigated while laying down the ground work for future control work. Even though the optimal control framework is not used in this chapter, the possibility to determine the optimal reconfiguration (transient operations) trajectories for these spacecraft does exist and is presented for future studies.

In the conclusion chapter, a summary of the work performed in this thesis is presented. Fundamental contributions of the thesis are also presented with the support of the specific contributions from the various chapters. Finally, investigations that warrant serious consideration, such as the EMFF concept, are also presented for future undertakings.

Chapter 2

PROBLEM FORMULATION

One of the key fundamentals to the research of multi-spacecraft problems is to maximize the returns of the system given the minimal resources that are available. Be it propellant or electrical energy, the ability to minimize the use of these resources will most certainly ensure longer mission lifetime. As such, one of the key focuses of this research is to determine the optimal trajectories for these spacecraft.

Determination of optimal trajectories has been extensively researched and well documented in optimal control text books. Various methodologies, such as the calculus of variation, have been developed to solve these problems. It is not the intent of this research to determine alternate methodologies to best determine these trajectories. Rather, the optimal control framework is used to obtain these trajectories and the results will be used to systematically analyze the viability of the various missions to meet their mission requirements, thus complementing the objective of this research. As such, the theoretical development of the optimal control problem is presented in order to set the tone for the subsequent chapters.

One of the more common approaches to solving optimal control problems is the use of the calculus of variation technique. The fundamental principle behind this technique is to obtain the first variation of the optimal control problem and equate it to zero to obtain the solution. This is the very same idea used to obtain the extrema of a given function, if it is a continuous within the range of interest. Note that the outline provided here is very similar to the one in reference [Kirk, 1970].

In general, analytic solutions to these problems can be obtained only for the simplest cases. It is, therefore, common practice to resort to numerical techniques. In this research, the multiple shooting method is used to numerically determine these trajectories. A brief discussion of this technique is presented in the latter half of this chapter. The outline presented here is based on the presentation given by [Stoer et al, 1976].

2.1 Overview of Optimal Control Problem - Variational Approach

The intent of this section is to present to the reader a general understanding of the optimal control problem through the use of the Calculus of Variation technique. Theoretically, the formulation presented here can be applied to a variety of problems. In the subsequent chapters, these derivations are further scrutinized to solve the problems of interest.

The goal in solving the optimal problem is to obtain an admissible control **u*** that causes the system:

$$\dot{\mathbf{x}}(t) \;=\; \mathbf{a}(\mathbf{x}(t), \mathbf{u}(t), t) \tag{2.1}$$

to follow an admissible trajectory **x*** that minimizes the performance measure:

$$J \;=\; h(\mathbf{x}(t_f), t_f) + \int_{t_o}^{t_f} g(\mathbf{x}(t), \mathbf{u}(t), t)\,dt \tag{2.2}$$

where h is the terminal cost and g is the integrated cost. To ensure that the system dynamics constraint is not violated, the Calculus of Variation technique requires that Equation 2.1 be appended to Equation 2.2 to form the augmented cost:

$$J_a \;=\; h(\mathbf{x}(t_f), t_f) + \int_{t_o}^{t_f} \{g(\mathbf{x}(t), \mathbf{u}(t), t) + \mathbf{p}^T(t)[\mathbf{a}(\mathbf{x}(t), \mathbf{u}(t), t) - \dot{\mathbf{x}}(t)]\}\,dt \tag{2.3}$$

through the use of $\mathbf{p}^T$, the Lagrange multipliers. To simplify the notation, Kirk introduced the Hamiltonian function defined as:

$$H(\mathbf{x}(t), \mathbf{u}(t), \mathbf{p}(t), t) \equiv g(\mathbf{x}(t), \mathbf{u}(t), t) + \mathbf{p}^T(t)[\mathbf{a}(\mathbf{x}(t), \mathbf{u}(t), t)] \tag{2.4}$$

which leads to Equation 2.3 being rewritten as:

$$J_a = h(\mathbf{x}(t_f), t_f) + \int_{t_o}^{t_f} \{H(\mathbf{x}(t), \mathbf{u}(t), \mathbf{p}(t), t) - \mathbf{p}^T(t)\dot{\mathbf{x}}(t)\}dt \tag{2.5}$$

The next step in the formulation is to obtain the first variation of the augmented cost function with respect to all its dependencies ($\mathbf{x}$, $\mathbf{u}$, $\mathbf{p}$, $\dot{\mathbf{x}}$, t) and equate it to zero:

$$\delta J_a = \left[\frac{\partial}{\partial \mathbf{x}_f}h(\mathbf{x}^*(t_f), t_f)\right]^T \delta \mathbf{x}_f + \left[H(\mathbf{x}^*(t_f), \mathbf{u}^*(t_f), \mathbf{p}^*(t_f), t_f) + \frac{\partial}{\partial t}h(\mathbf{x}^*(t_f), t_f)\right]\delta t_f$$

$$+ \int_{t_o}^{t_f} \left\{ \left[\frac{\partial}{\partial \mathbf{x}}H(\mathbf{x}^*(t), \mathbf{u}^*(t), \mathbf{p}^*(t), t)\right]^T \delta \mathbf{x}(t) \right.$$

$$+ \left[\frac{\partial}{\partial \mathbf{u}}H(\mathbf{x}^*(t), \mathbf{u}^*(t), \mathbf{p}^*(t), t)\right]^T \delta \mathbf{u}(t) \tag{2.6}$$

$$\left. + \left[\frac{\partial}{\partial \mathbf{p}}H(\mathbf{x}^*(t), \mathbf{u}^*(t), \mathbf{p}^*(t), t) - \dot{\mathbf{x}}^*(t)\right]^T \delta \mathbf{p}(t) + [-\mathbf{p}^*(t)]^T \delta\dot{\mathbf{x}}(t) \right\}dt$$

$$= 0$$

where variations of the augmented cost function with respect to the initial time (t_o) and initial states are assumed to be zero. In general, this assumption is valid since the initial conditions are usually known and fixed. Also note that the variations with respect to $\mathbf{x}$ and $\dot{\mathbf{x}}$ are actually related since the latter is simply the time derivative of the former. Utilizing the integration by parts technique, the variation in $\dot{\mathbf{x}}$ shown in Equation 2.6 can be rewritten as:

$$-\int_{t_o}^{t_f} \{\mathbf{p}^{*T}(t)\delta\dot{\mathbf{x}}(t)\}dt = -\mathbf{p}^{*T}(t)\delta\mathbf{x}(t)\Big|_{t_o}^{t_f} + \int_{t_o}^{t_f} \{\dot{\mathbf{p}}^{*T}(t)\delta\mathbf{x}(t)\}dt \tag{2.7}$$

Substituting Equation 2.7 into Equation 2.6, the variation of the augmented cost can be written as:

$$\delta J_a = \left[\frac{\partial}{\partial \mathbf{x}}h(\mathbf{x}^*, t_f) - \mathbf{p}^*\right]^T \delta \mathbf{x}_f + \left[H(\mathbf{x}^*, \mathbf{u}^*, \mathbf{p}^*, t_f) + \frac{\partial}{\partial t}h(\mathbf{x}^*, t_f)\right]\delta t_f$$

$$+ \int_{t_o}^{t_f} \left\{ \left[\frac{\partial}{\partial \mathbf{x}}H(\mathbf{x}^*, \mathbf{u}^*, \mathbf{p}^*, t) + \dot{\mathbf{p}}^*\right]^T \delta \mathbf{x} + \left[\frac{\partial}{\partial \mathbf{u}}H(\mathbf{x}^*, \mathbf{u}^*, \mathbf{p}^*, t)\right]^T \delta \mathbf{u} \right.$$

$$\left. + \left[\frac{\partial}{\partial \mathbf{p}}H(\mathbf{x}^*, \mathbf{u}^*, \mathbf{p}^*, t) - \dot{\mathbf{x}}^*\right]^T \delta \mathbf{p} \right\}dt \tag{2.8}$$

$$= 0$$

where all the implicit time dependencies are dropped for compactness. Since the integral must vanish on an extremal regardless of the boundary conditions, the following necessary conditions must be satisfied:

$$
\left.\begin{aligned}
\dot{\mathbf{x}}^* &= \frac{\partial}{\partial \mathbf{p}} H(\mathbf{x}^*, \mathbf{u}^*, \mathbf{p}^*, t) \\[2mm]
\dot{\mathbf{p}}^* &= -\frac{\partial}{\partial \mathbf{x}} H(\mathbf{x}^*, \mathbf{u}^*, \mathbf{p}^*, t) \\[2mm]
0 &= \frac{\partial}{\partial \mathbf{u}} H(\mathbf{x}^*, \mathbf{u}^*, \mathbf{p}^*, t)
\end{aligned}\right\}
\qquad
\begin{aligned}
&\textit{for all} \\
&t \in [t_o, t_f]
\end{aligned}
\tag{2.9}
$$

As the variation of the augmented cost must equate to zero at the extremal, the terminal condition must also be satisfied:

$$
\left[\frac{\partial}{\partial \mathbf{x}} h(\mathbf{x}^*, t_f) - \mathbf{p}^* \right]^T \delta \mathbf{x}_f + \left[H(\mathbf{x}^*, \mathbf{u}^*, \mathbf{p}^*, t_f) + \frac{\partial}{\partial t} h(\mathbf{x}^*, t_f) \right] \delta t_f = 0
\tag{2.10}
$$

2.1.1 Necessary Conditions

The necessary conditions given in Equation 2.9 are conditions that must be satisfied on the extremal regardless of the boundary conditions. The top equation is in fact the dynamics constraint given by Equation 2.1. This is easily shown by substituting the Hamiltonian function given in Equation 2.4 into Equation 2.9. Since the integrated cost g does not depend on $\mathbf{p}$, the top equation in Equation 2.9 reduces to just the dynamic constraint. This equation is commonly known as the state equation.

The second equation in Equation 2.9 is known as the co-state equation. In general, estimating the co-states is usually the key to solving optimal control problems since they are not intuitively simple to estimate. Expanding the co-state equation in Equation 2.9 gives the following:

$$
\dot{\mathbf{p}}^* = -\left[\frac{\partial}{\partial \mathbf{x}} \mathbf{a}(\mathbf{x}^*(t), \mathbf{u}^*(t), t) \right]^T \mathbf{p}^*(t) - \frac{\partial}{\partial \mathbf{x}} g(\mathbf{x}^*(t), \mathbf{u}^*(t), t)
\tag{2.11}
$$

The third equation occurs from the fact that the variation of $\delta \mathbf{u}(t)$ is independent and it must also be equated to zero. In general, the optimal controller for the problem is obtained from this equation. The expanded version of this equation is given by:

$$0 = \frac{\partial}{\partial \mathbf{u}} g(\mathbf{x}^*(t), \mathbf{u}^*(t), t) + \left[\frac{\partial}{\partial \mathbf{u}} \mathbf{a}(\mathbf{x}^*(t), \mathbf{u}^*(t), t)\right]^T \mathbf{p}^*(t) \qquad (2.12)$$

These necessary conditions must be satisfied to obtain the solution to the optimal control problem. In cases where the admissible controls are bounded, it can be shown that only the third equation (Equation 2.12) needs to be modified.

2.1.2 Boundary Conditions

Besides satisfying the necessary conditions, Equation 2.8 requires that the boundary conditions be satisfied as well. These boundary conditions can be divided into three general conditions: the initial, intermediate and terminal conditions. A brief discussion of both these conditions are given here.

Initial Conditions

For any optimal control problem, it is reasonable to assume that the initial conditions of the states will be given. This assumption is made in the formulation of the optimal control problem outlined in this chapter. In the event that the initial conditions are not given and need to be determined, the formulation can be easily modified. In fact, this new formulation will look very similar to the free terminal condition assumption made in this formulation.

Terminal Conditions

As opposed to the fixed initial condition assumption made in this formulation, the terminal conditions have yet to be specified. In fact, the free terminal condition assumption made thus far requires that the condition in Equation 2.10 be satisfied. In the case where the variations of the terminal states are independent of the terminal time, Equation 2.10 can be separated into the following two conditions:

$$\frac{\partial}{\partial \mathbf{x}} h(\mathbf{x}^*, t_f) - \mathbf{p}^* = 0$$

$$H(\mathbf{x}^*, \mathbf{u}^*, \mathbf{p}^*, t_f) + \frac{\partial}{\partial t} h(\mathbf{x}^*, t_f) = 0$$

$$(2.13)$$

where both have to be satisfied. If the final state is specified, the variation in the final state ($\delta \mathbf{x}_f$) is therefore zero, which results in the top terminal condition in Equation 2.13 being ignored. The

same is true for problems with their terminal times (t_f) being specified. In this case, the bottom terminal condition is ignored. This second terminal condition is commonly known as the transversality condition.

The derivation of other terminal conditions that are encountered in optimal control problems can be found in Kirk, 1970. As a reference, these terminal conditions are tabulated in Table 2.1. One of the terminal conditions that is utilized in this thesis is the third terminal condition in the table. Formulation of this fixed terminal time while requiring the terminal states to lie on a surface is further discussed in Chapter 3, when the initialization and geolocation problems for the TechSat 21 mission are explored.

Intermediate Conditions

Another class of boundary condition that will be explored is the intermediate boundary condition. In this case, the cost designated as the terminal cost (h) depends not only on the terminal states but also on specific intermediate states. As such, variations of this cost (h) with respect to all the intermediate states must be obtained. Note that the necessary conditions derived in Equation 2.9 no longer hold true over the entire trajectory but over segments between points where this new cost is being evaluated. An example of a problem where such conditions exist is the determination of optimal imaging locations for a separated spacecraft interferometer. This problem is considered in Chapter 4.

2.2 LQ Formulation

The formulation of the optimal control problem in the previous section only assumes that the dynamics and the cost of the system are functions of the states, controls and time. There is, however, no assumption made as to what these dependencies are. To simplify the problem, a linear dynamic and quadratic cost system (LQ) is assumed. These assumptions are generally valid as it is common practice to linearize complicated dynamics while assuming a quadratic control cost for spacecraft equipped with electrical propulsion systems. The rest of this section is devoted to reducing the necessary conditions given in Equation 2.9 to the LQ formulation.

TABLE 2.1 Summary of Boundary Conditions in Optimal Control Problems [Kirk, 1970].

Problem	Description	Substitution in Eq. 2.10	Boundary-condition equations	Remarks
t_f fixed	1. $\mathbf{x}(t_f) = \mathbf{x}_f$ specified final state	$\delta\mathbf{x}_f = \delta\mathbf{x}(t_f) = 0$ $\delta t_f = 0$	$\mathbf{x}^*(t_o) = \mathbf{x}_o$ $\mathbf{x}^*(t_f) = \mathbf{x}_f$	$2n$ equations to determine $2n$ constants of integration
	2. $\mathbf{x}(t_f)$ free	$\delta\mathbf{x}_f = \delta\mathbf{x}(t_f)$ $\delta t_f = 0$	$\mathbf{x}^*(t_o) = \mathbf{x}_o$ $\dfrac{\partial}{\partial\mathbf{x}}h(\mathbf{x}^*(t_f)) - \mathbf{p}^*(t_f) = 0$	$2n$ equations to determine $2n$ constants of integration
	3. $\mathbf{x}(t_f)$ on the surface $\mathbf{m}(\mathbf{x}(t)) = 0$	$\delta\mathbf{x}_f = \delta\mathbf{x}(t_f)$ $\delta t_f = 0$	$\mathbf{x}^*(t_o) = \mathbf{x}_o$ $\dfrac{\partial}{\partial\mathbf{x}}h(\mathbf{x}^*(t_f)) - \mathbf{p}^*(t_f) = \displaystyle\sum_{i=1}^{k} d_i\left[\dfrac{\partial m_i}{\partial\mathbf{x}}(\mathbf{x}^*(t_f))\right]$ $\mathbf{m}(\mathbf{x}(t_f)) = 0$	$(2n+k)$ equations to determine the $2n$ constants of integration and the variables $d_1, \ldots, d_k$
t_f free	4. $\mathbf{x}(t_f) = \mathbf{x}_f$ specified final state	$\delta\mathbf{x}_f = 0$	$\mathbf{x}^*(t_o) = \mathbf{x}_o$ $\mathbf{x}^*(t_f) = \mathbf{x}_f$ $H(\mathbf{x}^*(t_f), \mathbf{u}^*(t_f), \mathbf{p}^*(t_f), t_f) + \dfrac{\partial}{\partial t}h(\mathbf{x}^*(t_f), t_f) = 0$	$(2n+1)$ equations to determine the $2n$ constants of integration and t_f
	5. $\mathbf{x}(t_f)$ free		$\mathbf{x}^*(t_o) = \mathbf{x}_o$ $\dfrac{\partial}{\partial\mathbf{x}}h(\mathbf{x}^*(t_f), t_f) - \mathbf{p}^*(t_f) = 0$ $H(\mathbf{x}^*(t_f), \mathbf{u}^*(t_f), \mathbf{p}^*(t_f), t_f) + \dfrac{\partial}{\partial t}h(\mathbf{x}^*(t_f), t_f) = 0$	$(2n+1)$ equations to determine the $2n$ constants of integration and t_f
	6. $\mathbf{x}(t_f)$ on the moving point $\theta(t)$	$\delta\mathbf{x} = \left[\dfrac{d\theta}{dt}(t_f)\right]\delta t_f$	$\mathbf{x}^*(t_o) = \mathbf{x}_o$ $\mathbf{x}^*(t_f) = \theta(t_f)$ $H(\mathbf{x}^*(t_f), \mathbf{u}^*(t_f), \mathbf{p}^*(t_f), t_f) + \dfrac{\partial}{\partial t}h(\mathbf{x}^*(t_f), t_f)$ $+ \left[\dfrac{\partial h}{\partial\mathbf{x}}(\mathbf{x}^*(t_f), t_f) - \mathbf{p}^*(t_f)\right]^T\left[\dfrac{d\theta}{dt}(t_f)\right] = 0$	$(2n+1)$ equations to determine the $2n$ constants of integration and t_f
	7. $\mathbf{x}(t_f)$ on the surface $\mathbf{m}(\mathbf{x}(t)) = 0$		$\mathbf{x}^*(t_o) = \mathbf{x}_o$ $\dfrac{\partial}{\partial\mathbf{x}}h(\mathbf{x}^*(t_f), t_f) - \mathbf{p}^*(t_f) = \displaystyle\sum_{i=1}^{k} d_i\left[\dfrac{\partial m_i}{\partial\mathbf{x}}(\mathbf{x}^*(t_f))\right]$ $\mathbf{m}(\mathbf{x}(t_f)) = 0$ $H(\mathbf{x}^*(t_f), \mathbf{u}^*(t_f), \mathbf{p}^*(t_f), t_f) + \dfrac{\partial}{\partial t}h(\mathbf{x}^*(t_f), t_f) = 0$	$(2n+k+1)$ equations to determine the $2n$ constants of integration and the variables $d_1, \ldots, d_k$ and t_f
	8. $\mathbf{x}(t_f)$ on the moving surface $\mathbf{m}(\mathbf{x}(t),t) = 0$		$\mathbf{x}^*(t_o) = \mathbf{x}_o$ $\dfrac{\partial}{\partial\mathbf{x}}h(\mathbf{x}^*(t_f), t_f) - \mathbf{p}^*(t_f) = \displaystyle\sum_{i=1}^{k} d_i\left[\dfrac{\partial m_i}{\partial\mathbf{x}}(\mathbf{x}^*(t_f))\right]$ $\mathbf{m}(\mathbf{x}(t_f)) = 0$ $H(\mathbf{x}^*(t_f), \mathbf{u}^*(t_f), \mathbf{p}^*(t_f), t_f) + \dfrac{\partial}{\partial t}h(\mathbf{x}^*(t_f), t_f)$ $= \displaystyle\sum_{i=1}^{k} d_i\left[\dfrac{\partial m_i}{\partial t}(\mathbf{x}^*(t_f), t_f)\right]$	$(2n+k+1)$ equations to determine the $2n$ constants of integration and the variables $d_1, \ldots, d_k$ and t_f

2.2.1 Linear Dynamics

Most rigid body dynamics can be represented by a simple linear dynamic system. This usually simplifies the optimal control problem at hand. In the case of an Earth orbiting system, a modified linearized set of Hill's equations is used (Chapter 3). For a localized distributed imaging system located in a heliocentric orbit, a rigid body dynamic relationship that depends only on the thruster firings is considered (Chapter 4). In general, the dynamics for these linear systems can be written in the following form:

$$\dot{\mathbf{x}} = \mathbf{A}\mathbf{x}(t) + \mathbf{B}\mathbf{u}(t) \tag{2.14}$$

where the time derivative of the states is just simple linear combinations of the state and control variables.

2.2.2 Cost function (Quadratic Cost)

Formulation

In general, the electrical power required to operate a given set of electrical thruster is given by [Sutton, 1992]:

$$\begin{aligned} P &= \frac{F^2}{2\dot{m}\eta} \\ &= \frac{m_{sc}^2 u^2}{2\dot{m}\eta} \end{aligned} \tag{2.15}$$

where m is the mass of the spacecraft, $\dot{m}$ is the propellant mass flow rate and η is the thruster efficiency. This equation assumes a constant spacecraft mass over the entire trajectory as little propellant is consumed. As an example, the total mass of a TechSat 21 spacecraft is currently budgeted at 129.4 kg, of which only 8.2 kg is the propellant mass for the electric Hall thrusters. To further emphasize this point, the typical value for the propellant mass flow rate is 0.74 mg/s, which is insignificant compared to the total spacecraft mass.

Since the electrical power required for the thrusters is quadratic with respect to the control effort, u, one can therefore formulate the problem in terms of the well known Linear Quadratic (LQ) framework. In the LQ framework, the integrated cost can be rewritten as:

$$g(\mathbf{x}(t), \mathbf{u}(t), t) = \mathbf{x}^T(t)\mathbf{Q}\mathbf{x}(t) + \mathbf{u}^T(t)\mathbf{R}\mathbf{u}(t) \qquad (2.16)$$

where the $\mathbf{Q}$ matrix is assumed to be semi-positive definite, while $\mathbf{R}$, a positive definite matrix. Since the goal of the thesis is determine optimal trajectories in terms of the required control effort, the matrix $\mathbf{Q}$ in Equation 2.16 is set to zero in the subsequent derivations.

Justification

The quadratic cost considered in this optimal control formulation must be justified. The cost given by Equation 2.15 is in fact the total electrical energy required to operate the thrusters. For fixed time problems, problems considered in this thesis, minimizing with respect to the total electrical energy is equivalent to minimizing the average power required for the maneuver. Hence, the cost justification can also be discussed in terms of the average power required for the propulsion subsystem.

The propellant mass for a given maneuver can be obtained by first re-writing Equation 2.15 as follows:

$$P = \frac{\dot{m}}{2\eta}(I_{sp}g_e)^2 \qquad (2.17)$$

where I_{sp} is the specific impulse of the propulsion system and g_e is the Earth's gravity. For fixed specific impulse system, the propellant mass required can then be obtained by integrating the propellant mass flow rate over the entire trajectory:

$$\begin{aligned} m_{prop} &= \int_{t_o}^{t_f} \dot{m}dt \\ &= \frac{2\eta}{(I_{sp}g)^2}P_{avg}(t_f - t_o) \end{aligned} \qquad (2.18)$$

which turns out to be a linear function of the average power required for the propulsion subsystem. Since the average power for a fixed time problem is equivalent to the total energy required, minimizing with respect to the energy required for the thrusters is in fact minimizing the propellant required for the thrusters, thus the resources required.
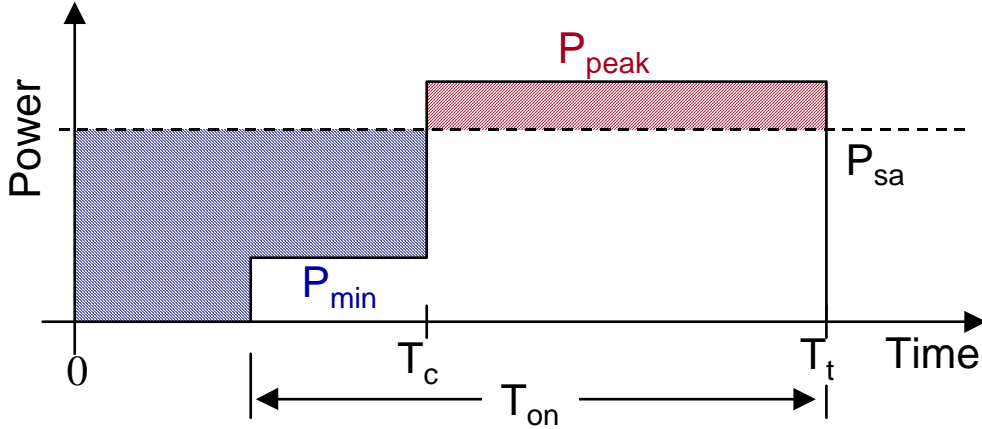
Figure 2.1   Sample power profile required for propulsion subsystem.

Since electrical thrusters are high specific impulse systems, little propellant is usually required. In fact, one has to also consider the corresponding power subsystem masses that are required to operate the thrusters. Consider the mass breakdown of a spacecraft in terms of the propulsion related masses and all other masses on the spacecraft (m_o):

$$m_{sc} = m_o + m_{prop} + m_{sa} + m_{batt}$$

(2.19)

where m_{prop}, m_{sa} and m_{batt} are the propulsion related masses that correspond to the propellant, solar array and battery. This formulation assumes that a certain power level (P_{sa}) is provided by the solar array panels while additional power is to be supplied by the batteries. Consider the power profile shown in Figure 2.1. In this profile, when the power demand is below the solar array power (from 0 to T_c), the battery is charged so that the peak power demand can be met when it is required (from T_c to T_t). Designing to solar arrays to provide an average power of P_{sa}, the required solar array mass is:

$$m_{sa} = \frac{P_{sa}}{P_w}$$

(2.20)

where P_w is the specific mass of the solar array panels (W/kg). The corresponding battery mass can then be expressed as:

$$m_{batt} = \frac{P_{avg}T_{on} - P_{min}(T_c - T_t + T_{on}) - P_{sa}(T_t - T_c)}{C_w}$$

(2.21)

where C_w is the specific mass of the battery given in terms of W.hr/kg. As all the parameters in these two equations can be explicitly determined for a particular power profile, the goal is then to determine the minimum combination of solar array and battery masses by determining the solar array power. Based upon these two equations only, the minimum mass answer is to provide zero solar array power since negative masses are not allowed. However, the energy provided by the solar array panel over the considered interval must at least meet the overall electrical energy required to operate the thrusters:

$$P_{avg}T_{on} \leq P_{sa}T_t \tag{2.22}$$

Hence, to minimize the power subsystem masses that are related to propulsion, the goal is to minimize the power provided by the solar array panels. However, to ensure that the power subsystem can in fact provide the power required to realize the maneuver, the solar array panels must be designed to at least meet the thruster energy requirements. Since the minimum power subsystem mass design is a linear function of the average power required for the thrusters, minimizing the total energy is in fact minimizing all the propulsion related masses, thus justifying the quadratic cost used in this formulation.

2.2.3 LQ Controller

The necessary conditions that result from the LQ framework can be obtained by substituting Equations 2.14 and 2.16 into Equation 2.9:

$$
\begin{aligned}
\dot{\mathbf{x}}^* &= \mathbf{A}\mathbf{x}^* + \mathbf{B}\mathbf{u}^* \\
\dot{\mathbf{p}}^* &= -\mathbf{A}^T\mathbf{p}^* \\
\mathbf{u}^* &= -\mathbf{R}^{-1}\mathbf{B}^T\mathbf{p}^*
\end{aligned}
\tag{2.23}
$$

where the matrix $\mathbf{Q}$ is set to zero. Since this optimal LQ controller is a linear combination of only the co-states, one can rewrite both the state and the co-state equations in terms of their own variables. Combining the two equations into a matrix form, the following first order differential equation is obtained:

$$\frac{d}{dt}\begin{bmatrix} \mathbf{x}^* \\ \mathbf{p}^* \end{bmatrix} = \begin{bmatrix} \mathbf{A} & -\mathbf{B}\mathbf{R}^{-1}\mathbf{B}^T \\ 0 & -\mathbf{A}^T \end{bmatrix}\begin{bmatrix} \mathbf{x}^* \\ \mathbf{p}^* \end{bmatrix} \tag{2.24}$$

$$= \mathbf{H}\tilde{\mathbf{x}}^*$$

where $\tilde{\mathbf{x}}^*$ represents both the state and the co-state variables, and the matrix $\mathbf{H}$ is known as the Hamiltonian matrix. From control theory, this linear differential equation has the solution in the form of:

$$\tilde{\mathbf{x}}^*(t_2) = \varphi(t_2,t_1)\tilde{\mathbf{x}}^*(t_1) \tag{2.25}$$

where $\varphi(t_2,t_1)$ is known as the state transition matrix. Since the system considered here is dependent only on their own variables, the state transition matrix can be represented by the matrix exponential:

$$\varphi(t_2,t_1) = e^{\mathbf{H}(t_2 - t_1)} \tag{2.26}$$

that can be easily calculated. In cases when the necessary conditions cannot be reduced to a linear first order differential equation (Equation 2.24), one needs to integrate both the state and co-state differential equations. In general, this integration cannot be carried out analytically due to the complex nature of the control law. Numerical integration is required, though this operation is extremely computation expensive.

Unless the problem is very simple, it is generally not possible to obtain analytical solutions to optimal control problems. As such, numerical techniques are normally used to determine the optimal trajectories. In the next section, the multiple shooting numerical method is presented.

2.3 Numerical Techniques

The key components required to solve the optimal trajectory problem have been presented in Section 2.1. Obtaining analytical solutions to optimal trajectory problems is almost impossible especially for problems involving a large number of states. In this section, the multiple shooting numerical algorithm used to determine these minimum energy trajectories is briefly described. A more complete description of the numerical method can be found in reference [Stoer et al, 1976].

The task at hand calls for solving a system of differential equations such that the optimal trajectory can be determined. In general, one can always numerically integrate the equations as long as all the initial conditions are specified. In the N spacecraft problem, only half of the required $12N$ initial conditions are specified since none of the initial conditions for the co-states are given. Instead, specified are the $6N$ initial and $6N$ terminal conditions. Such problems are commonly referred to as two point boundary value problems.

A two point boundary value problem can be solved using a simple shooting method where one guesses the missing initial conditions and then integrates the differential equations to obtain the terminal states. These terminal states are then used to determine the missing initial conditions through Newton's method, and the process is iterated until the specified terminal conditions are met. This simple shooting method is, however, quite numerically unstable, especially for problems with a large number of states and long integration times $(t_f - t_o)$. This is largely due to the fact that small errors occur in guessing the initial conditions may translate to large errors in the terminal states due to long integration times.

An alternative is to consider the multiple shooting method. This method divides the trajectory into M time steps and the states and co-states at all the time steps are determined numerically subject to the state dynamics:

$$\dot{\mathbf{x}} = \mathbf{f}(\mathbf{x},t) \tag{2.27}$$

and the boundary conditions:

$$\mathbf{r}[\mathbf{x}(t_o), \mathbf{x}(t_f)] = 0 \tag{2.28}$$

which, in this problem, is a $12N$ column vector. By defining $\mathbf{s}_m$ as the vector of solution at the m-th point on the trajectory, the problem is now to determine these $\mathbf{s}_m$ vectors in such a way that the function:

$$\mathbf{x}(t) = \mathbf{x}(t;t_m, \mathbf{s}_m) \qquad \textit{for } \mathbf{x} \in [\mathbf{x}_m, \mathbf{x}_{m+1})$$
$$m = 1, 2, ..., M-1 \tag{2.29}$$
$$\mathbf{x}(t_f) = \mathbf{s}_M$$
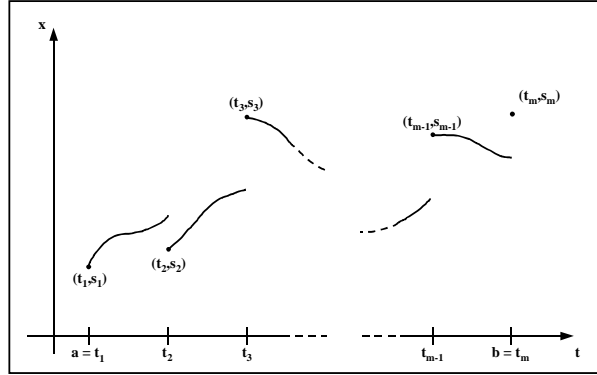
Figure 2.2 Multiple shooting method [Stoer et al, 1976].

when pieced together, is continuous, and thus a solution of the differential equation in Equation 2.27. In addition, the solution must also satisfy the boundary condition given by Equation 2.28. An illustration of the method is shown in Figure 2.2.

Instead of the original $12N$ boundary conditions, the problem now yields the following $12NM$ conditions:

$$
\mathbf{F}(\mathbf{s}) = \begin{bmatrix}
\mathbf{x}(t_2; t_1, \mathbf{s}_1) - \mathbf{s}_2 \\
\mathbf{x}(t_3; t_2, \mathbf{s}_2) - \mathbf{s}_3 \\
\dots \\
\mathbf{x}(t_M; t_{M-1}, \mathbf{s}_{M-1}) - \mathbf{s}_M \\
\mathbf{r}(\mathbf{s}_1, \mathbf{s}_M)
\end{bmatrix} = 0 \tag{2.30}
$$

and the unknowns that are to be determined:

$$
\mathbf{s} = \begin{bmatrix} \mathbf{s}_1 & \dots & \mathbf{s}_M \end{bmatrix}^T \tag{2.31}
$$

This problem can now be solved iteratively using Newton's method:

$$
\mathbf{s}^{(i+1)} = \mathbf{s}^{(i)} - [\mathbf{DF}(\mathbf{s}^{(i)})]^{-1} \mathbf{F}(\mathbf{s}^{(i)}) \tag{2.32}
$$

where $\mathbf{DF}(\mathbf{s})$ is a $12NM$ x $12NM$ Jacobian matrix which has the form:

$$\mathbf{DF(s)} = \begin{bmatrix} \mathbf{G}_1 & -\mathbf{I} & 0 & & 0 \\ 0 & \mathbf{G}_2 & -\mathbf{I} & \ldots & \\ & \ldots & \ldots & \ldots & 0 \\ 0 & & \ldots & \mathbf{G}_{M-1} & -\mathbf{I} \\ \mathbf{P} & 0 & & 0 & \mathbf{Q} \end{bmatrix} \tag{2.33}$$

and the $\mathbf{P}$, $\mathbf{Q}$ and $\mathbf{G}_k$ matrices are given by:

$$\mathbf{G}_m \equiv D_{s_m} \mathbf{x}(t_{m+1}; t_m, \mathbf{s}_m)$$

$$\mathbf{P} \equiv D_{s_1} \mathbf{r}(\mathbf{s}_1, \mathbf{s}_m) \tag{2.34}$$

$$\mathbf{Q} \equiv D_{s_M} \mathbf{r}(\mathbf{s}_1, \mathbf{s}_M)$$

Compared with the simple shooting method, the multiple shooting method is much more computationally expensive. At every iteration, one has to perform M numerical integrations, and in situations where $\mathbf{G}_m$ cannot be analytically determined, an additional $12N(M - 1)$ integrations must be executed. Fortunately, in cases where the future states of the system are simply a linear combination of the initial states of the system, the matrices $\mathbf{G}_m$ are simply the matrix exponential shown in Equation 2.26, if equal time steps are chosen.

As for the $\mathbf{P}$ matrix, one can show that it is simply an identity matrix of dimension $6N$ in the upper left corner of the $12N$ square matrix. The simple $\mathbf{P}$ matrix results from the fact that the dependency of the $\mathbf{r}$ vector with respect to variables $\mathbf{s}_1$ is linear when all the initial states are given. Depending on how the terminal conditions are specified, the $\mathbf{Q}$ matrix can be either as simple as the $\mathbf{P}$ matrix or more complicated. Again, if the terminal states are specified, the $\mathbf{Q}$ matrix will simply be a $12N$ square matrix with a $6N$ identity matrix located its lower left corner. Else, if the terminal states are anything but simple, one may be required to consider numerical finite differencing methods if the $\mathbf{Q}$ matrix cannot be obtained through simple analytic differentiation.

2.4 Summary

The theoretical development using the calculus of variation technique as applied to optimal control problems has been presented in this chapter. Through the formulation, it is observed that the optimal trajectories are determined by satisfying both the necessary and boundary conditions. The formulation is then extended to consider a linear dynamic system with a quadratic cost function, such

that LQ controller is obtained. This LQ controller is used throughout this thesis to determine the results for the various missions of interest.

Since analytical solutions to the optimal control problem can only be obtained for the simplest cases, one must resort to numerical techniques and the multiple shooting technique is considered to be the most appropriate. This method requires that the trajectory be divided into small segments where the solutions to these segments, once put together, give a continuous solution. Even though this technique can potentially require high computation power, it is much more tolerant to the integration of small errors, which is paramount in obtaining numerical solutions.

In the next chapter, the optimal control framework is applied to an Earth orbiting cluster, namely the Air Force TechSat 21. Key elements, such as the dynamic and terminal conditions, specific to the mission are developed. Optimal reconfigurations for the cluster operating in two different scenarios are determined. The results are then used to determine the viability of the proposed system to achieve the mission requirements.

Chapter 3

EARTH ORBITING CLUSTERS

In this chapter, the optimal maneuvers required to change the trajectories of Earth orbiting clusters are determined. The Air Force distributed Space Based Radar mission, TechSat 21, is used as the case study. A brief overview of the mission is first presented, followed by a discussion on the dynamics used to describe the motions of the spacecraft relative to each other. Boundary conditions specific to the Earth orbiting clusters are developed with the radar requirements in mind. Two reconfiguration maneuvers are considered in this study, namely the initialization and geolocation maneuvers. The ability of the currently designed system to perform these maneuvers is also examined.

3.1 Overview of TechSat 21

TechSat 21 is a program initiated by the Air Force Research Laboratory (AFRL) to explore the basic technologies required to enable a Distributed Satellite System (DSS) [Martin et al, 1999]. For this purpose, a Space Based Radar (SBR) mission is selected as a reference mission to identify the technology required to realize such a system and to allow for an easy comparison with conventional approaches. To provide global coverage with minimal outages, a total of 35 clusters of 8 satellites placed in 7 orbital planes at 800 km altitude is currently envisioned. Current program schedules for an operational system by the year 2010.

Before committing to launching the entire system, the AFRL has scheduled a flight experiment involving a cluster of three spacecraft. Since it is only a flight experiment, the capabilities of these spacecraft are reduced compared to the full TechSat 21TechSat 21 spacecraft. As an example, the

individual mass of these spacecraft is currently designed at 129.4 kg as opposed to a sub-100 kg TechSat 21 spacecraft. Also, the flight experiment spacecraft are to be placed in a nominal cluster size of 500 m at an altitude of 600 km, instead of 800 km.

3.2 Orbital Dynamics

3.2.1 Hill Equations

To analyze the motions of satellites in a cluster, it is useful to treat their local movements as perturbations about some reference orbit. This linearization is quite accurate since the size of the cluster is usually very small compared to the radius of the reference orbit. If the reference is circular, the resulting linearized set of equations are simply Hill equations [Hill, 1878]:

$$
\begin{aligned}
\ddot{x} - 2n\dot{y} - 3n^2 x &= a_x \\
\ddot{y} + 2n\dot{x} &= a_y \\
\ddot{z} + n^2 z &= a_z
\end{aligned}
\tag{3.1}
$$

where n is the frequency of the reference orbit in radians per second, and the acceleration terms on the right account for all non-central force effects (drag, thrust, etc.). The coordination has been chosen so that the x-axis points up, the y-axis is parallel to the velocity vector in the reference orbit and the z-axis completes the right-handed system. An illustration of this local coordinate system is shown in Figure 3.1.

If the terms on the right hand side are set to zero, the resulting set of differential equations can be solved to get the free orbit motion given by [Sedwick et al, 1998]:

$$
\begin{aligned}
x &= A_o \cos(nt + \alpha) + x_{offset} \\
y &= -2A_o \sin(nt + \alpha) - \frac{3}{2} n x_{offset} t + y_{offset} \\
z &= B_o \cos(nt + \beta)
\end{aligned}
\tag{3.2}
$$

where A_o and B_o have dimensions of length, and α and β are phasing angles. It can be seen that the movement along the z axis is de-coupled from the other two directions, and exhibits a simple harmonic motion. This cross track direction is in fact the inclination of the orbit relative to the reference. The coupling between the x and y equations is seen to require that (1) each satellite follows
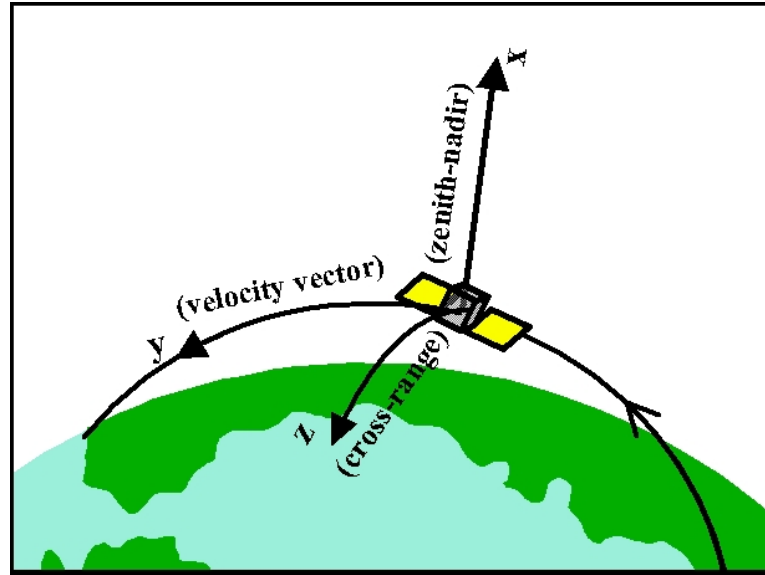
Figure 3.1 Hill's coordinate frame shown with respect to Earth.

a two-by-one ellipse in the vertical plane of motion, and (2) an offset in the positive x direction causes a drift along the negative y-axis. This second motion corresponds to the satellite being in a higher (longer period) orbit, where the velocity is lower [Sedwick et al, 1998, Kong et al, 1999a].

Since Equation 3.2 is the effort free solution to Hill equations, spacecraft that are placed onto this trajectory should theoretically remain on it indefinitely. To ensure that all the spacecraft in the cluster remain in a closed configuration, the drift effects in Equation 3.2 are eliminated by setting the offset in the x-direction to zero. The resulting trajectory simply describes an ellipse centered on the velocity vector. Figure 3.2 shows the free elliptical trajectory when the substitution of $B_o =$ $-2A_o$ is made.

Optimal trajectories for both the initialization and geolocation problems using the linearized Hill equations for the TechSat 21 mission have already been presented in [Kong et al, 2000]. More recently, however, a more accurate model of the linearized spacecraft dynamics that incorporates the non-linear J_2 effect has been developed. In the next subsection, these modified Hill equations are presented.
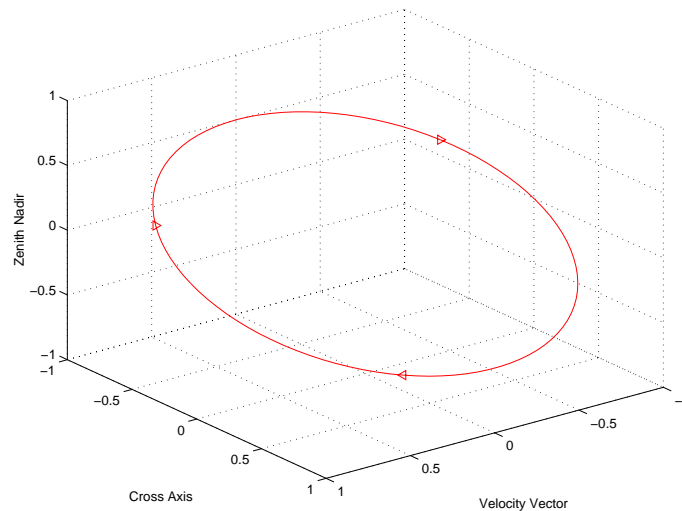
Figure 3.2   Free elliptical trajectory in Hill's frame of reference.

3.2.2 Modified Hill's Equations

The original Hill equations are based upon the premise that the Earth is a perfect sphere. This, however, is not true. Depending upon the altitude of the spacecraft, the largest non-linear perturbation to this perfectly spherical Earth theory is the bulging effect seen around Earth's equator. This non-linear perturbation is commonly known as the J_2 effect. Even though the J_2 effect may be very small compared to the altitude of the spacecraft or the size of the earth, in its local environment, this effect may be significant. Perturbation on the order of meters may not matter when compared to the hundreds or thousands of kilometers scale of the spacecraft altitude, it is quite significant when one is describing spacecraft formation flight in the hundreds of meters scale. To accurately capture this effect, the spacecraft trajectories in this thesis will be determined based upon these modified Hill equations. Full derivation of these equations can be found in reference [Schweighart, 2001]. For the purpose of this research, only the key equations will be presented.

The modified Hill equations, which looks quite similar to original Hill equations (Equation 3.1) are given by:

$$\ddot{x} - 2(nc)\dot{y} - (5c^2 - 2)n^2 x = a_x$$
$$\ddot{y} + 2(nc)\dot{x} = a_y \qquad (3.3)$$
$$\ddot{z} + k^2 z = a_z$$

where the s, c and k terms are given by:

$$s = \frac{3J_2 R_e^2}{8r_{ref}^2}[1 + 3\cos(2i_{ref})]$$
$$c = \sqrt{1+s} \qquad (3.4)$$
$$k = n\sqrt{1+s} + \frac{3nJ_2 R_e^2}{2r_{ref}^2}[\cos(i_{ref})]^2$$

In this equation, i_{ref} corresponds to the reference orbit's inclination and r_{ref} is the spacecraft radial distance from the center of the Earth. Comparison between this new set of equations and the Hill equations indicates an increase in oscillation frequency in all three axes. The frequency increase is the same in both the x and y directions, but different in the z direction. Note that when the value of J_2 is set to zero, Equation 3.3 simply reduces to Equation 3.1.

The general solution to these equations is found to be [Schweighart, 2001]:

$$x = x_o \cos(nt\sqrt{1-s}) + \frac{\sqrt{1-s}}{2\sqrt{1+s}} y_o \sin(nt\sqrt{1-s})$$
$$y = -\frac{2\sqrt{1+s}}{\sqrt{1-s}} x_o \sin(nt\sqrt{1-s}) + y_o \cos(nt\sqrt{1-s}) \qquad (3.5)$$
$$z = z_o \cos(kt) + \frac{\dot{z}_o}{k} \sin(kt)$$

where x_o, y_o, and z_o are the initial position of the spacecraft and $\dot{z}_o$ is the initial velocity of the spacecraft in the z direction. As for the initial velocities in the x and y directions, the following substitution:

$$\dot{x}_o = \frac{n y_o (1 - s)}{2} \frac{}{\sqrt{1 + s}}$$

$$\dot{y}_o = \sqrt{v_{In-plane}^2 - \dot{x}_o^2} - v_{ref} - n c x_o$$

$$v_{In-plane} = \sqrt{\frac{2\mu}{r_o} + \frac{J_2 R_e^2 \mu (1 - 3[\sin(i_o)\sin(\theta_o)]^2)}{r_o^3} - \frac{\left(1 - \frac{s}{3}\right)\mu}{r_{ref}}}$$

(3.6)

were made in Equation 3.5 to eliminate all secular motions. Based upon previous experience in using the original set of Hill equations, the following initial conditions were assumed for the cluster of spacecraft:

$$x_o = A_o, \qquad y_o = 0$$

$$z_o = -\frac{2\sqrt{1+s}}{\sqrt{1-s}} x_o, \quad \dot{z}_o = 0$$

(3.7)

which eliminates both the initial x and y velocities and reduces Equation 3.5 to:

$$x = A_o \cos(nt\sqrt{1-s})$$

$$y = -\frac{2\sqrt{1+s}}{\sqrt{1-s}} A_o \sin(nt\sqrt{1-s})$$

$$z = -\frac{2\sqrt{1+s}}{\sqrt{1-s}} A_o \cos(kt)$$

(3.8)

This equation does indeed look very similar to Equation 3.2 with zero x and y offsets, a slight difference in oscillation amplitudes in the y and z directions, and oscillation frequency in the z direction. The slight difference in oscillation amplitudes may not matter at all since it remains constant over time. However, the difference in the oscillation frequency can change the elliptical trajectory significantly. As time progresses, the elliptical trajectory described in Equation 3.2 is seen to 'tumble' at a rate of $2|k - n|$. This tumbling effect is depicted in Figure 3.3. In the early stages of the orbit, the trajectory described by the modified Hill equations (solid line) duplicates the elliptical trajectory described by original version (dotted line) (a). However, as time progresses, the two trajectories no longer match each other ((b) and (c)). The solid trajectory described in subplot (c) is actually the elliptical trajectory described in Equation 3.2 if the substitution $B_o = 2A_o$ is made instead. Finally, in subplot (d), the two trajectories match up again. This tumbling effect is the
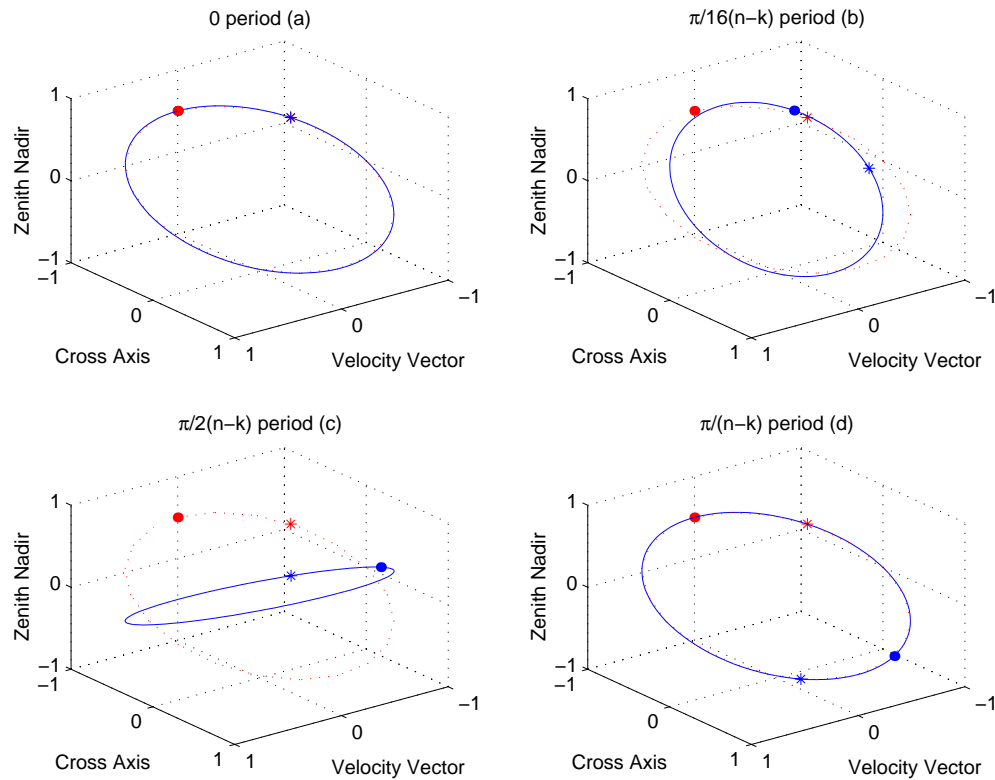
Figure 3.3 Comparison between elliptical trajectories described in Equation 3.2 (dotted) and Equation
3.8 (solid). Direction of trajectory is from the dot marker to the asterix marker.

direct result of the J_2 perturbation introduced to the original Hill equations. As such, transferring
the spacecraft to the elliptical trajectory described in Equation 3.2 will not be appropriate since the
J_2 perturbation has a drastic effect on the elliptical trajectory. To realistically determine the opti-
mal spacecraft trajectories, the trajectory described in Equation 3.8 will be used instead.

To simplify the calculation and to ensure that the system is numerically stable, it is recognized that
Equation 3.3 can be written as a function of the true anomaly (θ), using the fact that all terms in the
solution will have periods that are multiples of the orbital period. The chain rule can then be
applied to each term of Equation 3.3 by writing d/dt as $n(\mathrm{d}/\mathrm{d}\theta)$ and dividing through by n^2. As a
result, Equation 3.3 can be re-written as:

$$x_o'' - 2cy_o' - (5c^2 - 2)x_o = a_{ox}$$
$$y_o'' + 2cx_o' = a_{oy} \qquad (3.9)$$
$$z_o'' + (k/n)^2 z_o = a_{oz}$$

where a_{ox}, a_{oy} and a_{oz} are the corresponding non-central force effects.

Finally, to put the dynamics in the context of the optimal control framework, Equation 3.9 is written in state-space notation. The obvious choice for the state variables are the position and velocity components of the spacecraft. Designating **x** as the state vector, Equation 3.9 can be re-written in terms of:

$$\dot{\mathbf{x}} = \mathbf{A}\mathbf{x} + \mathbf{B}\mathbf{u} \qquad (3.10)$$

where the state and the control vectors for a spacecraft are given by:

$$\dot{\mathbf{x}} = \begin{bmatrix} x & \dot{x} & y & \dot{y} & z & \dot{z} \end{bmatrix}^T$$
$$\mathbf{u} = \begin{bmatrix} u_x & u_y & u_z \end{bmatrix}^T \qquad (3.11)$$

while the **A** and **B** matrices for the spacecraft are given by:

$$\mathbf{A} = \begin{bmatrix} 0 & 1 & 0 & 0 & 0 & 0 \\ 5c^2 - 2 & 0 & 0 & 2c & 0 & 0 \\ 0 & 0 & 0 & 1 & 0 & 0 \\ 0 & -2c & 0 & 0 & 0 & 0 \\ 0 & 0 & 0 & 0 & 0 & 1 \\ 0 & 0 & 0 & 0 & -(k/n)^2 & 0 \end{bmatrix}, \mathbf{B} = \begin{bmatrix} 0 & 0 & 0 \\ 1 & 0 & 0 \\ 0 & 0 & 0 \\ 0 & 1 & 0 \\ 0 & 0 & 0 \\ 0 & 0 & 1 \end{bmatrix} \qquad (3.12)$$

In the case of a multiple spacecraft cluster, the state vector of the system will include all the position and velocity components of all the spacecraft with the corresponding expanded dynamic matrix (**A**). Similarly, the control matrix (**B**) must also be modified to accommodate the modified control vector **u**.

3.3 Boundary Conditions

3.3.1 Initial Conditions

In most cases, the initial conditions on the states ($\mathbf{x}(t_o)$) are usually known. This, however, is not the case for the co-states. The initial conditions for the co-states are determined through numerical iterations.

3.3.2 Terminal Conditions

Single Aperture

To satisfy both the boundary conditions, the terminal conditions for the system must also be specified. The specified initial conditions will give $6N$ of the $12N$ required (N is the number of spacecraft in the cluster). For fixed terminal time problems, there exist three types of terminal conditions as tabulated in Table 2.1. However, only the fixed and surface terminal states are of interest here.

In the simple case where all the terminal states ($\mathbf{x}(t_f) = \mathbf{x}_f$) are specified, the terminal conditions for the co-states ($\mathbf{p}(t_f) = 0$) in Equation 2.8 are disregarded since all the $12N$ boundary conditions are specified. The position conditions have already been specified in Equation 3.8. However, these position conditions only constitute half of the six required for each spacecraft. The rest of the terminal conditions lie in the velocity conditions. The consequence of not specifying the terminal velocity conditions will result in the spacecraft not staying on the elliptical trajectory once the maneuver is made. These velocity conditions are obtained by taking the time derivative of Equation 3.8:

$$
\begin{aligned}
\dot{x} &= -n\sqrt{1-s}A_o\sin(nt\sqrt{1-s}) \\
\dot{y} &= -2n\sqrt{1+s}A_o\cos(nt\sqrt{1-s}) \\
\dot{z} &= \frac{2k\sqrt{1+s}}{\sqrt{1-s}}A_o\sin(kt)
\end{aligned}
\tag{3.13}
$$

which actually describes an elliptical trajectory similar to the one given by Equation 3.8, except for a 90° phase lag.

However, a more appropriate terminal condition for the cluster of spacecraft is to specify a surface condition for all the acceptable terminal states. From these terminal states, the set of states that corresponds to the minimum energy trajectory solution can be obtained. From Table 2.1, the terminal conditions that must be met are:

$$\mathbf{m}(\mathbf{x}^*(t_f)) = 0 \tag{3.14}$$

which give at most $6N - 1$ terminal conditions while the remainders are given by:

$$-\mathbf{p}^*(t_f) = \sum_{i=1}^{k} d_i \left[\frac{\partial m_i}{\partial \mathbf{x}}(\mathbf{x}^*(t_f)) \right] \tag{3.15}$$

which make a total of $6N$ terminal conditions.

The objective in both the cluster initialization and geolocation problems is to place all the spacecraft onto an effort free trajectory while requiring them to be in some sort of formation. Unlike the solution to Hill equations, Equation 3.8 do not exactly described an elliptical trajectory since oscillation frequency in the z direction is different from the other two. This slight offset, however, can be accommodated by re-writing the z component in Equation 3.8 as:

$$\begin{aligned} z &= -\frac{2\sqrt{1+s}}{\sqrt{1-s}} A_o \cos(nt\sqrt{1-s} + [k - n\sqrt{1-s}]t) \\ &\approx -\frac{2\sqrt{1+s}}{\sqrt{1-s}} A_o \cos(nt\sqrt{1-s} + \alpha_{avg}) \end{aligned} \tag{3.16}$$

where the time varying phase offset is replaced with an equivalent α_{avg} phase. With this approximation, this new trajectory will be a closed elliptical trajectory after each period. As such, the objective is to place the spacecraft with the given initial conditions onto this new elliptical trajectory.

One way to accomplish this is to specify two terminal conditions for the spacecraft: (1) the spacecraft has to be located on the ellipse and (2) the spacecraft has to be in the plane of the ellipse. To do so, however, requires that the elliptical trajectory be described in its principle coordinate system. This is achieved through a series of coordinate transformation shown in Figure 3.4. Denoting $\mathbf{v_2}$ and $\mathbf{v_3}$ as the semi-minor and semi-major axis vectors of the ellipse, the vector $\mathbf{v_1}$, which completes this principle coordinate system, can be obtained through the use of the vector cross
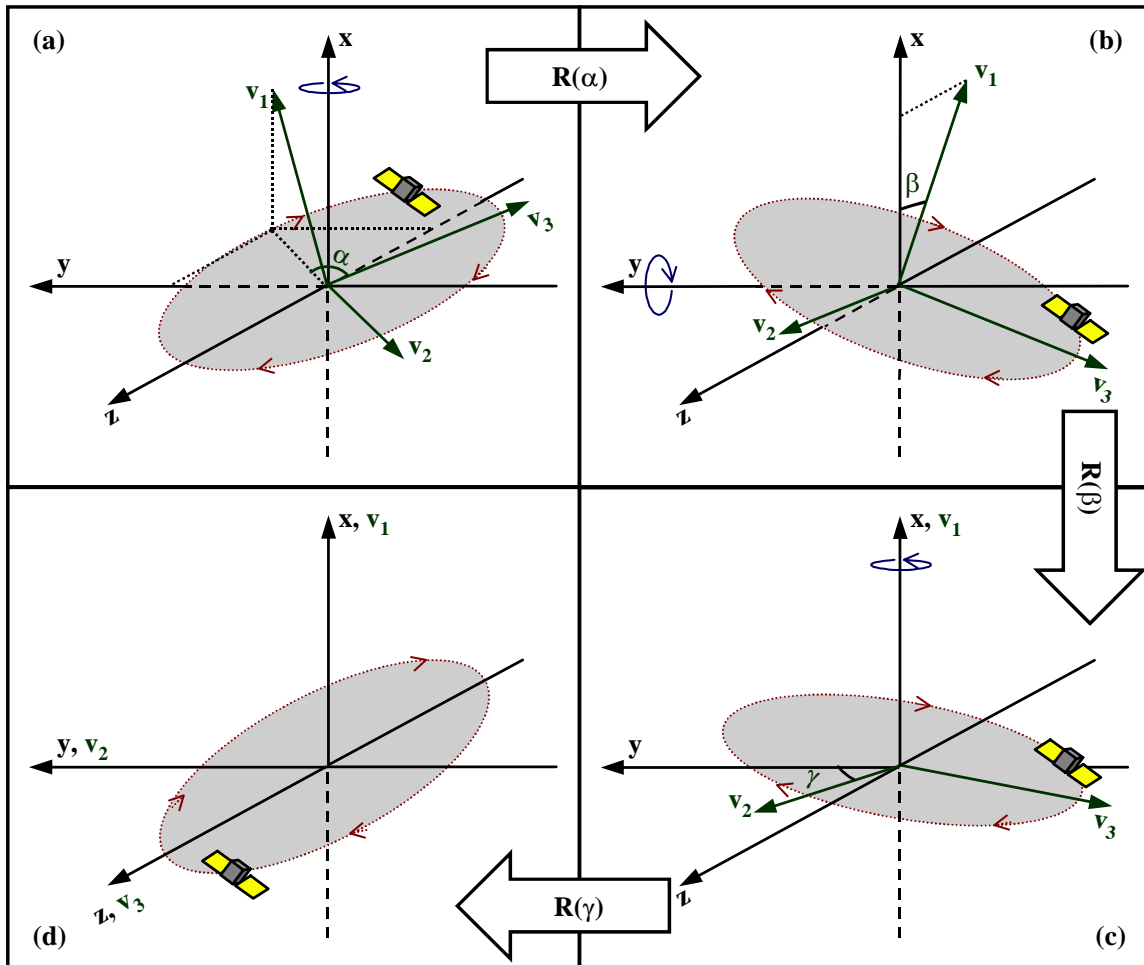
Figure 3.4   Series of rotation made to describe elliptical trajectory in its principle coordinate system.

product. From this, the first transformation is made by rotating the entire array about the global x axis by the angle α such that the vector $\mathbf{v_1}$ is now located in the x-z plane while pointed in the negative z direction (a):

$$(3.17)$$

The next transformation is to align the vector $\mathbf{v_1}$ with the global x axis (b). This is made by rotating the ellipse through an angle β about the global y axis. The corresponding rotational matrix and the angle β required for this transformation is given by:

$$R(\beta) = \begin{bmatrix} \cos\beta & 0 & \sin\beta \\ 0 & 1 & 0 \\ -\sin\beta & 0 & \cos\beta \end{bmatrix}, \qquad \beta = -\text{acos}\left(\frac{\mathbf{v}_1 \cdot \begin{bmatrix} 1 & 0 & 0 \end{bmatrix}^T}{|\mathbf{v}_1|}\right) \qquad (3.18)$$

Finally, with the ellipse already in the *y-z* plane, the third transformation is to align the semi-minor axis vector ($\mathbf{v_2}$) with the *y* axis (c):

$$R(\gamma) = \begin{bmatrix} 1 & 0 & 0 \\ 0 & \cos\gamma & \sin\gamma \\ 0 & -\sin\gamma & \cos\gamma \end{bmatrix}, \qquad \gamma = \text{atan}\left(\frac{v_{2z}^c}{v_{2y}^c}\right) \qquad (3.19)$$

The overall transformation for an ellipse described in the global *x-y-z* coordinates to its principle coordinates can then be made using the rotational matrices given in Equations 3.17, 3.18 and 3.19:

$$\begin{bmatrix} \tilde{x} \\ \tilde{y} \\ \tilde{z} \end{bmatrix} = R(\gamma)R(\beta)R(\alpha) \begin{bmatrix} x \\ y \\ z \end{bmatrix} \qquad (3.20)$$

With these transformations, the surface terminal conditions for the spacecraft can now be derived. The first two terminal conditions are dependent only on the terminal positions of the spacecraft and are given by:

$$m_1 = \tilde{x}$$
$$m_2 = (\tilde{y}/|\mathbf{v}_2|)^2 + (\tilde{z}/|\mathbf{v}_3|)^2 - 1 \qquad (3.21)$$

where these conditions are to be equated to zero. The first condition specifies that the spacecraft must be located in the plane of the ellipse ($\tilde{y}$-$\tilde{z}$ plane) while the second constrains the spacecraft to the elliptical trajectory, thus the general form of the elliptical equation. Similar to the position conditions, the velocity conditions must also be specified:

$$m_3 = \dot{\tilde{x}}$$
$$m_4 = (\dot{\tilde{y}}/n|\mathbf{v}_2|)^2 + (\dot{\tilde{z}}/n|\mathbf{v}_3|)^2 - 1 \qquad (3.22)$$

Unlike the case where all the terminal conditions are specified, meeting only the conditions given by Equations 3.21 and 3.22 is not enough. One can imagine that a particular spacecraft may be placed at one location on the position ellipse while assuming velocities corresponding to a differ-

ent location on the ellipse. Even though the respective terminal conditions are met, the spacecraft will diverge from the ellipse if the corresponding terminal velocities are not met. Hence, a fifth terminal condition is required to tie the position and velocity terminal conditions. Since the position and velocity terminal conditions are ellipses that are 90° out of phase, this fifth terminal condition can be obtained by taking the vector triple product between the position vector, the velocity vector and the unit vector perpendicular to the elliptical plane:

$$m_5 = \dot{\tilde{y}} \cdot \tilde{z} - \tilde{y} \cdot \dot{\tilde{z}} - n|\mathbf{v}_2||\mathbf{v}_3| \qquad (3.23)$$

where the positional vector is first crossed with the velocity vector. Note that even though a dot product between the two vectors can be obtained, it is also important to take into account the fact that the velocity vector lags the position vector by 90°.

The five surface conditions for the single spacecraft case that have been discussed thus far are essentially constraints placed on the spacecraft states. However, to solve the problem, one would need to specify one more terminal condition. This is given by Equation 3.15. In this one space-craft case where k is equal to five, one will need to solve for the five unknowns d_i using five of the six co-state equations and treating the remaining co-state equation as the last terminal condition. However, it is possible to reduce the six co-state equations down to the one terminal condition that is required without having to solve for the unknowns d_i. This is achieved by re-writing Equation 3.15 in a matrix format and reducing the equation down to the singular value decomposition struc-ture [Strang, 1993]:

$$-\mathbf{p}^*(t_f) = \mathbf{U}\mathbf{\Sigma}\mathbf{V}^T\mathbf{d} \qquad (3.24)$$

where $\mathbf{U}$ is 6 x 6 orthogonal matrix, Σ is 6 x 5 diagonal matrix of singular values and V is 5 x 5 orthogonal matrix. The structure of the Σ matrix is such that all the singular values are located on the diagonal of the matrix, while the last row is just a row of zeros. As such, the $\mathbf{U}$ matrix can be partitioned as:

$$-\mathbf{p}^*(t_f) = \begin{bmatrix} \mathbf{U_F} & \mathbf{U_o} \end{bmatrix} \begin{bmatrix} \Sigma_\mathbf{F} \\ 0 \end{bmatrix} \mathbf{V}^T\mathbf{d} \qquad (3.25)$$

where $\mathbf{U_F}$ is composed of the eigenvectors corresponding to the singular values of Σ_F. Now, by taking the inverse of the $\mathbf{U}$ matrix on both sides of the equation, the six co-state equations can be reduced to:

$$-\mathbf{U_o}^T \mathbf{p}^*(t_f) = 0 \tag{3.26}$$

which gives the last terminal condition that is required for the one spacecraft problem.

Multi-Spacecraft

The terminal surface conditions given by Equations 3.21, 3.22 and 3.23 will apply to each spacecraft. However, when a cluster of spacecraft is considered, it is usually desirable to phase these spacecraft in some form. This leads to additional terminal conditions.

The total number of terminal conditions that must be provided for an N spacecraft cluster is $6N$. Using the surface terminal condition method, $5N$ of these conditions are specified to ensure that the spacecraft reach the ellipse with the corresponding velocity conditions. This therefore, leaves N conditions to specify the phasing conditions for the multi-spacecraft cluster.

The simplest method to specify these conditions is to determine the phasing angles of each spacecraft based upon their locations on the ellipse. This, however, presents two major drawbacks. The first is that the order that the spacecraft are to be phased on the ellipse is inherently specified when all that matters is that the N spacecraft are phased correctly relative to each other. The second is the issue of dealing with the inverse of trigonometric operations to determine which of the two possible quadrants that the resulting angle should lie in.

There, however, exists an alternative where the distances between the spacecraft are to be considered instead. The logic behind this method is that the relative angular separations between the spacecraft can be translated to the relative distance separations if the spacecraft are located on a circle. Since it can be shown that a circular projection can always be found from an ellipse, transforming the trajectory described by Equation 3.20 through a δ rotation about the $\tilde{y}$ axis:

$$R(\delta) = \begin{bmatrix} \cos\delta & 0 & \sin\delta \\ 0 & 1 & 0 \\ -\sin\delta & 0 & \cos\delta \end{bmatrix}, \qquad \delta = \mathrm{acos}\left(\frac{v_{2y}^d}{v_{3z}^d}\right) \tag{3.27}$$

gives a circle that can be described by the new $\bar{y}$ and $\bar{z}$ coordinates of the ellipse. Since this transformation is a linear operation, the absolute angular phasing for a spacecraft in the ellipse remains the same in the circular projection, and hence the relative angular phasings as well. The advantage of specifying these angular separation in a circle is that the distance between points on the circle depends only on the relative angular separation between them regardless of where they are on the circle. As such, ensuring that the spacecraft distance separation criteria are met will ensure that the spacecraft in the cluster are correctly phased with respect to each other.

Given that the spacecraft can now be placed onto a circle, the distance between two points on a circle of radius r_o separated by an angle θ can be shown to be:

$$C_{i,j} = \sqrt{2}r_o\sqrt{1 - \cos\theta_{i,j}} \qquad (3.28)$$

where i and j represents the i-th and j-th spacecraft. Since it is only the relative angular separations that are of concern, only N - 1 phasing conditions are required. The easiest is of course to specify all the N - 1 phasing conditions with respect to the first spacecraft. Unfortunately, this may lead to incorrect solutions since correct phasings with respect to the first spacecraft do not automatically translates to the required phasing between other spacecraft. Even though the separations between spacecraft 1 with the other two spacecraft remain the same in both the subplots in Figure 3.5, separation between spacecraft 2 and 3 is different in these subplots. Clearly, the proposed phasing condition is not adequate.

The main reason that the previous method failed to specify to appropriate phasing conditions is that it only considers the relative angular separations with respect to only one spacecraft. To appropriately described the terminal conditions, all the relative angular separations must be considerd. One possibility is to take the sum of all the distances from each of the spacecraft to all the others. This will then give N phasing conditions for an N spacecraft cluster. However, since $5N$ of the $6N$ terminal conditions have already been specified, up to only N - 1 phasing conditions can be specified before the problem becomes over-constrained. As such, the first N - 1 phasing conditions are used to the determine the optimal trajectories while the last condition is used to ensure that the desired cluster configuration is indeed obtained. Mathematically stated, the N - 1 phasing conditions are given by:
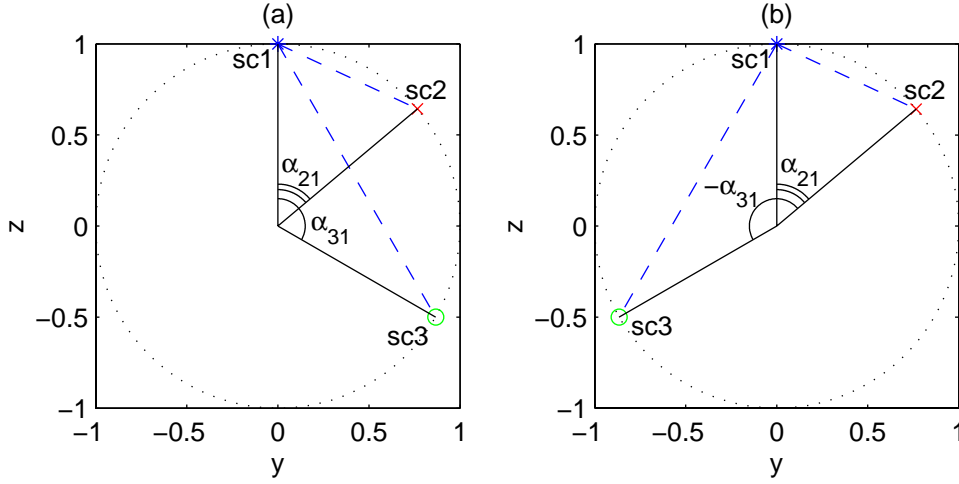
Figure 3.5   Incorrect phasing conditions for multi-spacecraft cluster.

$$m_{5N+i} = \sum_{j=1}^{N} \left| \begin{bmatrix} \bar{y} \\ \bar{z} \end{bmatrix}_i - \begin{bmatrix} \bar{y} \\ \bar{z} \end{bmatrix}_j \right| - C_i \qquad for\ i = 1, 2, \ldots, N-1 \qquad (3.29)$$

where C_i are terminal constants obtained through the desired relative angular separations, $\theta_{i,j}$:

$$C_i = \sqrt{2} r_o \sum_{j=1}^{N} \sqrt{1 - \cos \theta_{i,j}} \qquad for\ i = 1, 2, \ldots, N \qquad (3.30)$$

where the N-th constant is used to check the resulting trajectory. In specifying the phasing conditions in terms of the distances on a circle, the exact locations or phasing angles for the spacecraft in the cluster are not specified. Such phasing conditions allow the algorithm some leeway to determine the minimum energy trajectories. In the case of a five spacecraft cluster evenly phased on a circle, all the terminal constants have the same value of $6.16 r_o$.

Hence, in the case of the N spacecraft cluster, there exist 5 terminal conditions (Equations 3.21, 3.22 and 3.23) for each spacecraft which equates to $5N$ conditions. Since these spacecraft are to be phased with respect to each other, an additional N - 1 (Equation 3.29) conditions are required, which give $6N$ - 1 conditions. The remaining condition, required to ensure that the problem is well defined, is obtained through the co-state terminal condition (Equation 3.15) via Equation 3.26.

3.4 Results and Discussion

3.4.1 Mission Parameters

An experimental flight to validate the technologies required for the full TechSat 21 mission is currently scheduled for the year 2003. The current plan is to launch a cluster of three spacecraft into a 600 km circular polar orbit. Since most of the advance technologies required for the full TechSat 21 mission will not be available soon, the capabilities of these experimental spacecraft will be reduced.

To take advantage of the high specific impulse offered by electrical propulsion systems, Hall Thrusters have been selected as the spacecraft main propulsion system. It is envisioned that these spacecraft will use two large thrusters for orbit raising and de-orbit maneuvers and a system of 10 micro-thrusters for full three-axis thrust capability [Martin et al, 1999]. Interestingly enough, the total mass of the entire propulsion system is only 10 kg of the 129.4 budgeted for the spacecraft. According to [Hruby et al, 1999], the mass flow rate for the BHT-200-X2B Hall thruster is rated at 0.74 mg/s with a nominal electrical efficiency of about 42%. For normal operations, electrical power input of 200 W is required.

3.4.2 Tolerance Limit

The solutions to the optimal control problem are obtained by simultaneously equating all the $12Nm$ conditions (Equation 2.30) to zero. However, since it is not possible to obtain analytic solutions, numerical evaluation of the problem requires that a tolerance to be set. Intuitively, if a loose tolerance is set, the algorithm will require fewer number of iterations to arrive at a solution, though it may not be acceptable. Conversely, a more accurate solution can be obtained if a tighter tolerance is set, but this comes at the expense of computation power.

To determine the appropriate tolerance limit, a plot of the normalized energy required to transfer a spacecraft from the center of the Hill origin to the desired free elliptical trajectory as a function of the set tolerance limit is shown in Figure 3.6. Seen in the figure is the decreasing trend of the energy required to transfer the spacecraft. As tighter tolerances are set, the energy requirements seem to decrease. These energy requirements, however, do not decrease indefinitely, but asymptotically approach an energy level of 0.3335 units when a tolerance of at least 0.001 unit is set.
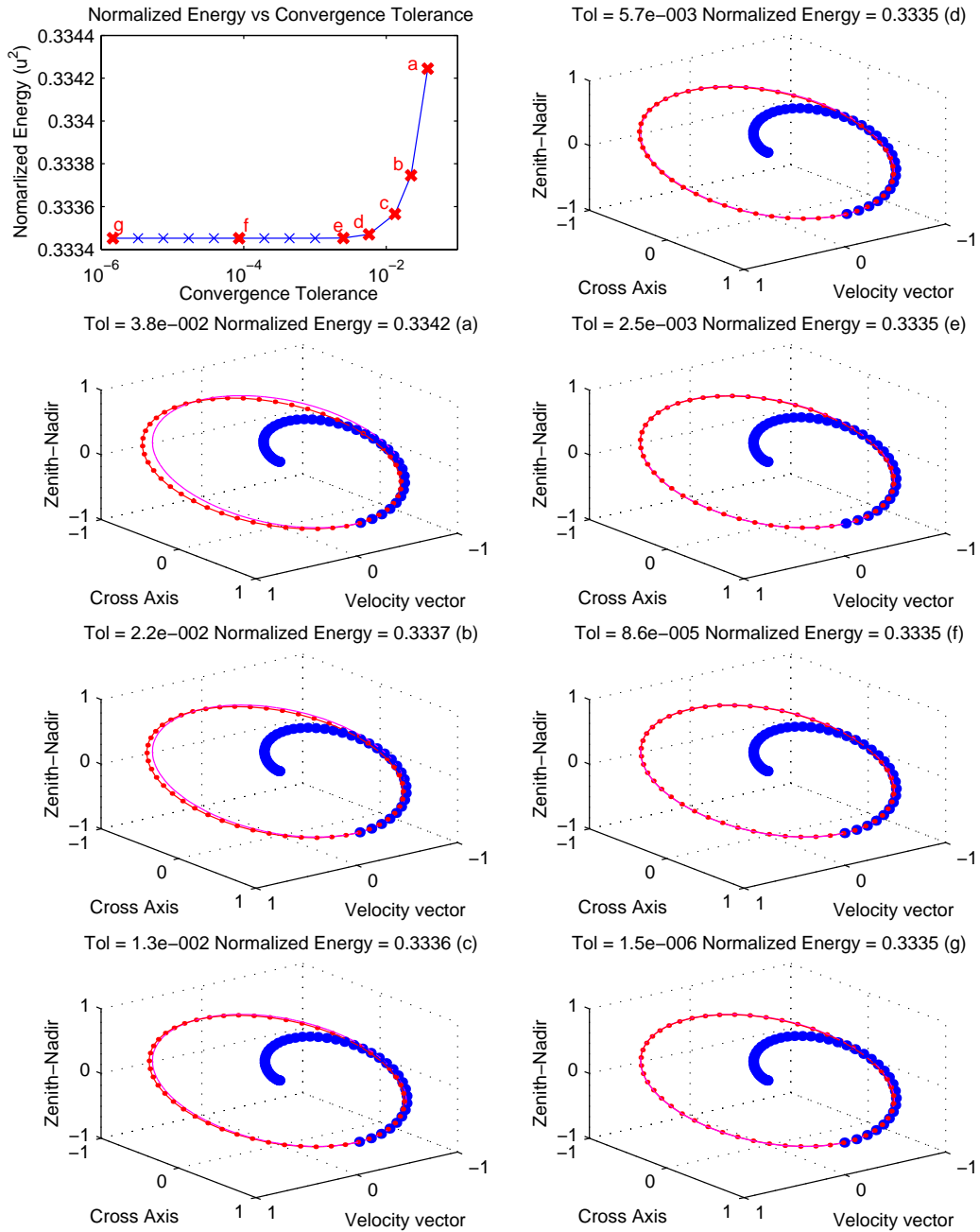
Figure 3.6   Setting of numerical tolerance for optimal trajectory solution determination.

This indicates that the solution obtained with a tolerance set at 0.001 is good enough to represent the actual solution. To further confirm this result, plots of the spacecraft trajectories obtained for the different tolerance limits are also shown. The blue curves indicate the spacecraft trajectories during the transfer period while the red curves represent the trajectories of the spacecraft beyond the transfer period. Even though all the plots indicate that the spacecraft reached the ellipse, clearly shown in plots (a) to (c) is that the spacecraft did not meet the corresponding velocity conditions required to stay on the ellipse. However, with a tighter tolerance setting, the spacecraft remains on the elliptical trajectory (plots (d) to (g)) after the initialization maneuver has taken place. As such, a tolerance of 0.001 is set for determining the controls required to transfer the cluster of spacecraft.

3.4.3 Initialization

For any given mission, it is important to accurately place the spacecraft in its desired orbit. This is especially true for multi-spacecraft missions. It is no longer adequate for each spacecraft to reach its final destination with minimum energy but they must also be correctly phased with respect to each other. As such, the objective here is to determine the minimum energy trajectories required to transfer a cluster of N spacecraft from some initial location to the free elliptical trajectory described by Equations 3.21, 3.22 and 3.23. To obtain the total energy required to initialize the cluster, the normalized energy calculated from the algorithm must be scaled by $n^3 r_o^2$ since the spacecraft acceleration, $\mathbf{u}$, is scaled by $n^2 r_o$, while the power required by the thrusters is scaled by $n^4 r_o^2$.

Single Spacecraft

The optimal transfer trajectory for a spacecraft located at the Hill origin to the free ellipse can be obtained in two different methods: (a) one can specify the specific terminal conditions that the spacecraft must achieved at every point on the elliptical trajectory and iteratively determine the minimum energy trajectory for each of these terminal points; or (b) only the position and velocity ellipses (Equations 3.21, 3.22 and 3.23) are specified such that the minimum energy trajectory is obtained. Using the first approach, a plot of the minimum energy required to initialize a spacecraft to the ellipse is shown in Figure 3.7. This curve does in fact resemble an inverted cosine wave with a frequency twice that of the orbital frequency, resulting in two minimum energy trajectories.
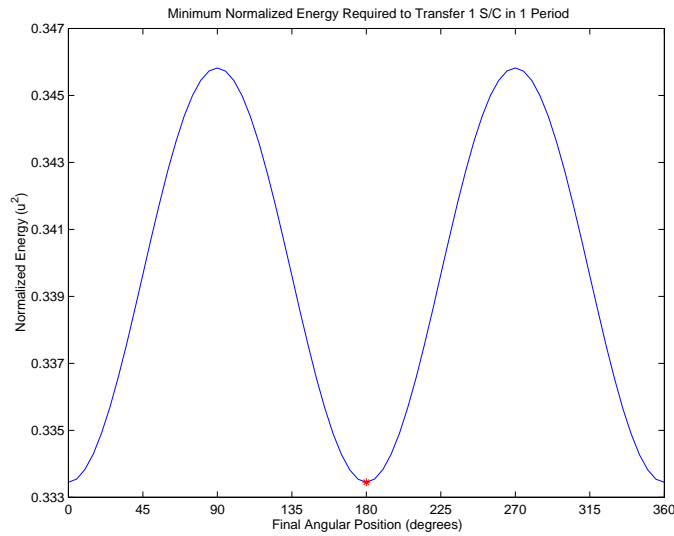
Figure 3.7 Energy required to transfer spacecraft from the origin to
free elliptical trajectory.

On this plot, these two minimum energy locations are found to be 180° apart since reversing the thrust directions for one of the minimum energy trajectory results in the other. The trajectory obtained in Figure 3.6 is shown as an asterix in the figure, which corresponds to one of the two minima. This, therefore, confirms that the results obtained using the second methodology do correspond to the minimum energy trajectory.

Further investigation shows similar sinusoidal curves when the initialization time is changed. By assuming a sinuisoidal relationship between the energy required and the initialization time in the form of:

$$E = a - b\cos(2\theta + c) \tag{3.31}$$

where θ is the angle to which the spacecraft is transferred to on the ellipse, these curves can be completely described by determining the parameters in the equation. These parameters, obtained from curve fitting the results, are tabulated in Table 3.1 for the various initialization times. In this table, the second column (variable a) refers to the average energy required to initialize a spacecraft, the third column (variable b) corresponds to the amplitude of energy required and the final column (variable c) refers to the phasing of the sinuisoidal curve. From this table, the minimum energy required to initialize a spacecraft can be obtained by subtracting the values in column b

TABLE 3.1 Minimum energy parameters as a function of initialization time.

Init. Time	a	b	c (deg)	Init. Time	a	b	c (deg)
0.1	5.62×10^1	5.05×10^0	35.1	5	6.68×10^{-2}	7.84×10^{-5}	0.7
0.2	7.68×10^0	3.26×10^{-1}	70.7	7	4.77×10^{-2}	4.49×10^{-5}	1.6
0.3	2.60×10^0	2.88×10^{-2}	111.0	10	3.34×10^{-2}	2.73×10^{-5}	2.9
0.5	8.57×10^{-1}	1.31×10^{-1}	0	20	1.66×10^{-2}	1.22×10^{-5}	7.2
0.7	5.44×10^{-1}	1.36×10^{-1}	72.1	30	1.11×10^{-2}	7.95×10^{-6}	11.3
1	3.39×10^{-1}	6.19×10^{-3}	-0.2	50	6.67×10^{-3}	4.69×10^{-6}	19.3
2	1.67×10^{-1}	6.47×10^{-4}	-0.2	70	4.77×10^{-3}	3.31×10^{-6}	27.3
3	1.11×10^{-1}	2.27×10^{-4}	0	100	3.34×10^{-3}	2.27×10^{-6}	39.3

from column a. These minimum energy trajectories can be achieved if the spacecraft terminates at phasing angles of either $\theta_{min} = -c/2$ or $\theta_{min} = -c/2 + 180°$. Also observe in the table is the general trend of decreasing average energy (column a) required to initialize a spacecraft as time is increased.

With the minimum energy trajectories required to initialize a spacecraft being determined, the next step is to determine the minimum energy trajectories required to transfer a cluster of N spacecraft. In this subsection, two different approaches will be considered with two different initialization problems. In the first problem, all the spacecraft in the cluster will be assumed to originate from the Hill origin. The results obtained for the one spacecraft case will be extended for this multi-spacecraft case. In the second problem, these spacecraft are to be initialized from a linearly distributed configuration along the velocity vector (*y*-axis). The difference between these two initialization problems are depicted in the two subplots in Figure 3.8.

Multi-spacecraft - Initialization from the origin

The energy required to transfer a spacecraft to the various points on the ellipse was determined in the previous subsection. Here, the goal is to determine the total minimum energy required to transfer the N spacecraft cluster within a specified time. As such, the total desired cost function that is to be minimized is:

$$E_T = E_1 + E_2 + \dots + E_N \tag{3.32}$$
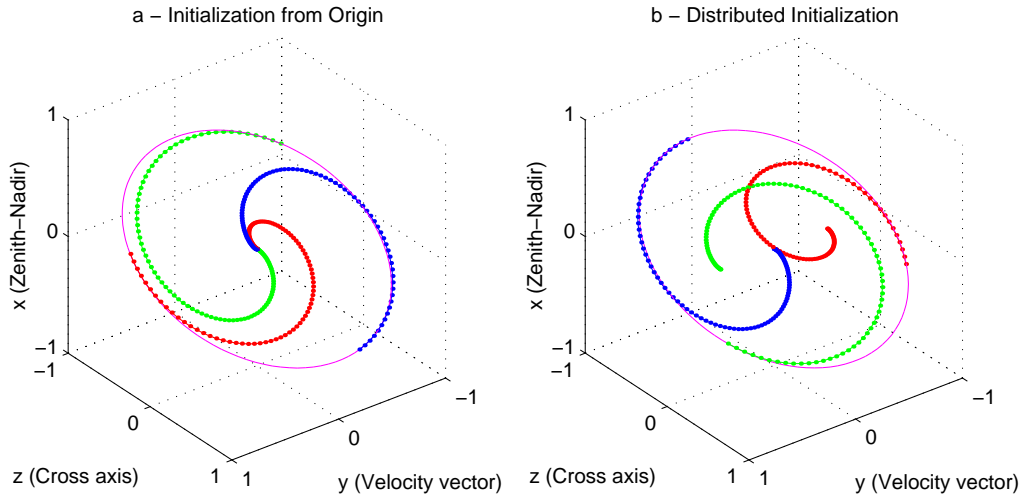
Figure 3.8 Two initialization problems considered in this thesis.

Substituting the energy required to transfer each spacecraft to the various locations on the ellipse from Equation 3.31, the total energy required is then:

$$
\begin{aligned}
E_T &= aN - b \sum_{n=1}^{N} \cos(2\theta + c + 2\alpha_n) \\
&= aN - b \left[\cos(2\theta + c) \sum_{n=1}^{N} \cos 2\alpha_n - \sin(2\theta + c) \sum_{n=1}^{N} \sin 2\alpha_n \right]
\end{aligned}
\tag{3.33}
$$

where α_n is the phase of the n-th spacecraft in the cluster. To determine the minimum energy phasing required for the cluster as a whole, the first derivative of the total energy with respect to the variable θ is obtained and set to zero:

$$
\begin{aligned}
\frac{dE_T}{d\theta} &= -2b \sum_{n=1}^{N} \sin(2\theta_{min} + c + 2\alpha_n) \\
&= 0
\end{aligned}
\tag{3.34}
$$

Expanding the sine term in the equation and through some simple mathematical manipulation, the minimum energy phasing for the entire array can be found to be:

$$\tan 2\theta_{min} = -\frac{\displaystyle\sum_{n=1}^{N} \sin(c + 2\alpha_n)}{\displaystyle\sum_{n=1}^{N} \cos(c + 2\alpha_n)} \qquad (3.35)$$

Of course, to ensure that the variable θ_{min} does in fact correspond to the minimum energy phase, the second derivative of Equation 3.34 must be evaluated such that a positive value is obtained:

$$\left.\frac{d^2 E_t}{d\theta^2}\right|_{\theta_{min}} = -4b \sum_{n=1}^{N} \cos(2\theta_{min} + c + 2\alpha_n) \qquad (3.36)$$

As an example, consider the Cornwell distribution [Cornwell, 1988]. The Cornwell distribution is a set of N points located on a circle such that its u-v points are distributed as uniformly as possible. The objective is to obtain a distribution where redundancies in the baselines between the spacecraft are minimized as much as possible. Using these Cornwell points, the average energy required for each spacecraft in an N spacecraft configuration can be plotted and shown in Figure 3.9. In general, the average energy required per spacecraft remains relatively the same regardless of the number of spacecraft. The energy, however, has a strong dependence on the time for the cluster to complete the maneuver. The time dependencies of these curves can be divided into two portions based upon the gradients of the curves. This division occurs at the initialization time of approximately 0.7 period. The steeper slope in first portion of the curve represents a higher savings in the energy required to initialize the spacecraft if more time is granted. As the curves pass the 0.7 period mark, it seems that there is less incentive to extend the initialization time.

In the special case where the N (> 2) spacecraft are to be equally phased on the elliptical trajectory, the average energy required for each spacecraft can be shown to be the same regardless of the number of spacecraft in the cluster. In this case, the phase for each spacecraft is given by:

$$\alpha_n = \frac{2\pi}{N}(n - 1) \qquad (3.37)$$

which results in the summations in Equation 3.33 to equate to zero:
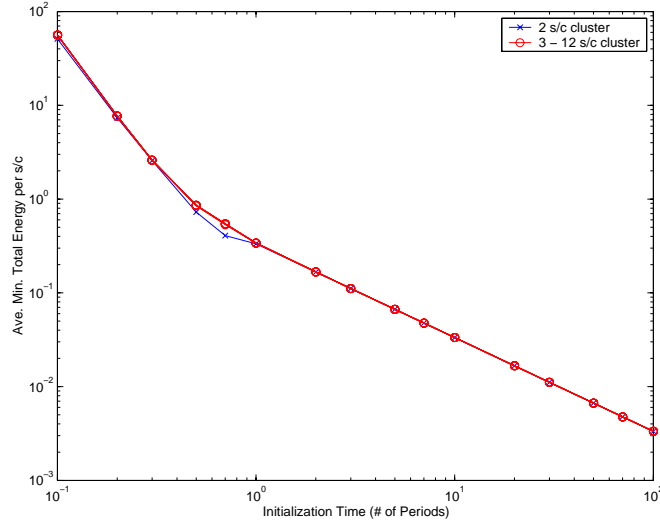
Figure 3.9 Average energy required to transfer a spacecraft from the Hill origin to the free elliptical trajectory using the Cornwell distribution.

$$\sum_{n=1}^{N} \cos 2\alpha_n = 0$$

$$\sum_{n=1}^{N} \sin 2\alpha_n = 0$$

(3.38)

By substituting Equation 3.38 into Equation 3.33, the total energy required to initialize the N spacecraft cluster is therefore:

$$E_T = aN \tag{3.39}$$

which is independent of the phase of the cluster. Clearly, this indicates that as long as the spacecraft are equally phased on the elliptical trajectory, it makes no difference where the entire cluster is initialized to.

One possible distinguishing factor in determining the optimal phasing for the entire cluster is to consider the variation in energy required for all the spacecraft in the cluster. Since it is generally acknowledged that the lifetime of a spacecraft is dependent on the propellant expended, the lifetime of the entire cluster is most likely be determined by the least propellant left in each spacecraft.

As such, the secondary goal of transferring a cluster of spacecraft is to minimize the variation in the energy required:

$$E_{var} = b^2 \sum_{n=1}^{N} [\cos(2\theta + c + 2\alpha_n)]^2 \tag{3.40}$$

which also can be re-written as:

$$
\begin{aligned}
E_{var} &= \frac{b^2}{2}\left[N + \cos(4\theta + 2c)\sum_{n=1}^{N}\cos4\alpha_n - \sin(4\theta + 2c)\sum_{n=1}^{N}\sin4\alpha_n\right] \\
&= \frac{Nb^2}{2}
\end{aligned}
\tag{3.41}
$$

where it can be shown that the summations of the sines and cosines in the equation are again zero if the spacecraft are equally phased in the cluster:

$$
\begin{aligned}
\sum_{n=1}^{N}\cos4\alpha_n &= 0 \\
\sum_{n=1}^{N}\sin4\alpha_n &= 0
\end{aligned}
\tag{3.42}
$$

Again, the derivation indicates that there is no preferential direction where the entire array should be initialized to. The average minimum energy required to initialize an N spacecraft cluster as a function of the initialization time is shown in Figure 3.10. The curves in the plot look very similar to one shown in Figure 3.9. However, the average energy per spacecraft for clusters with more than two are actually the same. In the two spacecraft case, the average minimum energy can also be obtained from Table 3.1 by subtracting the values given by variable b from the variable a.

Minimizing the total energy required to maneuver a spacecraft ensures that the least amount of electrical power is required over time. There is, however, another issue that warrants serious consideration, the instantaneous power required to produce the desirable thrust. Since the size and mass of the power subsystem is dependent upon the electrical power that it needs to generate, it is therefore important to ensure that the optimal trajectories do not require power levels beyond that is available from the power subsystem. The maximum power required to initialize the N spacecraft in the cluster is shown in Figure 3.11. Except for the one and two spacecraft cases, the maxi-
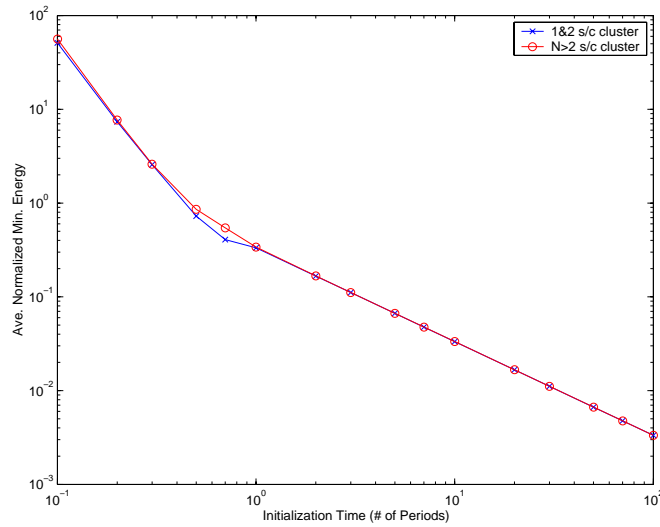
Figure 3.10   Minimum energy required to transfer a spacecraft
from the origin of the frame to the effort free ellipse.
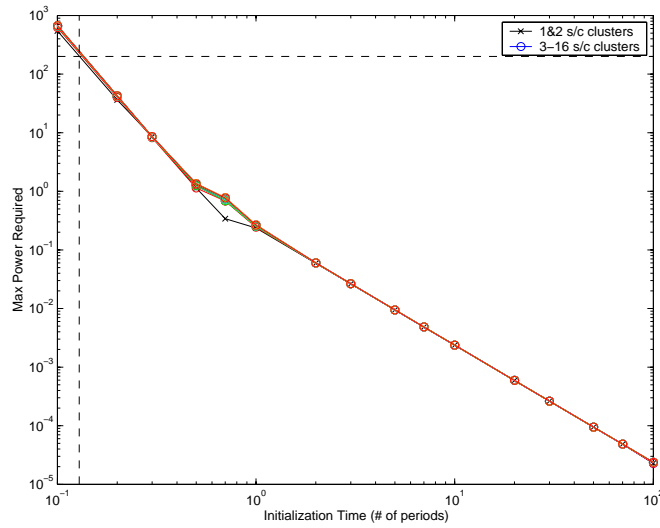
Figure 3.11   Maximum power required for minimum energy trans-
fer from the Hill origin.

mum power required is indeed very similar for the different size clusters.   Similar to the minimum
energy curves, the maximum power curves again exhibit a gradient change at an initialization time
of about 0.7 period. Again, this indicates a greater reduction in the maximum power as more time
is granted to initialize the cluster when short initialization maneuvers are considered.
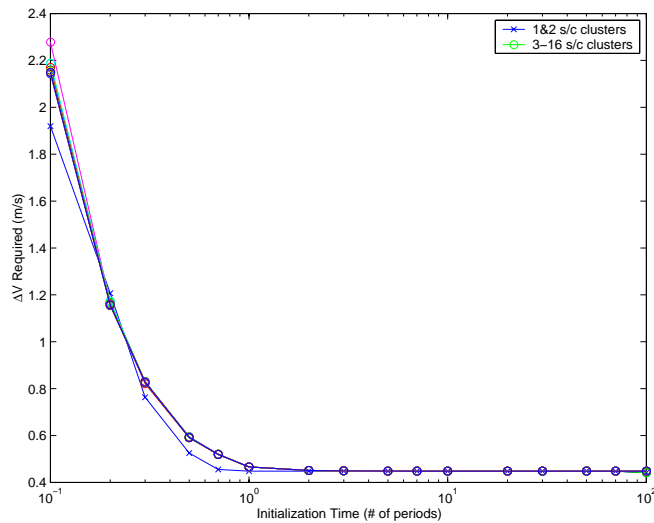
Figure 3.12   Average ΔV required for minimum energy transfer
from the Hill's origin.

The electrical power that is currently designed for the TechSat 21 spacecraft is also shown in the plot at 200 W. In this plot, design points that lie below this 200 W represent the minimum energy trajectories that can be achieved by the TechSat 21 spacecraft. As such, a minimum initialization time of about 0.13 period is required to initialize the TechSat 21 cluster. To initialize a cluster within an orbital period of 0.1, the power available to the propulsion system must be increased to at least 290 W.

The average velocity change (ΔV) associated with these minimum energy trajectories is shown in Figure 3.12. From the plot, it can be seen that the average ΔV required to initialize a cluster of spacecraft tends to rapidly decrease as the initialization time is increased from the minimum of 0.1 period. This decrease, however, asymptotes to value of about 0.45 m/s when an initialization time of at least one period is allowed. Even though the current design does not rule out initialization times of more than 0.13 period, significant savings in velocity change favor initialization times of at least one orbital period. No doubt high specific impulse systems require very little propellant expenditure, any propellant savings will result in longer mission lifetime.

Multi-spacecraft - Initialization From Distributed Locations

In the previous subsection, the energy required to initialize a spacecraft from the Hill origin to the various locations on the elliptical trajectory was found to be sinuisoidal. From the single spacecraft results, the initialization for the multi-spacecraft cluster was found by determining the phasing angle of the entire cluster that results in the minimum energy transfers (θ_{min} in Equation 3.35). The rather simplistic approach works since it was assumed that all the spacecraft are initialized from the Hill origin.

There is, however, no reason to expect all the spacecraft to initialize from the same location. For one, it is not physically possible to have more than one spacecraft at a given location at the same time. As such, in this subsection, it will be assumed that all the spacecraft are distributed evenly along the velocity vector (*y*-axis) of the orbit (Figure 3.8). In doing so, the approach used in the previous subsection will no longer work.

In this problem, the terminal conditions for the spacecraft are specified using the surface conditions for each spacecraft (Equations 3.21, 3.22 and 3.23) and the phasing conditions given in Equations 3.29 and 3.30. In most cases, the optimal trajectories do meet the desired phasing conditions if all the terminal conditions are met. The issue, however is with Equations 3.29 and 3.30. Instead of specifying all the *N* phasing conditions, in order to avoid placing too many constraints on the problem, only *N* - 1 phasing conditions are specified. These *N* - 1 conditions, however, do not uniquely define a particular phasing condition. This may result in trajectories leading to the incorrect phasing conditions. Therefore, to ensure that the desired spacecraft phasing is achieved, the results obtained are checked to ensure the *N*-th condition is also met.

A plot of the maximum power required to initialize a cluster of *N* spacecraft is shown in Figure 3.13. The curves in the figure do in fact look quite similar to ones initialized from Hill origin (Figure 3.11) but with more variability when short initialization times are specified. This variability seems to make sense since for the different cluster sizes, the spacecraft are actually initialized from different locations on the velocity vector. Also, at short initialization times, the maximum power required seemed to be slightly higher except for the two spacecraft cluster case. However, as the initialization times are increased beyond one orbital period, the curves in both Figure 3.11 and Figure 3.13 are almost the same.
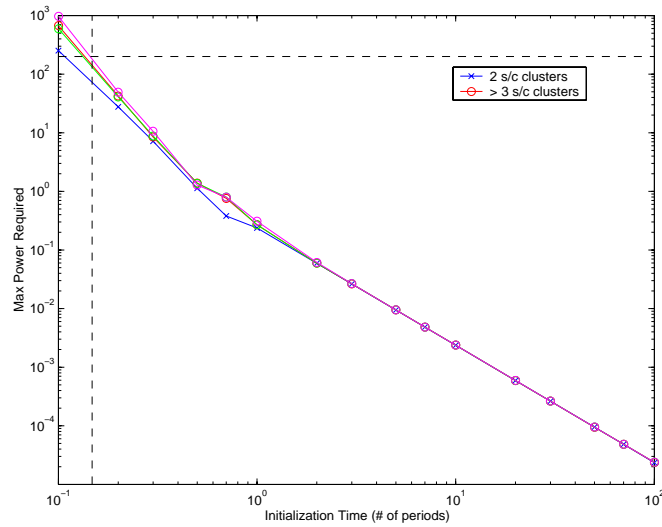
Figure 3.13 Maximum power required for minimum energy trans-
fer for spacecraft distributed along the velocity vector.

The corresponding ΔV per spacecraft required to initialize the spacecraft is shown in Figure 3.14.
Again, it can be seen that the variability in the curves is higher for short initialization times due to
the distributed initial positions. Not only that, it seems that the ΔV required is generally lower too
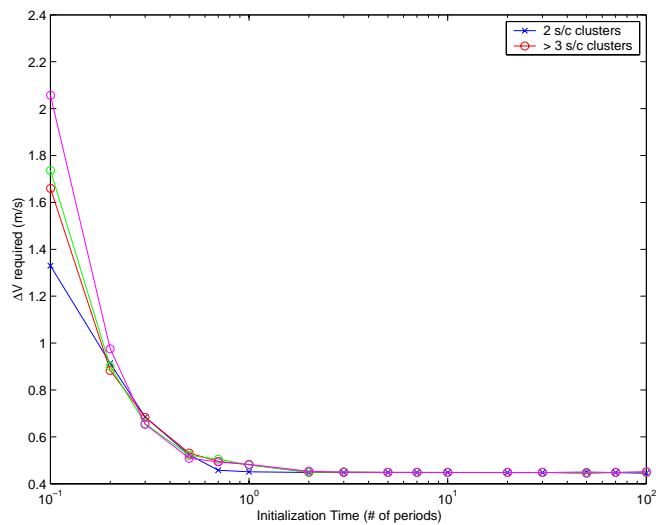
Figure 3.14 Average ΔV required for minimum energy transfer for
spacecraft distributed along the velocity vector.
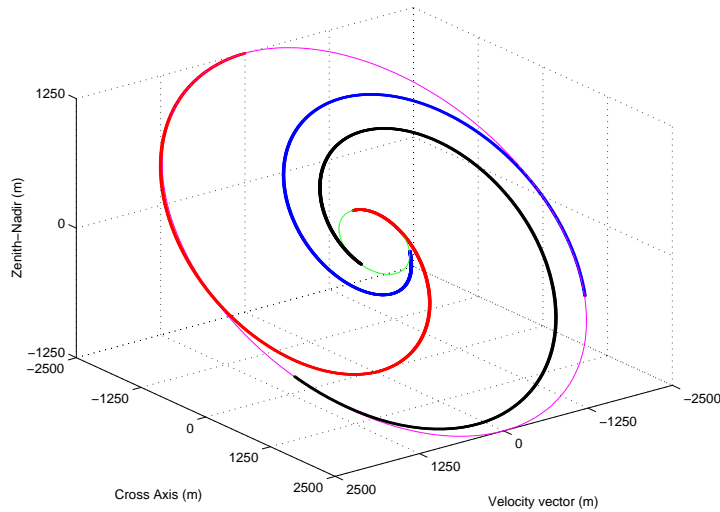
Figure 3.15   Optimal array re-sizing for a three spacecraft cluster.

which can be attributed to the shorter distance that some of the spacecraft in the cluster need to travel to reach the ellipse. However, once the initialization times exceed one orbital period, an average ΔV of 0.45 m/s is required for each spacecraft.

The results seem to indicate that the TechSat 21 cluster can be initialized with a minimum time of 0.2 period. However, at such short initialization times, significant ΔV is required. Velocity change savings up to 3 to 5 fold can be achieved if the initialization time is increased to at least one orbital period. As such, it is recommended that the TechSat 21 cluster be initialized with longer durations since significant velocity change savings can be achieved.

3.4.4 Geolocation

Besides using TechSat 21 as a Space Based Radar system, the AFRL is also interested in using the system to accurately locate objects of interest, that is increasing the angular resolution (better) of the system. One such application is to quickly locate a pilot who has just ejected from his/her aircraft. In a sparse aperture system, the angular resolution is inversely proportional to the baseline of the cluster. Hence, increasing the size of the elliptical trajectory of the cluster will increase the angular resolution of the system. The problem is then to determine the minimum energy trajecto-
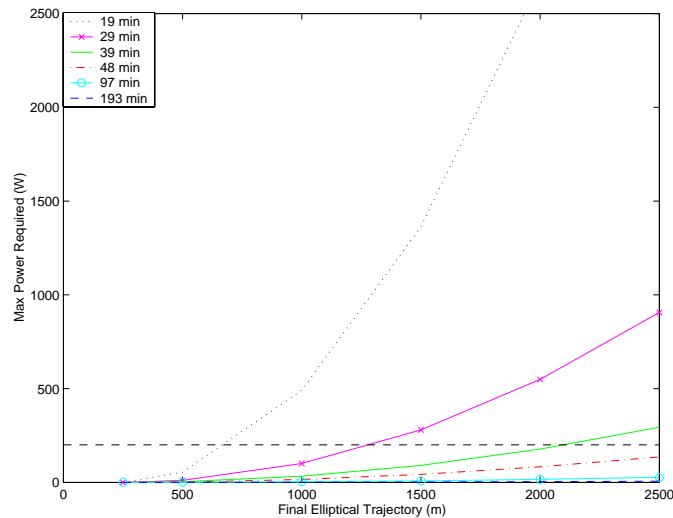
Figure 3.16   Maximum power required to resize a cluster of 3
spacecraft.

ries required to transfer the spacecraft from their original elliptical trajectory to one that is much
larger, as is depicted for a three spacecraft cluster in Figure 3.15.

The maximum power required to resize a cluster of three TechSat 21 spacecraft from the nominal
250 m elliptical trajectory to the different final elliptical trajectories is shown in Figure 3.16. As
expected, the maximum power required to resize the cluster increases as the size of the final ellipse
is increased. The maximum power required is also dependent upon the maneuvering time that is
available. As the resizing time is increased, significant drop in the power requirement is observed.
As an example, the maximum power required decreases more than 93% when the maneuvering
time is doubled from 19 minutes to 39 minutes. However, as the maneuvering time is increased
beyond one orbital period (97 mins), the power required seems to be small. With the maximum
power currently designed for the spacecraft (200 W) marked in the figure, it is clear that the final
ellipse size of 2.5 km cannot be achieved with a maneuvering time of less than 36 minutes.
Besides determining the minimum resizing time that is required for the current TechSat 21 space-
craft, the plot can be used to find the minimum the largest elliptical size that it can achieve if the
resizing time is specified instead. As an example, the largest ellipse that the three spacecraft clus-
ter can reach within 29 minutes is a little over 1250 m.
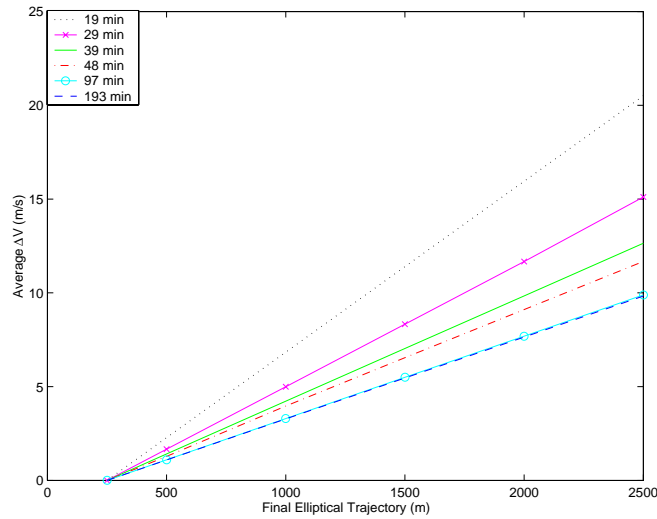
Figure 3.17   Average ΔV required to resize a cluster of 3 space-
craft.

The corresponding average ΔV required to resize the cluster is shown in Figure 3.17. The figure suggests a linear relationship between the ΔV required to resize the cluster and the size of the final ellipse. As expected, the short maneuvering time trajectories require more resources than trajectories with longer maneuvering times. Again, similar to results from the previous subsections, the ΔV required to resize the array seems to remain the same if a resizing time of greater than one period is allowed. To resize the TechSat 21 spacecraft to the desired 2.5 km ellipse, a minimum ΔV of 10 m/s is required, which is quite significant considering that only 40 m/s of ΔV is currently budgeted for the flight experiment spacecraft.

The results obtained indicate that the current TechSat 21 design can in fact be resized to the desired 2.5 km ellipse if a maneuvering time of greater than 36 minutes is provided. The corresponding ΔV that is required for this resizing time is approximately 12 m/s, which is about 30% of the total budgeted for the spacecraft. In cases where time is not a critical issue, it is recommended that the cluster be resized with a maneuvering time of at least one orbital period where 10 m/s of ΔV is required.

3.5 Further Considerations

The results obtained give a good first estimate of the energy and ΔV requirements to initialize and resize a cluster of TechSat 21 spacecraft. There are, however, a number of issues that have yet to be considered in the thesis.

A constraint that is currently not considered in the algorithm is the maximum power that is available to the thrusters at any given time. This constraint has to be checked separately. Even though the trajectories obtained are optimized for electrical energy consumption, power levels that are required to generate a certain thrust level may exceed what is available. Hence, one has to either ensure that the trajectories do not require high power levels at any given instant in time or a constraint must be incorporated into the algorithm.

There exist, however, issues that are related more directly to the TechSat 21 mission. One such issue is the plumes created by the propulsion system. To ensure that the radar performance of the mission is not affected by the generated plumes, it is important to ensure that the thrusters are not fired directly at the other spacecraft in the cluster. Hence, revision of the algorithm should incorporate this plume impingement constraint.

3.6 Summary

In this chapter, the optimal control framework presented in Chapter 2 was applied to the TechSat 21 Space Based Radar cluster. Using a linearized dynamic model, closed form trajectories required to maintain spacecraft formation with minimal effort were presented. Terminal conditions that would allow these spacecraft to theoretically stay indefinitely on these trajectories were developed. The reconfiguration trajectories for these spacecraft were then determined and the capability of the currently designed system was discussed.

Cluster initialization and resizing results, specifically for the TechSat 21 flight experiment cluster of three spacecraft, were presented. In the initialization problem, it was determined that the cluster can be initialized in as little as half an orbital period. However, one may consider increasing the initialization time, as more than 67% of ΔV savings can be achieved. In the minimum energy trajectories, it was also found that the bulk of the effort was spent on changing the spacecraft orbital inclination.

In the geolocation problem, maneuvering times of less than 0.4 orbital period are not possible for the flight experiment spacecraft to resize to an elliptical trajectory of 2.5 km. In cases where the cluster can be resized, significant ΔV is required. It was also found that by increasing the maneuvering time beyond one period, the velocity required to resize the array remains almost the same.

In summary, an algorithm to determine the optimal trajectories to reconfigure a cluster of spacecraft has been developed. Optimal cluster initialization and resizing trajectories for the three spacecraft TechSat 21 flight experiment cluster were determined. For the maneuvers considered in this thesis, a minimum reconfiguration time of half an orbital period is required, with the resizing maneuver costing at least 25% of the budgeted ΔV.

Chapter 4

DISTRIBUTED SPACECRAFT IMAGING

In the previous chapter, reconfiguration trajectories for the TechSat 21 Earth observing multi-spacecraft cluster were determined. Consideration of the sparse aperture radar requirements for the mission resulted in the derivation of the terminal conditions framed in the optimal control framework. Even though a linear dynamic system was found to be adequate, the coupled dynamics made it possible to obtain closed formation trajectories for the spacecraft.

In this chapter, we turn our attention to the imaging of stellar objects using multi-spacecraft interferometers. As discussed in the Literature Review section, the fast dynamics experienced by a spacecraft in Earth's orbit made it technologically challenging to control the spacecraft to within the acceptable tolerances. As such, the idea of placing these interferometers in 'gravitational-free' environments was proposed. In these 'gravitational-free' environments, the dynamics experience by a spacecraft is linear and is affected only by the thrust generated by the spacecraft.

Similar to the TechSat 21 system, an image of the targeted object is obtained by collecting light from the collector spacecraft that are placed far apart to simulate a large virtual aperture. However, the characteristics of the stellar object are usually not known apriori and multiple measurements are required to adequately reproduce an image of the object. Given the limited resources, the selection of a small set of imaging locations that best reproduces the image of the target is therefore important. Hence, the determination of the optimal trajectories for these multi-spacecraft imaging interferometers must take into consideration both the control and science metrics.

In the next section, three different imaging metrics that have been proposed are presented. Based upon the characteristics observed in these proposed metrics, an imaging metric that can be framed into the optimal control framework is proposed. This is followed by the derivation of the necessary and boundary conditions needed to determine the optimal imaging trajectories. Sample trajectories for a two collector interferometer are obtained and the results are discussed. The framework is then extended to consider one of the two NASA's missions that are currently considered for multi-spacecraft imaging: the Terrestrial Planet Finder mission.

4.1 Imaging Metrics

Imaging of astronomical objects using an interferometer requires that the separation between the apertures be known exactly. This separation, normalized by the electromagnetic wavelength of interest, is known as a u-v point. Since it is generally believed that a good u-v coverage (a set of u-v points) will allow one to obtain good interferometric images, previous work in determining the optimal aperture imaging locations has been focused toward maximizing the interferometer's u-v coverage. The relationships between the absolute positions of the apertures and their corresponding components in the u-v domain are given by:

$$
\begin{aligned}
u_{i,j} &= \pm \frac{x_i - x_j}{\lambda} \\[2mm]
v_{i,j} &= \pm \frac{y_i - y_j}{\lambda}
\end{aligned}
\tag{4.1}
$$

where (x_i, y_i) are the coordinates of the i-th aperture and λ is the wavelength of interest [Thompson et al, 1986]. In the optical regime, the u-v coverage is also known as the auto-correlation function of the interferometer [Golay, 1971].

In this section, several proposed imaging configurations are presented. The metrics that are used to arrive at these published results are presented to give the reader an insight as to how these results are determined. The objective is, of course, to determine the appropriate metric that can be used in the optimal control framework to determine the optimal imaging trajectories.

4.1.1 Golay Arrays
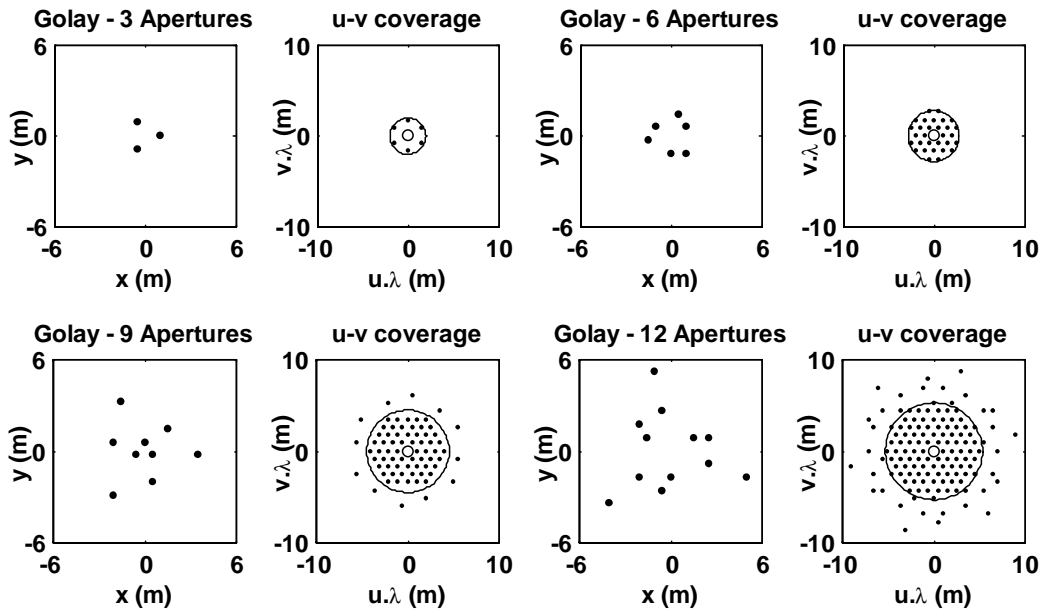
Figure 4.1 Three-fold symmetry Golay Arrays [Golay, 1971].

An optimal imaging configuration designed for small stationary arrays was first proposed by Golay [Golay, 1971]. These arrays are all non-redundant and optimized for compactness in the arrays' auto-correlation function.

The imaging configurations of interest are the threefold symmetry arrays presented in Golay, 1971. These imaging configurations, with their respective auto-correlation functions are shown in Figure 4.1. Golay defined a hexagonal grid in which the apertures can be placed. The apertures are then rotated by 120° and 240° to give the threefold symmetry imaging configuration. For each imaging configuration, the most compact auto-correlation function (u-v points) array is determined. This is done by first assigning a maximum core number, N_c, defined as the number of points within a circle completely filled with auto-correlation points and passing through the unoccupied points of the field closest to the center. The circles in which these points lie are shown in Figure 4.1.

The metric that determines the most compact imaging configuration is given by the core factor number, defined as:

TABLE 4.1   Three-fold symmetry Golay arrays [Golay, 1971].

No. of apertures (N)	Core Number (N_c)	Core factor (C)
3	6	1.00
6	30	1.00
9	60	0.83
12	96	0.73

$$C = \frac{N_c}{N(N-1)} \tag{4.2}$$

where N is the number of apertures in the array. The closer the core factor is to unity, the more compact is the imaging configuration. The core numbers and the core factor numbers for different numbers of imaging locations (N) are presented in Table 4.1.

The advantage of having compact arrays is that apertures of the smallest size can be used to obtain full u-v coverage when the arrays are used in a snap-shot or Fizeau interferometric imaging mode. The Golay-6 imaging configuration has been proposed by the US Air Force Research Laboratory for its UltraLite program [Powers et al, 1997].

4.1.2 Cornwell Points

The Cornwell points were originally developed for instantaneous snap-shot imaging of a target in the radio regime [Cornwell, 1988]. The imaging locations were determined based on the separation of the imaging points in the Fourier plane (u-v points). Imaging configurations with evenly distributed u-v points were preferred and chosen by maximizing the uniformity of the u-v point distribution given by:

$$m(r_1, r_2, \ldots, r_N) = \sum_{i,j,k,l} \log\left(\left|u_{i,j} - u_{k,l}\right|\right) \tag{4.3}$$

where N is the number of points in the physical domain (x-y plane), $u_{i,j}$ is the separation vector between the points i and j in the physical domain and the self-terms in the summation are ignored. Rather than taking the square of the distances in the Fourier plane, the logarithm of the distance is taken so that points that are farther apart are weighted less heavily. Examples of the Cornwell
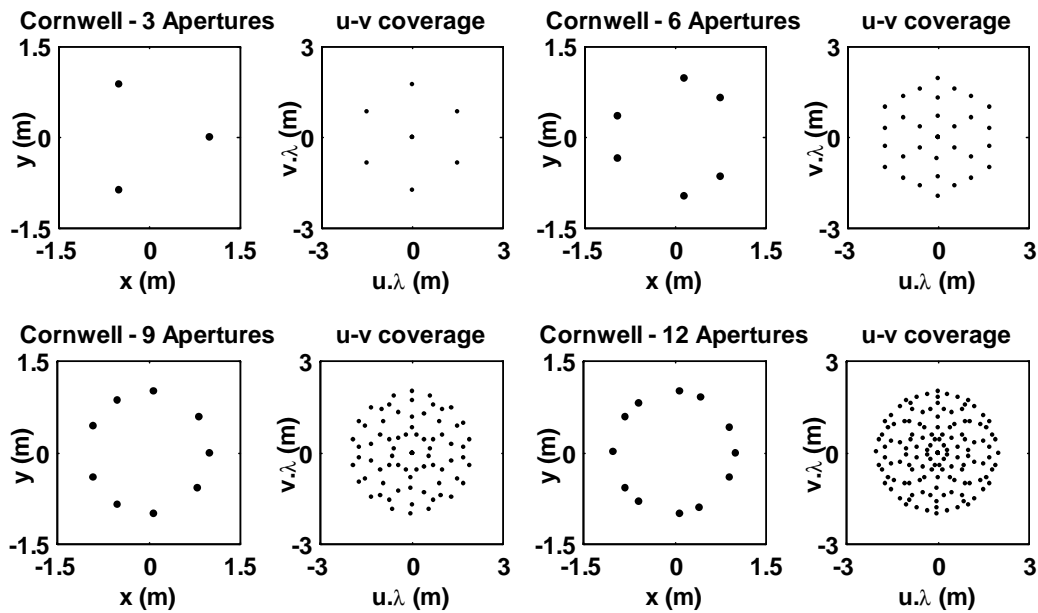
Figure 4.2   Examples of Cornwell imaging configurations [Cornwell, 1988].

imaging configurations are shown in Figure 4.2, while their performance measures are listed in Table 4.1.

Note that the Cornwell points were all constrained to lie on a circle in the physical plane (*x-y* plane) as the imaging elements were found to migrate to the boundary of the optimization space. Hence in his optimization, Cornwell only considered imaging elements that were placed on the circle to reduce the time required to carry out the optimization. Incidentally, the path lengths between all these imaging elements and a combiner element located at the center are the same, which is advantageous for imaging in the visible regime.

TABLE 4.2   Performance measure of the Cornwell Points using Equation 4.3.

Number of Apertures (N)	Performance measure (m)
3	26.8
6	127
9	301
12	544

4.1.3 Encircle Energy

Aperture configurations proposed by both Golay and Cornwell are based solely on their corresponding u-v distributions. These coverages, however, give little indication as to what the actual responses of the interferometer are. Instead, these configurations were determined based upon the idea of having the u-v plane sampling made as much as possible.

Hence, a more appropriate metric to choose should be based upon the response of the imaging system. Typically, one would compare the point response of one imaging system to another. As such, Kong proposed a Mean Square Error metric that compares the response of an imaging system within a given imaging area to one that is considered to be the ideal response [Kong, 1998b]. Such a metric works well when only a small imaging area is of interest and the response of the imaging system is to mimic the desired response.

In the case where one was to consider the entire imaging plane, the appropriate metric is to compare the energy received within the first null of the response to the total energy received by the imaging system. This metric, more commonly known as the Encircle Energy (*EE*) metric, is mathematically expressed by:

$$
EE = \frac{E_{1st}}{E_{Tot}} = \frac{\displaystyle\int_0^{2\pi}\int_0^{r_{1st_{null}}} I \cdot r\,dr\,d\theta}{\displaystyle\int_0^{2\pi}\int_0^{\pi} I \cdot r\,dr\,d\theta}
\tag{4.4}
$$

where *I* is the response of the of imaging system to a point source (Point Spread Function), while *r* and θ are the polar coordinates of the image plane. As an example, the *EE* of a single monolithic circular aperture of diameter *D* is found to be 83.9%. This is obtained by integrating the PSF of the circular aperture, which is given by:

$$
I_{circ}(r, \theta) = \left[\left(\frac{\pi(1 + \cos r)D}{\lambda} \right) \left(\frac{J_1\left(\frac{\pi D \sin r}{\lambda} \right)}{\frac{\pi D \sin r}{\lambda}} \right) \right]^2
\tag{4.5}
$$

The first null of the response is located at:
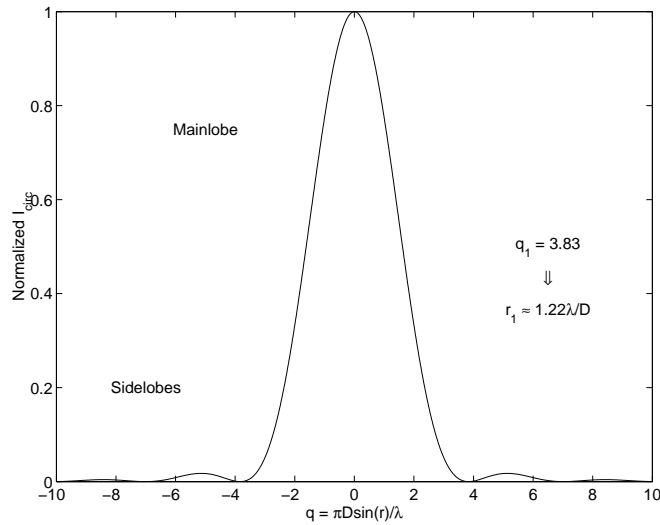
Figure 4.3   Point Spread Function of a circular aperture.

$$r_{1^{st}null} \approx 1.22 \frac{\lambda}{D} \tag{4.6}$$

as shown in the 2-D plot of the PSF (Figure 4.3). Clearly indicated in the figure is the existence of the mainlobe and a number of sidelobes. Since energy from these sidelobes may not be distinguished from the mainlobes of other point sources, the goal is, of course, to obtain an imaging system that minimizes the levels of these sidelobes. Even though not explicitly shown here, the total energy received by the imaging system is only dependent upon the total aperture area. As such, minimizing the energy received in the sidelobes will result in maximizing the energy in the mainlobe. This in turn, leads to obtaining an imaging system that maximizes the Encircle Energy metric.

The *EE* metric can also be used to evaluate a sparse aperture system. In the case where one consider an array of circular apertures of the same diameter *D*, the array's PSF can be written as:

$$I(r, \theta) = I_{circ} \cdot AF \tag{4.7}$$

where *AF* is the array factor of the imaging system obtained based on the aperture imaging locations. The array factor of an *N* aperture system re-oriented *M* times is given by:

$$AF = \sum_{m=1}^{M} \left[\left| \sum_{n=1}^{N} \exp\left(-\frac{2\pi r i}{\lambda} (x_{m,n} \cos\theta + y_{m,n} \sin\theta) \right) \right| \right]^2 \qquad (4.8)$$

where $(x_{m,n}, y_{m,n})$ is the location of the n-th aperture at m-th configuration. Integrating this PSF as required in the *EE* equation, the energy received by the array within an angular separation of r_1 can be shown to be:

$$E(r_1) = 2\pi \int_0^{r_1} I_{circ} \cdot \left[\sum_{m=1}^{M} \sum_{n=1}^{N} \sum_{p=1}^{N} J_o\left(\frac{2\pi r}{\lambda} C_{m,n,p} \right) \right] r\, dr \qquad (4.9)$$

where

$$C_{m,n,p} = \sqrt{(x_{m,n} - x_{m,p})^2 + (y_{m,n} - y_{m,p})^2} \qquad (4.10)$$

is simply the distances between aperture locations. Together with the fact that the total energy collected by the array is dependent on the total collecting area and not on the location of the apertures, determining an array that maximizes the *EE* metric translates to maximizing the total energy received within the first null of the arrays' PSF.

Since the achievable angular resolution of the imaging system is generally considered an important parameter, it makes sense to set the angular resolution of the imaging array and determine the configuration that gives the most energy within the desired angular extent. There is, however, a flaw to this problem formulation. In order to maximize the energy within the fixed angular extent, configurations that gives the shortest aperture separation will result. These configurations, however, will result in the first null being located at some angular some angular extent larger than the desired angular resolution. Consider the PSFs for a two 5m diameter aperture array separated at both 10m and 20m. In Figure 4.4, r_1 represents the desired angular resolution for the array. In the case where the apertures separated by 20m (solid curve), the calculated *EE* is 11.7% while its first null is located at the desired angular extent (r_1). When the separation between the apertures is decreased to 10m (dashed curve), the *EE* is found to be 13.1%, which is higher than the previous 20m separation array. However, the first null of this second separation occurs at a larger angular extent, marked as r_2 in the figure. As such, if one were to only consider maximizing the *EE* of the
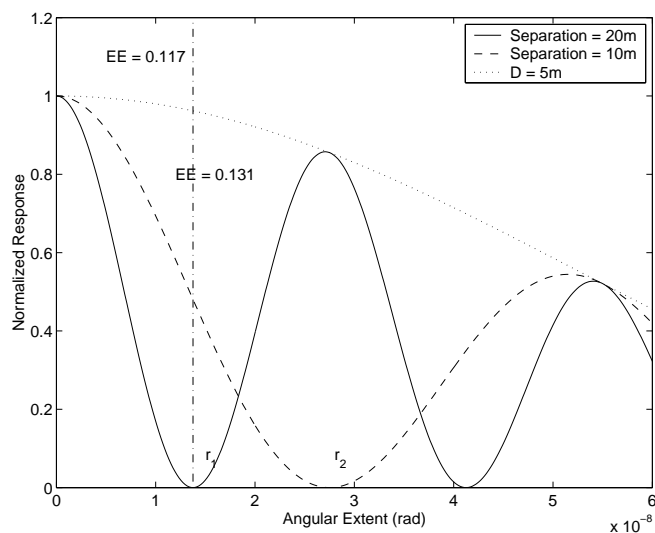
Figure 4.4   Discrepancy in EE evaluation.

array, the results obtained will lead to arrays will the smallest separation while causing the undesirable effect of worsening their angular resolution.

Of course, one can always consider alternative metrics that favor high *EE* values while penalizing a large first null angular extent. Such combined metrics, however, will inherently lead to a rather complicated mathematical expression. Since the calculus of variation approach is taken in this thesis, at some point, the first variation of the imaging metric will have to be computed. Therefore, a simpler imaging metric, one that is similar to the Cornwell metric is proposed. The development of this metric is presented in the next section, followed by its incorporation into the overall optimal control framework.

4.2 Development of Imaging Metric

In this section, the development of the imaging metric used to determine the optimal trajectories for a separated spacecraft interferometer is presented. This is followed by incorporating this imaging metric into the overall optimal control framework. The section concludes with a two spacecraft interferometer example.

4.2.1 Imaging Metric

The goal of this section is to obtain an imaging metric that allows for the best image quality. From the previous section, one observed that the angular resolution of the system is obtained through the largest separation between the apertures, while high *EE* is obtained through short baseline separations. It is, however, generally acknowledged that good u-v coverages will consist of little redundant u-v coverages while favoring medium to longer baseline coverages, as observed in the Cornwell imaging configuration.

One method of evaluating the u-v coverage is to take the auto-correlation of a discretized aperture map of the interferometer. In the case of an interferometer that consists of only circular apertures, one can directly produce a discretized u-v map of the interferometer provided that both the aperture locations and the aperture sizes are known [Kong, 1998b]. With this evaluation, the overlapping u-v coverages will show up as high u-v weighting on the discretized u-v map. A couple of issues arise from such evaluation. First, the determination of the discretization size that should be set on the u-v map. Obviously, the finer the discretization, the better is the u-v coverage estimation. However, finer discretization leads to more elements that need to be considered, which will result in high computational burden. The second issue is the discretization errors that are introduced. Of course, this second issue can easily be solved with finer discretization, that in turn leads to high computational burden.

An imaging metric that is relatively simple but still captures the essentials of the imaging requirements is proposed. The proposed metric is similar to the Cornwell metric. Like the Cornwell metric, the u-v distribution of the aperture locations is first determined (Equation 4.1). This is followed by evaluation of the distances between the u-v points:

$$C_{i,j,k,l} = \sqrt{\left(u_{i,j} - u_{k,l}\right)^2 + \left(v_{i,j} - v_{k,l}\right)^2} \tag{4.11}$$

The goal here is to obtain a fairly distributed u-v distribution since redundant distribution do not give any new information. As opposed to the Cornwell metric, the inverse of Equation 4.11 is obtained such that the best image is obtained by minimizing the proposed metric. The various u-v distances are then summed together to form an overall imaging metric given by:
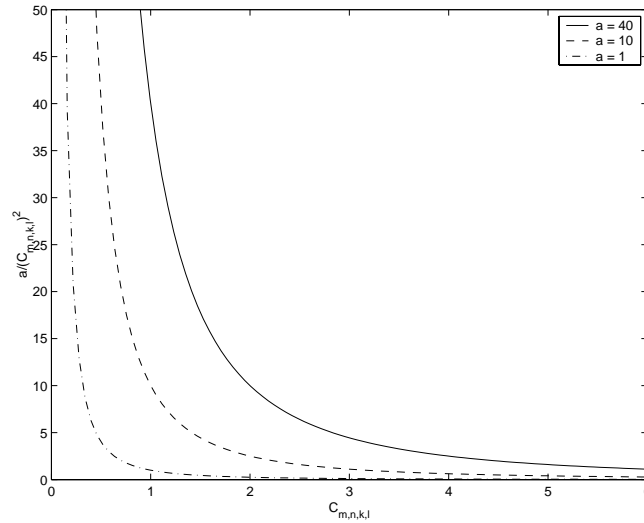
Figure 4.5 Imaging metric penalty as a function of u-v distances.

$$h \;=\; \sum \frac{1}{C_{i,j,k,l}^{2}} \tag{4.12}$$

This metric can also be multiplied with a constant *a* to allow the metric to be weighted against the control effort in the optimal control problem. Plots of the penalty function as a function of the inverse square distances of the u-v points for the various *a* constant is given in Figure 4.5. In each of these curves, one can clearly see that the metric heavily penalizes short u-v separations while favoring long u-v separations. In the case when *a* = 1, u-v separations beyond the value of 1.5 are rather insignificant. This imaging metric is therefore ideal when it is preferable to have u-v separations of at least 1 unit apart to ensure minimal u-v coverage overlapping for a system consisting of 1 m diameter apertures. In the case when larger apertures are considered, one can always increase the constant *a* to favor a minimum u-v separation. In the case when *a* is set to 10, the contribution to the imaging metric by u-v separations that are greater than 6 unit gets less significant.

This simple imaging metric will be used to evaluate the optimal imaging trajectories throughout this chapter. Though simple, this imaging metric captures the essential characteristics of a good u-v coverage map; that is it penalizes short and redundant u-v separations, while do not exactly distinguish between long and extremely long u-v separations. In the next sub-section, the incorporation of this imaging metric into the optimal control framework is presented.

4.2.2 Optimal Control Formulation

Determination of the control effort in the LQ framework results in the optimal trajectory being evaluated continuously within a specified time interval. Evaluation of the imaging metric, however, is a discrete process. As such, there are two issues that must be considered: (1) where the apertures are to be located for optimal imaging; and (2) when these interferometric measurements are to be obtained.

In the optimal control formulation, one can always let the measurement time to be a free parameter within a given total imaging time. However, such formulation is more complicated and problems involving free time parameter do not easily converge to a solution. Therefore, the measurements will evaluated at fixed time intervals. Depending upon the number of interferometric measurements, Q, the time interval for an aperture to travel from a given point to another within the imaging sequence will be set the same. Hence, the Q imaging times within a given time interval are therefore:

$$t_{q+1} = t_o + q\left(\frac{t_f - t_o}{Q+1}\right) \tag{4.13}$$

for $q = 1, 2, ..., Q$. Note that in the numerical solution, there will be at least $Q + 2$ $(= M)$ time steps since both the initial and terminal times must be included too. As for the initial and terminal states, they will both assume zero position and velocity conditions. Though not physically possible to locate more than one spacecraft at the origin at the same time, this assumption is appropriate since the actual locations of the apertures cannot be predetermined. In any event, the framework does not fail for any acceptable initial and terminal conditions, but for the purpose of this research, it will be assumed that the imaging trajectories will initiate and terminate at the frame's origin with zero velocities.

To incorporate the imaging metric (Equation 4.12) into the optimal control framework, the terminal cost (h) in Equation 2.2 can be modified to be a function of not only the terminal states, but a function of all the intermediate states of interest:

$$h = f(\mathbf{x}(t_2), \mathbf{x}(t_3), ..., \mathbf{x}(t_{M-1})) \tag{4.14}$$

With this modification to the h cost, the augmented cost in Equation 2.2 is therefore:

$$J_a = a \cdot h(\mathbf{x}(t_2), \mathbf{x}(t_3), \ldots, \mathbf{x}(t_{M-1})) + \int_{t_1}^{t_M} \{ H(\mathbf{x}(t), \mathbf{u}(t), \mathbf{p}(t), t) - \mathbf{p}^T(t)\dot{\mathbf{x}}(t) \} dt \quad (4.15)$$

where both $t_o = t_1$ and $t_f = t_M$ substitutions are already made to conform with the notations used in the numerical description. The variation of this new augmented cost must now be taken with respect to all the states of interest. For this reason, taking the variations of the h cost with respect to only the terminal states is no longer sufficient. Since the variation of h with respect to all the states of interest will generate Q number of intermediate boundary conditions, it is no longer valid to assume that the variation of the integrand is continuous over the entire time interval (t_o to t_f). Instead, the integrand must be divided into the $Q + 1$ time intervals and boundary conditions for each time interval must be satisfied. Instead of the augmented cost variation shown in Equation 2.6, the new augmented cost is:

$$
\begin{aligned}
\delta J_a &= \left[a \cdot \frac{\partial}{\partial \mathbf{x}_2}(h) \right]^T \delta \mathbf{x}_2 + \left[a \cdot \frac{\partial}{\partial \mathbf{x}_3}(h) \right]^T \delta \mathbf{x}_3 + \ldots + \left[a \cdot \frac{\partial}{\partial \mathbf{x}_{M-1}}(h) \right]^T \delta \mathbf{x}_{M-1} \\[2mm]
&\quad + \int_{t_1}^{t_2} \left\{ \left[\frac{\partial H}{\partial \mathbf{x}} \right]^T \delta \mathbf{x} + \left[\frac{\partial H}{\partial \mathbf{u}} \right]^T \delta \mathbf{u} + \left[\frac{\partial H}{\partial \mathbf{p}} - \dot{\mathbf{x}}^* \right]^T \delta \mathbf{p} + [-\dot{\mathbf{p}}^*]^T \delta \mathbf{x} \right\} dt \\[2mm]
&\quad + \int_{t_2}^{t_3} \left\{ \left[\frac{\partial H}{\partial \mathbf{x}} \right]^T \delta \mathbf{x} + \left[\frac{\partial H}{\partial \mathbf{u}} \right]^T \delta \mathbf{u} + \left[\frac{\partial H}{\partial \mathbf{p}} - \dot{\mathbf{x}}^* \right]^T \delta \mathbf{p} + [-\dot{\mathbf{p}}^*]^T \delta \mathbf{x} \right\} dt \\[2mm]
&\quad + \ldots \\[2mm]
&\quad + \int_{t_{M-2}}^{t_{M-1}} \left\{ \left[\frac{\partial H}{\partial \mathbf{x}} \right]^T \delta \mathbf{x} + \left[\frac{\partial H}{\partial \mathbf{u}} \right]^T \delta \mathbf{u} + \left[\frac{\partial H}{\partial \mathbf{p}} - \dot{\mathbf{x}}^* \right]^T \delta \mathbf{p} + [-\dot{\mathbf{p}}^*]^T \delta \mathbf{x} \right\} dt \\[2mm]
&\quad + \int_{t_{M-1}}^{t_M} \left\{ \left[\frac{\partial H}{\partial \mathbf{x}} \right]^T \delta \mathbf{x} + \left[\frac{\partial H}{\partial \mathbf{u}} \right]^T \delta \mathbf{u} + \left[\frac{\partial H}{\partial \mathbf{p}} - \dot{\mathbf{x}}^* \right]^T \delta \mathbf{p} + [-\dot{\mathbf{p}}^*]^T \delta \mathbf{x} \right\} dt \\[2mm]
&= 0
\end{aligned}
\qquad (4.16)
$$

Integrating the $\delta\dot{\mathbf{x}}$ terms using the integration by parts technique, the equivalent of Equation 2.8 given in Section 2.1 is:

$$\delta J_a = \left[a \cdot \frac{\partial}{\partial \mathbf{x}_2}(h) - \mathbf{p}_2^{*-} + \mathbf{p}_2^{*+} \right]^T \delta \mathbf{x}_2 + \left[a \cdot \frac{\partial}{\partial \mathbf{x}_3}(h) - \mathbf{p}_3^{*-} + \mathbf{p}_3^{*+} \right]^T \delta \mathbf{x}_3 + \dots$$

$$+ \left[a \cdot \frac{\partial}{\partial \mathbf{x}_{M-1}}(h) - \mathbf{p}_{M-1}^{*-} + \mathbf{p}_{M-1}^{*+} \right]^T \delta \mathbf{x}_{M-1}$$

$$+ \int_{t_1}^{t_2} \left\{ \left[\frac{\partial H}{\partial \mathbf{x}} + \dot{\mathbf{p}}^* \right]^T \delta \mathbf{x} + \left[\frac{\partial H}{\partial \mathbf{u}} \right]^T \delta \mathbf{u} + \left[\frac{\partial H}{\partial \mathbf{p}} - \dot{\mathbf{x}}^* \right]^T \delta \mathbf{p} \right\} dt$$

$$+ \int_{t_2}^{t_3} \left\{ \left[\frac{\partial H}{\partial \mathbf{x}} + \dot{\mathbf{p}}^* \right]^T \delta \mathbf{x} + \left[\frac{\partial H}{\partial \mathbf{u}} \right]^T \delta \mathbf{u} + \left[\frac{\partial H}{\partial \mathbf{p}} - \dot{\mathbf{x}}^* \right]^T \delta \mathbf{p} \right\} dt \qquad (4.17)$$

$$+ \dots$$

$$+ \int_{t_{M-2}}^{t_{M-1}} \left\{ \left[\frac{\partial H}{\partial \mathbf{x}} + \dot{\mathbf{p}}^* \right]^T \delta \mathbf{x} + \left[\frac{\partial H}{\partial \mathbf{u}} \right]^T \delta \mathbf{u} + \left[\frac{\partial H}{\partial \mathbf{p}} - \dot{\mathbf{x}}^* \right]^T \delta \mathbf{p} \right\} dt$$

$$+ \int_{t_{M-1}}^{t_M} \left\{ \left[\frac{\partial H}{\partial \mathbf{x}} + \dot{\mathbf{p}}^* \right]^T \delta \mathbf{x} + \left[\frac{\partial H}{\partial \mathbf{u}} \right]^T \delta \mathbf{u} + \left[\frac{\partial H}{\partial \mathbf{p}} - \dot{\mathbf{x}}^* \right]^T \delta \mathbf{p} \right\} dt$$

$$= 0$$

where $\mathbf{p}_q^{*-}$ represents the co-state values at t_q integrated using the conditions at time t_{q-1} and $\mathbf{p}_q^{*+}$ represents the co-state values at t_q. Similar to the results obtained in Equation 2.8, the necessary conditions within each small time intervals remain the same. That is, the states and the co-state equations must be satisfied while the optimal controller is obtained from the terms multiplied by the $\delta \mathbf{u}$ variation.

Since the state boundary conditions (t_o, t_f) are assumed to be zero, the $\mathbf{P}$ and $\mathbf{Q}$ matrices in the numerical solution formulation are just simple block diagonal matrices. The added twist to the problem comes from the intermediate conditions. As the variation of the augmented cost must equate to zero on the extremal, the following intermediate co-state conditions must be satisfied:

$$a \cdot \frac{\partial}{\partial \mathbf{x}_q}(h) - \mathbf{p}_q^{*-} + \mathbf{p}_q^{*+} = 0 \qquad (4.18)$$

for $q = 2, 3, \dots, M - 1$. Similarly, a corresponding set of intermediate state condition must exist. Since there is no reason for the states of the system to be anything but continuous, the intermediate state conditions are simply:

$$- \mathbf{x}_q^{*-} + \mathbf{x}_q^{*+} = 0 \tag{4.19}$$

again for all $q = 2, 3, ..., M - 1$. To determine if the problem is solvable, the number of unknowns (differential equations) and conditions that are available to solve for must be the same. For the N spacecraft problem, each with N_s states, the number of unknowns to solve for is $2 \cdot (M - 1) \cdot N \cdot N_s$, which is also the total number of first order state and co-state differential equations. These unknowns can be determined from the $2 \cdot N \cdot N_s$ initial and terminal state conditions, plus with the $2 \cdot (M - 2) \cdot N \cdot N_s$ intermediate state and co-state conditions. Therefore, this problem formulation is not ill defined.

Similar to the numerical methodology outlined in Chapter 2, these state and co-state conditions can be re-written in a vectorial form:

$$\mathbf{F(s)} = \begin{bmatrix} \mathbf{x}(t_2;t_1,\mathbf{s}_1) - \mathbf{s}_2 - a \cdot \mathbf{h}_{\mathbf{s}_2}(\mathbf{s}_2) \\ \mathbf{x}(t_3;t_2,\mathbf{s}_2) - \mathbf{s}_3 - a \cdot \mathbf{h}_{\mathbf{s}_3}(\mathbf{s}_3) \\ \cdots \\ \mathbf{x}(t_{M-1};t_{M-2},\mathbf{s}_{M-1}) - \mathbf{s}_{M-1} - a \cdot \mathbf{h}_{\mathbf{s}_{M-1}}(\mathbf{s}_{M-1}) \\ \mathbf{x}(t_M;t_{M-1},\mathbf{s}_{M-1}) - \mathbf{s}_M \\ \mathbf{r}(\mathbf{s}_1, \mathbf{s}_M) \end{bmatrix} \tag{4.20}$$

where both the states and co-states at each time step are represented in each entry. The last entry in this $\mathbf{F}$ vector represents both the initial and terminal conditions for the spacecraft.

To use the Newton-Raphson method to solve this optimal control problem, the gradients of the $\mathbf{F}$ vector with respect to all the state and co-state variables are determined. Similar to the general $\mathbf{DF}$ matrix outlined in Chapter 2, the $\mathbf{DF}$ matrix for this problem is found to be:

$$\mathbf{DF(s)} = \begin{bmatrix} \mathbf{G}_1 & -(\mathbf{I} + \mathbf{H}_1) & 0 & & & 0 \\ 0 & \mathbf{G}_2 & -(\mathbf{I} + \mathbf{H}_2) & & & \\ & \cdots & \cdots & \cdots & & \\ 0 & & \cdots & \mathbf{G}_{M-2} & -(\mathbf{I} + \mathbf{H}_{M-2}) & 0 \\ 0 & & \cdots & 0 & \mathbf{G}_{M-1} & -(\mathbf{I} + \mathbf{H}_{M-1}) \\ \mathbf{P} & 0 & & & 0 & \mathbf{Q} \end{bmatrix} \tag{4.21}$$

where the various entries in the matrix are given by:

$$\mathbf{G}_m \equiv D_{s_m}\mathbf{x}(t_{m+1};t_m, \mathbf{s}_m)$$
$$\mathbf{H}_m \equiv D_{s_m}\mathbf{h}_{\mathbf{s}_m}(\mathbf{s}_m)$$
$$\mathbf{P} \equiv D_{s_1}\mathbf{r}(\mathbf{s}_1, \mathbf{s}_m) \qquad (4.22)$$
$$\mathbf{Q} \equiv D_{s_M}\mathbf{r}(\mathbf{s}_1, \mathbf{s}_M)$$

If the problem follows a linear dynamic and quadratic cost formulation, the $\mathbf{G}_m$ matrix is simply the matrix exponential of the Hamiltonian dynamics. The existence $\mathbf{H}_m$ matrix is due to the introduction of the imaging metric. Finally, both the $\mathbf{P}$ and $\mathbf{Q}$ matrices are simply due to the initial and terminal conditions that must be met.

In the next subsection, typical results for a two collector interferometer is presented and discussed. The lessons learned from analyzing this simple example are then applied to the Terrestrial Planet Finder mission.

4.2.3 Two Spacecraft Results

The simplest example considered here is the two collector spacecraft interferometer. With the combiner spacecraft fixed at the center of the interferometer, the equidistant path length requirement for a visible interferometer can be easily met by constraining the second collector spacecraft to follow the mirror image trajectory of the first. The optimization is reduced to determining the imaging trajectory for a single collector spacecraft.

Since the optimal control formulation here is geared towards the NASA's TPF mission, the propulsion system used in this simple example is the high specific impulse Pulse Plasma Thruster (PPT). According to Burton et al, 1998, the ablation rate of a LES-8/9 PPT is 36 μg per pulse at a maximum pulse of 2 Hz, so that the propellant mass flow rate, $\dot{m}$, is 72 μg/s. Even though PPTs are highly efficient in terms of propellant consumption, the electrical thruster efficiency is rather low. In fact, thruster efficiency of about 15% is commonly quoted for PPTs.

A typical optimal trajectory for this two spacecraft example is shown in Figure 4.6 with the trajectory of the first spacecraft represented by the solid line while the second spacecraft by the dotted line. From the figure, it can be seen that the trajectory is symmetric about the line connecting the
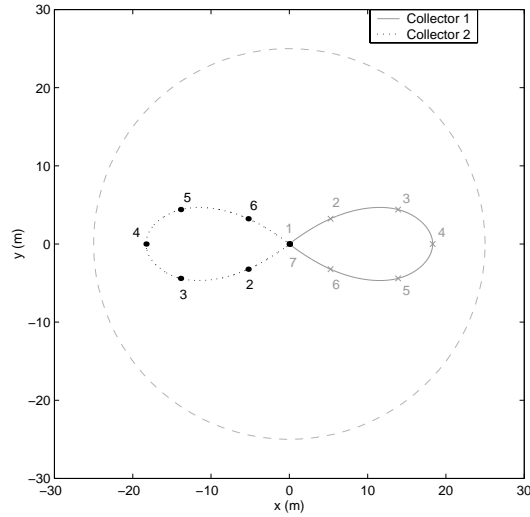
Figure 4.6 Optimal trajectory for two collector spacecraft interfer-
ometer using both the imaging and power metric.

first and the middle imaging locations (1 and 4). With the imaging times being specified at a fixed interval, the imaging locations on this optimal trajectory are also symmetric.

The corresponding state and co-state histories for the optimal trajectory shown in Figure 4.6 are shown in Figure 4.7. Let us consider the lower two subplots that represent the co-state histories first. In the left subplot, three distinct characteristics are observed. The first is the constant values for both the p_1 and p_3 co-states between imaging locations. This actually results from the deriva-tion of the optimal control problem. With the dynamic **A** and **B** matrices simply given by:

$$\mathbf{A} = \begin{bmatrix} 0 & 1 & 0 & 0 \\ 0 & 0 & 0 & 0 \\ 0 & 0 & 0 & 1 \\ 0 & 0 & 0 & 0 \end{bmatrix}, \qquad \mathbf{B} = \begin{bmatrix} 0 & 0 \\ 1 & 0 \\ 0 & 0 \\ 0 & 1 \end{bmatrix} \qquad (4.23)$$

the necessary conditions for both the p_1 and p_3 co-states (Equation 2.23) are found to be:

$$\dot{p_1} = 0$$
$$\dot{p_3} = 0 \qquad (4.24)$$
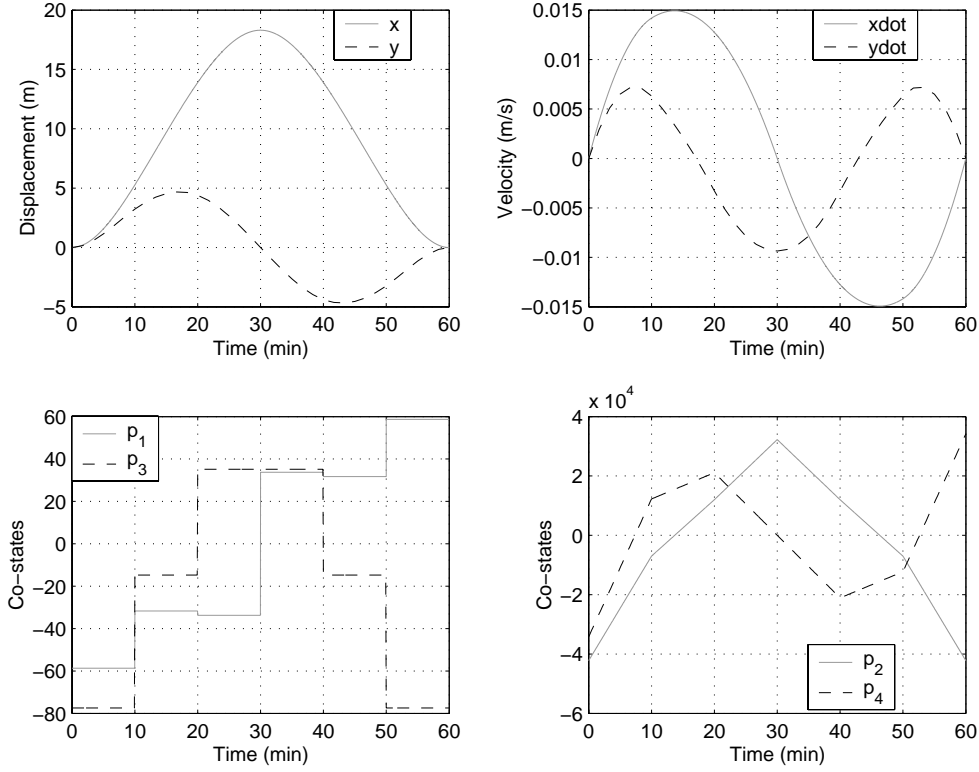
Figure 4.7   Corresponding states and co-states history for optimal trajectory shown in Figure 4.7.

which results in both these co-states to assume constant values between imaging points. The second feature observed are the jumps in co-state values at the imaging locations. This is attributed to the imaging metric that is being introduced into the optimal control problem which results in the intermediate boundary conditions described by Equation 4.18. The values of the jumps at the respective imaging locations do, in fact, correspond to the first derivative of the imaging metric. The third characteristic of the subplot are the asymmetry and symmetry natures of the co-state histories, which again can be related to the boundary conditions described by Equation 4.18:

$$
\begin{aligned}
p_{1q}^{*-} - p_{1q}^{*+} &= a \cdot \frac{\partial h}{\partial x_q} \\[2mm]
p_{3q}^{*-} - p_{3q}^{*+} &= a \cdot \frac{\partial h}{\partial y_q}
\end{aligned}
\tag{4.25}
$$

where the gradients of h in the x direction for symmetric pair of imaging locations are the same while the gradients in the y direction are equal but opposite in directions. Therefore, the time history of the p_1 co-state is asymmetric while the p_3 co-state is symmetric.

The right subplot shows the time history of the other two co-state variables (p_2 and p_4). The trend observed in this subplot indicates the linear nature of the co-states in the time interval between imaging locations. This again is the result from Equation 2.23 where the differential equation for these two co-states are:

$$\dot{p}_2 = -p_1$$
$$\dot{p}_4 = -p_3$$

(4.26)

which result in the gradients of these co-states assuming the values of p_1 and p_3 in these intervals. The asymmetry and symmetry natures of the two curves are again observed since they are related to the first two co-states.

These asymmetry and symmetry characteristics are also observed in the state histories as well. From Equation 2.24, the states of the spacecraft are found to be:

$$\begin{bmatrix} \dot{x} \\ \ddot{x} \\ \dot{y} \\ \ddot{y} \end{bmatrix} = \begin{bmatrix} \dot{x}_1 \\ \dot{x}_2 \\ \dot{x}_3 \\ \dot{x}_4 \end{bmatrix} = \begin{bmatrix} x_2 \\ -p_2/r \\ x_4 \\ -p_4/r \end{bmatrix}$$

(4.27)

which again explains the asymmetry and symmetry natures of the respective curves. Given the nature of these curves, one will expect that the problem can be reduced by half by taking advantage of symmetry. In fact, a full order problem with m imaging locations can be reduced to just (m + 1)/2 imaging locations with the following terminal conditions:

$$\dot{x}^{*}_{m_{mid}} = 0 \qquad p^{*+}_{1m_{mid}} = -\frac{a}{2} \cdot \frac{\partial h}{\partial x_{m_{mid}}}$$
$$y^{*}_{m_{mid}} = 0 \qquad p^{*+}_{4m_{mid}} = 0$$

(4.28)

where a mixed between the first and second terminal conditions in Table 2.1 are used.
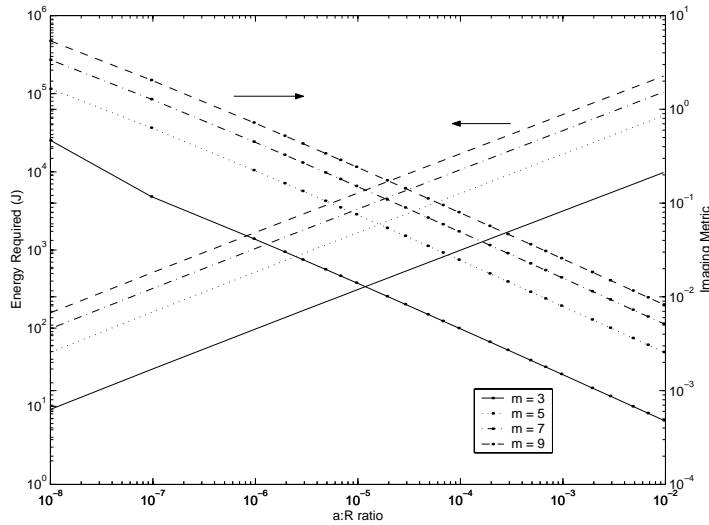
Figure 4.8   Trends in energy required and imaging metric for the
various number of imaging points.

A plot of the energy required and value of the imaging metric (h) as a function of metric weights
ratio (*a:r*) is shown in Figure 4.8. When the imaging weight (*a*) is low compared to the propulsion
weight (*r*), low energy trajectories with high imaging metrics are observed. As *a* is increased,
optimal trajectories requiring more propulsion energy to obtain lower (better) imaging metric
result instead. This trend is consistent even when the number of imaging observations is
increased. Obviously, the required propulsion energy increases with the number of observations.

The corresponding maximum power required to allow the spacecraft to follow the obtained opti-
mal trajectories are shown in Figure 4.9. Similar to the propulsion energy requirement, the
required maximum power increases as the propulsion weight is decreased. Since the total imaging
time is fixed in this problem and the larger *a* to *r* ratios favor trajectories with imaging locations
being spread far apart, a larger propulsive power is therefore needed to complete the trajectory
within the fixed time frame. Higher power requirements for the larger number of imaging loca-
tions are also observed.

The corresponding ΔV required to complete the optimal trajectory is shown in Figure 4.10. The
trend, which is very similar to the power requirement in Figure 4.9 indicates the need for more
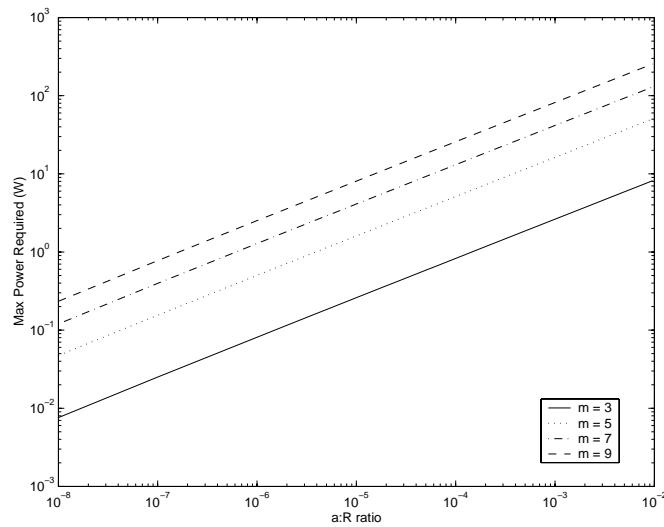
Figure 4.9   Corresponding trend in power requirement for the various number of imaging points.
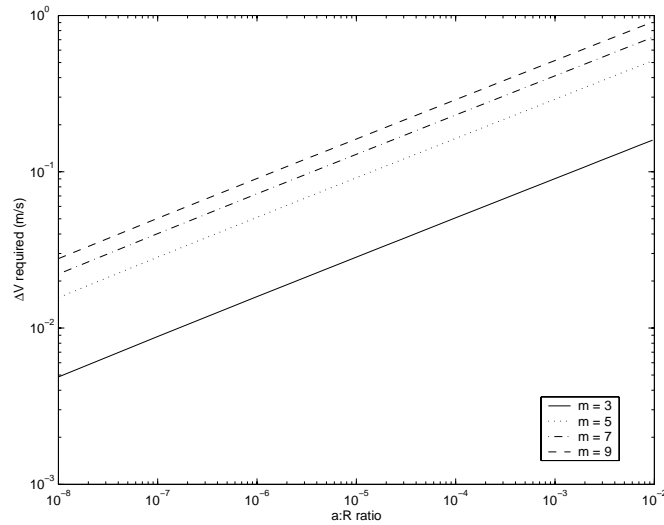
Figure 4.10   Corresponding trend in ΔV requirement for the various number of imaging locations.

resources as the weight of the imaging metric is increased when compared to the propulsion weight and when higher image quality is needed by increasing the number of imaging locations.

In the next section, results specific to one of the two NASA's interferometer missions are presented. The mission considered is the Terrestrial Planet Finder (TPF) mission consisting of four collector and one combiner spacecraft. The primary objective of this mission is to detect the presence of habitable planets in extra-solar systems.

4.3 Application: Terrestrial Planet Finder

4.3.1 Mission Description

In order to achieve NASA's ORIGINS goal of understanding the beginning of life, the Terrestrial Planet Finder Program was established to find Earth-like planets around nearby stars [Beichman et al, 1999]. The key challenge in this mission is to detect the faint planets orbiting about their bigger and brighter stars. Various ways have been proposed to detect these planets but one that has been considered the most is the use of a nulling interferometer.

The concept of a nulling interferometer was first proposed by Ron Bracewell [Bracewell et al, 1979]. The basic principle of this interferometer is in fact very similar to the commonly known Michelson interferometer, except for the 180° phase shift introduced to one of the two light paths to create a destructive interference to null out the bright parent star. Comparison between the radiation from the sun and the reflection of the Earth indicates that star light nulling can be easiest made in the infrared regime as the signal from the star needs to be attenuated only by a million times compared to the billion times in the visible regime. Given that stars within 5 to 15 parsecs away are to be surveyed, it was determined that a four collector spacecraft interferometer distributed evenly along a 75m baseline is required [Beichman et al, 1999]. To detect the existence of planets around the bright stars, the entire interferometer must rotate by 180° about the combiner spacecraft that is located at the center of the array.

A secondary objective was then tagged on to the original TPF mission to increase its attractiveness. This second objective calls for the general astrophysical imaging of stellar objects using the same spacecraft that are designed for the planet detection mission. Instead of blocking out the bright stars through destructive interference, the goal is to constructively create images of the target stars. Star light reflected off the collector spacecraft is to be constructively interfered in the combiner spacecraft, thus making it a Michelson interferometer.

Of course, the requirements for a Michelson interferometer differ from that of a nulling interferometer. In the latter case, the key objective is to null out the parent star and try to detect the presence of a planet by rotating the array about the parent star. In the imaging mode, however, the goal is to reconstruct the image of the targeted object from the sparse interferometric measurements. As described earlier in the chapter, a good image can be achieved by filling out the u-v plane, thus simulating measurements from a large mirror. This, however, can only be performed given infinite resources and time. To obtain images with the limited resources, the combined metric developed in the previous section is used to determine the best imaging trajectories for the TPF spacecraft.

4.3.2 Mission Parameters

Mission parameters that are relevant to the analysis of the TPF interferometer operating in the imaging mode are presented in this section. Since the concept is to ensure that the current design can meet this new imaging requirement, no major hardware changes are expected for the spacecraft and so, the dimensions and mass allocations are not expected to change.

The mass breakdowns for both the collector and combiner spacecraft are tabulated in Table 4.3 [Beichman et al, 1999]. The dry mass of the collector is currently listed at 600 kg. This value includes the mass of everything except for the propulsion and propellant masses. At present, the propulsion system for these spacecraft has yet to be fully determined except that high impulse electric propulsion systems will most likely be the thrusters of choice. Therefore, to demonstrate the viability of the framework proposed in this thesis, the PPT specifications given Section 4.2.3 will be assumed for the TPF spacecraft.

In the report published by the TPF Science Working Group, an illustrative scientific utilization plan for the TPF was presented and is reproduced here in Table 4.4 [Beichman et al, 1999]. Since

TABLE 4.3   TPF spacecraft mass breakdown [Beichman et al, 1999].

Mass Components	Collector S/C		Combiner S/C	
	Mass (kg)	Power (W)	Mass (kg)	Power (W)
Dry	600	268	568	686
Propulsion	96	300	96	300
Propellant	35	N/A	23	N/A

TABLE 4.4   Illustrative Scientific Utilization Plan for TPF [Beichman et al, 1999].

	Year 1	Year 2	Year 3	Year 4	Year 5
In-orbit Checkout	0.2	0	0	0	0
Planet Survey	0.5	0.5	0.2	0.1	0.1
Medium-Depth Spectroscopy	0.1	0.2	0.4	0.4	0.3
Deep Spectroscopy	0.1	0.1	0.1	0.2	0.2
General Astrophysical Imaging	0.1	0.2	0.3	0.3	0.4

the primary objective of the mission is to detect planets in extra-solar systems, the first few years of the five year mission are heavily loaded with planet detection operations. The imaging of general astrophysical sources is also considered in the plan. This secondary objective is given little observation time in the early stages but is increased to about 40% of the observation time in the fifth and final year of operation. Based upon this plan, the percentage of time allocated for general astrophysical imaging operation is 26%. Assuming that the available resources are distributed according to the plan shown in Table 4.4, each collector spacecraft will then be allocated 9.1 kg of propellant for the purpose of general astrophysical imaging.

The concept of using the TPF for the purpose of general astrophysical imaging is still at a very infant stage. For this reason, the requirements for this portion of the mission are not entirely defined. Given uncertainty in the requirements of the mission, the best estimate that the TPF Science Working Group came up with is that it will take about a half to one full day to completely observe a target [Beichman et al, 1999]. Given this, a total about 750 - 1000 images are to be obtained by TPF. Assuming the high end of these numbers and given an average of 26% of the total mission lifetime dedicated to the imaging process, the average time allocated to obtain an image is about 11 hours. For the purpose of this research, this value will be used as the baseline case.

Since the TPF interferometer is designed to operate in the infrared regime, the imaging process requires equal path lengths for star light reflected off the collector spacecraft. The same wavefront from the targeted object must be coherently interfered at the combiner spacecraft. One possibility to achieve this equal path length requirement is to place all four collector spacecraft at equal distances away from the combiner spacecraft. Since the imaging goal is to maximize the u-v point distribution of the interferometer in the imaging plane, placing these four spacecraft using the

Cornwell-4 distribution seems to make sense. With this configuration, up to 12 new u-v points can be obtained each time the spacecraft are reconfigured.

With the equal path length requirement and using the Cornwell-4 distribution, the dynamics of the system can be further simplified. Similar to the two spacecraft case considered in the previous section, the problem is then reduced to only a one spacecraft case with the other three spacecraft distributed in a prescribed configuration. Even though this simplification does not guarantee optimal results in terms of control metrics, non-uniformity concern involving resource usage is a not a factor as all the collector will use the same amount of resources.

4.3.3 Results

Typical trajectories obtained for the TPF spacecraft operating in the imaging mode are shown in Figure 4.11. Since a Cornwell-4 configuration is used to satisfy the equal path length requirement, the trajectory for each spacecraft is in fact the same except that they are rotated by the corresponding Cornwell angles. In fact, the trajectories shown here are very similar to the trajectory obtained for the two spacecraft case shown in Figure 4.6 where a tear-drop shape trajectory is observed. In general, as the weighting ratio between the imaging metric to the control metric is increased, trajectories with imaging locations located further apart are observed. This in turn increases the length of the trajectory, thus the size of the tear-drop shaped trajectory. The corresponding u-v
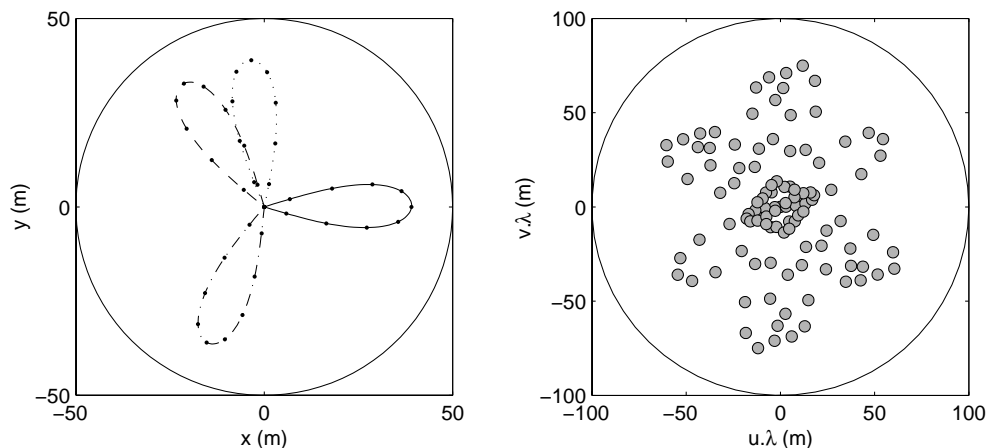
Figure 4.11   Optimal trajectory for the four TPF collector spacecraft in operating in the imaging mode.
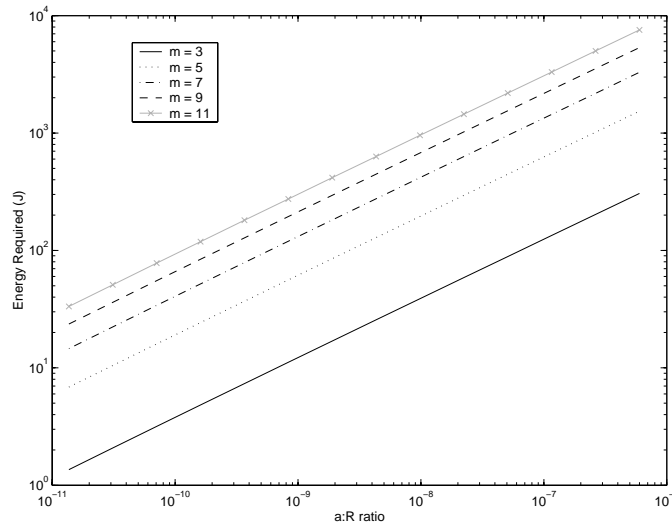
Figure 4.12   Total energy per spacecraft required to complete the
TPF imaging trajectory as a function of imaging to control metric
weighting.

coverage for the interferometer is also shown in the figure. This coverage assumes only 11 imaging measurements.

A plot of the total electrical energy required for the spacecraft to complete the imaging trajectory is shown in Figure 4.12. The results are very similar to the two spacecraft case considered in the previous section. As the imaging metric is weighted more heavily (large a to *r* ratio), more energy is required for the spacecraft to follow the trajectories that give better image quality. Also observed in the figure is the higher propulsion energy required to complete a trajectory with higher number of imaging locations. However, there is a trade-off between obtaining fewer number of observations that are located further apart and obtaining more observations that are located closer together.

Instead of plotting the imaging metric used to determine the optimal trajectories as a function of the weighting ratio of the combined metrics, a plot of the trajectory using the Cornwell metric is shown in Figure 4.13. Using this metric, high Cornwell value corresponds to better image quality. Clearly observed in the plot is the better quality of images that can be obtained when both the number of imaging locations and the weighting ratios are increased. Again, there are trade-offs between taking more measurements that are located closer together and fewer measurements that are located further apart at the expense of more control effort.
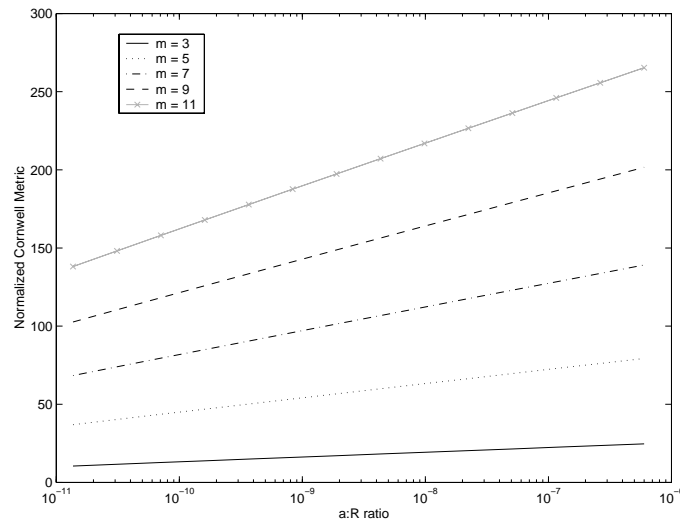
Figure 4.13   Trends of Cornwell metric normalized by the number
of unique u-v points (TPF).
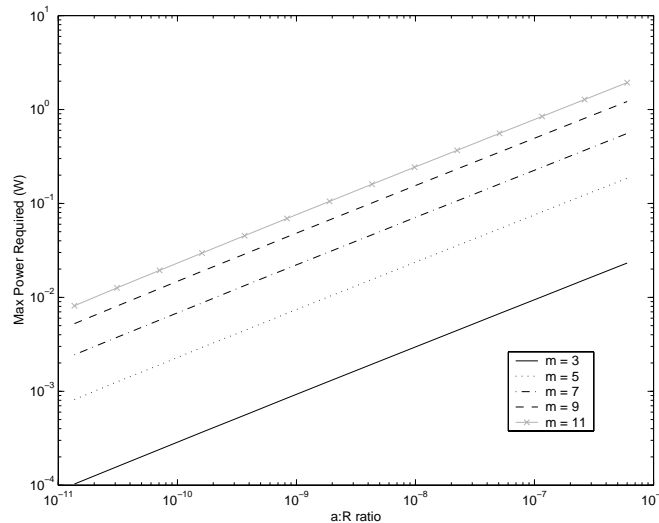
Figure 4.14   Corresponding maximum power required for the TPF
spacecraft to complete the imaging trajectory.

The corresponding maximum power and ΔV plots required for each spacecraft are shown in
Figure 4.14 and Figure 4.15. According to these plots, the resources required are in fact minimal:
maximum power of only 1.93 W and ΔV of only 0.14 m/s. Considering the 1000 images that are
scheduled for the TPF interferometer, the amount of propellant required for the imaging process is
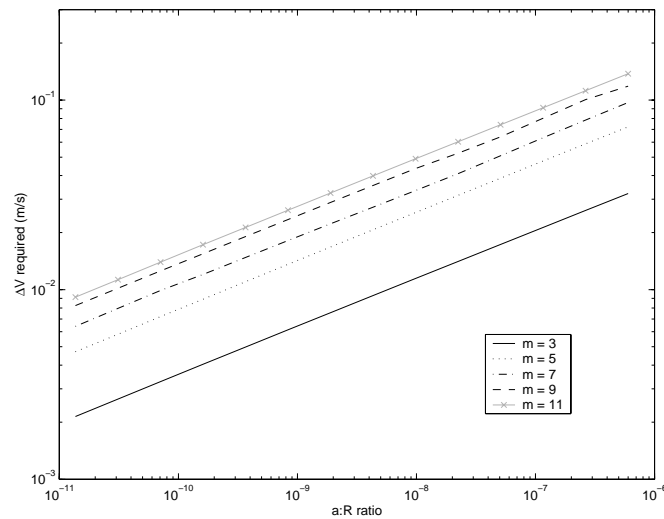
Figure 4.15   Corresponding ΔV per spacecraft required to complete
the TPF imaging trajectory.

only 8.6 kg, which is within the allocated 9.1 kg. In fact, the extra 0.5 kg of propellant can be used to obtain 55 more images. Therefore, the currently designed TPF multi-spacecraft interferometer can in fact meet the new imaging requirements levied upon it.

Since the required amount of propellant is less than the allocated amount, there also exists the possibility of increasing the imaging rate of the TPF interferometer. Shown in Figure 4.16 are the maximum power required and the corresponding Cornwell imaging metric for images as functions of the imaging time. Clearly indicated in the figure are the higher power requirements and worse image quality when little time is available for the interferometer to obtain an image. The preference is obviously to allow as much time as possible for the interferometer to obtain an image. In the remote event that a target must be imaged within a short time frame, the minimum time that the TPF can do so is 1.5 hrs, based upon the 300 W budgeted power for the propulsion system. The corresponding ΔV per spacecraft required as a function of imaging time is shown in Figure 4.17. As the imaging time is increased, the ΔV requirement becomes less stringent. Given the number of images and propellant requirements, a minimum imaging time of 8.5 hrs must be allocated for each image. At this imaging time, a relatively good quality of image can be obtained with relatively low power.
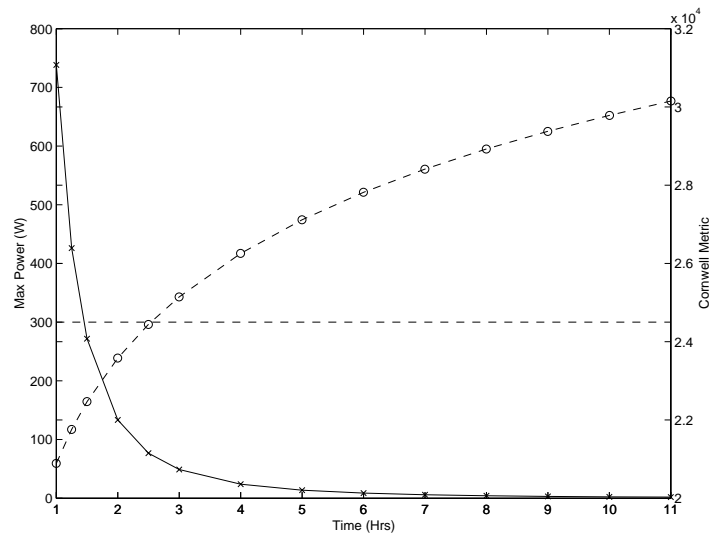
Figure 4.16 Maximum power required and corresponding Cornwell metric as a function of imaging time (TPF).
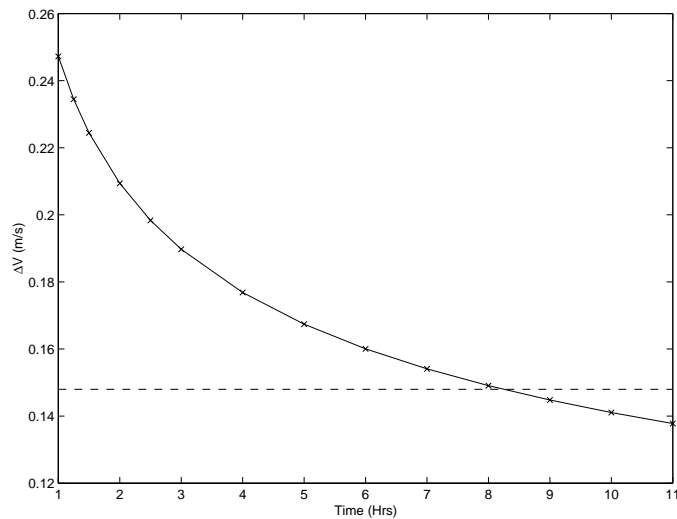
Figure 4.17 ΔV required as a function of imaging time (TPF).

The results obtained here indicates that the currently designed TPF interferometer can meet the newly imposed imaging requirement using the resources allocated to it. In fact, based upon the propellant allocation, an additional 50 images can be obtained if there is a need to do so. Alterna-

tively, the average imaging time for each target can be reduced by 22% with the allocated 9.1 kg of propellant.

4.4 Further Considerations

The distributed spacecraft imaging study performed in this thesis allowed us to determine the viability of the currently designed TPF interferometer to meet the new imaging requirement. However, much work must still be considered to realize such an enormous mission. In this section, some immediate considerations that resulted from this study is presented.

One major concern associated with a propulsion based multi-spacecraft interferometer is plume impingement as a result of thruster firings. Plume impingement can be bad in a number of ways. First, the dynamic stability of neighboring spacecraft can be affected by direct impingement. Second, the possibility of particulates depositing on sensitive optics can significantly affect the performance of the interferometer. Third, the high speed particle ejection can in fact ablate material off the spacecraft thereby causing permanent damage. Fourth, for imaging in the infrared regime, the propellant plume can put a thermally bright haze across the line-of-sight of the telescope. One proposed solution is to ensure that the interferometer is always moving in the direction of the target such that thruster firings are never directed towards the line-of-sight of the system. Another possibility is to formulate a problem that considers plume avoidance maneuvers. The trajectories obtained should result in minimal thruster firings when either the spacecraft are closed together or the thrusters are aimed at the other spacecraft. These trajectories will require more resources than those without such constraints. Preliminary work in this area has been reported in [Richards et al, 2001].

In this study, the imaging metric is based upon the general consensus that an image that results from a well distributed u-v coverage should provide good image quality. However, the quality obtained is really dependent upon the type of stellar targets that is being imaged. In order to maximize the science returns, the types of targets that are to be imaged must first be identified. Then, the science requirements that correspond to these targets must be obtained, e.g. more distributed u-v points or less u-v measurements with longer integration times. These requirements can then be formulated into the optimal control framework such that the appropriate trajectories can be deter-

mined. Increasing the fidelity of the analysis will no doubt give a better estimate as to the resources required to fulfill the mission.

4.5 Summary

In this chapter, the optimal control framework described in Chapter 2 was applied to a multi-spacecraft interferometer. Based upon both the imaging and control metrics, the optimal imaging trajectories for a two spacecraft interferometer operating in a 'gravitation-free' environment were determined. The analysis was further extended to consider the viability of the currently designed TPF interferometer to meet the newly imposed imaging requirements.

In order to understand the general imaging requirements, an overview of three proposed imaging metrics are presented in Section 4.1. In general, since the characteristics of the target are not usually known, images that result from a well distributed u-v coverage are usually considered good. Even though redundant u-v coverage can improve the signal-to-noise ratio of the measurements, information obtained from additional u-v points can contribute to better image quality. Of course, a balance must be struck between spending more time to reduce the noise in a single measurement and obtaining more measurements for the given observation.

Assuming that the integration time for a given measurement is much shorter than the reconfiguration time of the spacecraft, an imaging metric that captures the general requirements of the already proposed metrics is developed. This imaging metric penalizes heavily both redundant and extremely short baseline coverages and encourages long baseline coverages to a certain degree. This metric is then introduced into the optimal control framework and the necessary and boundary conditions to determine the optimal trajectories are then obtained. As opposed to the TechSat 21 mission considered in Chapter 3, intermediate boundary conditions are found to exist at the pre-defined imaging times. More specifically, the introduction of the imaging metric caused the co-state trajectories to be non-continuous functions across the intermediate boundaries. However, the state trajectories still remain continuous as shown in the two spacecraft example.

The framework is then applied to NASA's TPF mission. Originally designed to detect the existence of Earth-like planet around extra-solar systems, a general astrophysical imaging requirement has been levied onto the mission to make it more attractive. The optimal trajectories based upon a

four collector spacecraft arranged in a Cornwell imaging configuration are determined. The results indicate the current design can meet the imaging requirements of the proposed scientific plan. Assuming that 26% of the resources are allocated to the astrophysical imaging process, up to 1050 images can be obtained with the current system.

To summarize, the optimal trajectories for distributed spacecraft imaging systems are determined based upon both the imaging and control metrics. Formulating the problem in the optimal control framework results in discrete jumps in the co-state trajectories at the predefined imaging times. Application to the NASA's TPF indicate that the currently proposed system can meet the new imaging requirements as proposed in the scientific plan.

Chapter 5

EM FORMATION FLIGHT

In the previous chapters, the main emphasis is to determine the optimal trajectories for the multi-spacecraft cluster such that minimal effort, including electrical power and propellant, is required. The expenditure of these precious propellants has several implications. First, propellant is a consumable that, once depleted, renders the satellite useless. Second, the impingement of a thruster plume on a neighboring spacecraft can cause a dynamic disturbance to its stability, deposit particulates on sensitive optics, induce inadvertent charging, and actually ablate material off the spacecraft thereby causing permanent damage. Third, for missions such as NASA's Terrestrial Planet Finder (TPF), the propellant plume can put a thermally bright haze across the line-of-sight of the telescope. For example, micron particles at room temperature can blind TPF even if the particles are many kilometers away [Beichman et al, 1999]. Furthermore, low speed plume exhaust will tend to be attracted to the spacecraft, creating a local pollution haze through which the telescope must look.

As one explores the design of these systems in more depth, one recognizes that there is a mismatch between the geometric requirements that the formation must achieve and the way in which that geometry is controlled. Specifically, the relative separations between spacecraft, not the absolute inertial position in space, is important. However, thrusters actuate inertial degrees-of-freedom. Therefore, it would be desirable if a form of formation control can be developed which does not rely on precious consumables and that reduces the amount of contamination introduced by thrusters.

In this chapter, a formation flight concept based upon the use of electromagnetic forces between spacecraft to control formation geometry is explored. This Electromagnetic Formation Flight (EMFF) concept controls relative positions and orientations between spacecraft through the use of a renewable energy source: electrical power. In the next section, the basic concept of the EMFF concept is presented. A mission efficiency metric is presented such that the different EMFF designs can be adequately compared. The design exercise is then extended to NASA's TPF mission and compared to the different proposed propulsion systems. Controllability issues for this EMFF concept are also investigated. Finally, the chapter concludes with a discussion of the EMFF interferometer spinning-up work done by researchers at the MIT Space Systems Laboratory.

5.1 EM Formation Flight Concept

5.1.1 General Concept

The EMFF concept is best applied to a rotating separated spacecraft interferometer such as the TPF mission. Previous concepts have considered using tethers, structures and also propulsion to balance the centripetal load experienced by the rotating array. For missions that require large spacecraft separation like the TPF interferometer, it was found that formation flying seems to be the most effective solution [Stephenson, 1998].

The centripetal load experienced by a spacecraft rotating about a point at an angular rate of ω is given by:

$$F_c = \frac{1}{2}m_{sc}B\omega^2 \tag{5.1}$$

where m_{sc} is the mass of the spacecraft and $B/2$ is the distance of the spacecraft from its center of rotation. In this EMFF concept, this centripetal load is balanced by the EM force. The EM force is generated by using a set of EM coils and/or cores, as shown in Figure 5.1. Each spacecraft contains an electromagnetic coil of diameter $2a$ and the spacecraft are separated by a baseline B. The longitudinal axes of the two coils are co-linear. The generated force is a function of permeability (μ_o), coil geometry, and vehicle separation (B):
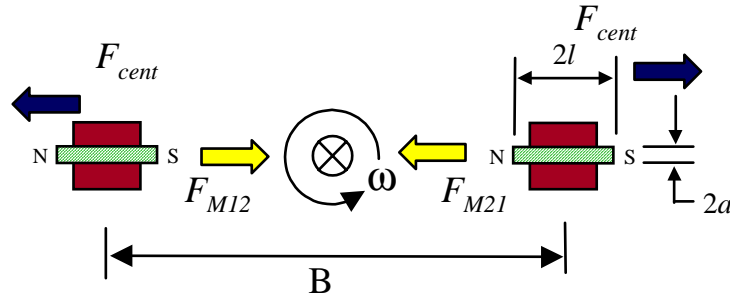
Figure 5.1   Two spacecraft EMFF concept.

$$F_{M_{12}} = \frac{3}{2}\mu_o\pi\frac{n_1 n_2 i_1 i_2 (\chi + 1)^2 a^4}{B^4} \tag{5.2}$$

where n_1 and n_2 are the number of turns of the conducting coils, i_1 and i_2 are the respective currents in the coils, and χ is the relative susceptibility of the core. In the absence of a magnetizable core, χ takes the value of zero.

As a rough first order analysis, consider a system of two 600 kg spacecraft separated by a baseline of 75 m and rotating at one rotation per eight hours (TPF parameters). Further assuming that each spacecraft is equiped with a 2000 turn coil with 10 amps of current running through the coils. The size of the coil that is required to provide the necessary magnetic force to compensate for the centripetal load is about 2 m in radius. If a ferromagnetic core is added ($\chi = 100$), the size of the core/coil combination can be reduced down to 0.2 m. This addition corresponds to significant mass savings considering a coil mass of about 380 kg is required for the coil only option and a coil/core mass of only 140 kg is required for the latter.

5.1.2 Pole representation

The EM attraction force given by Equation 5.2 is only valid for a pair of dipole electromagnets placed in the orientation shown in Figure 5.1. In order to analyze more general cases, one can consider the use of multipole electromagnets. These multipole magnets can be best analyzed by considering the EM forces generated from the interaction between the poles on one magnet to the poles on the other (Figure 5.2). In this section, a short development of a two dipole system is pre-
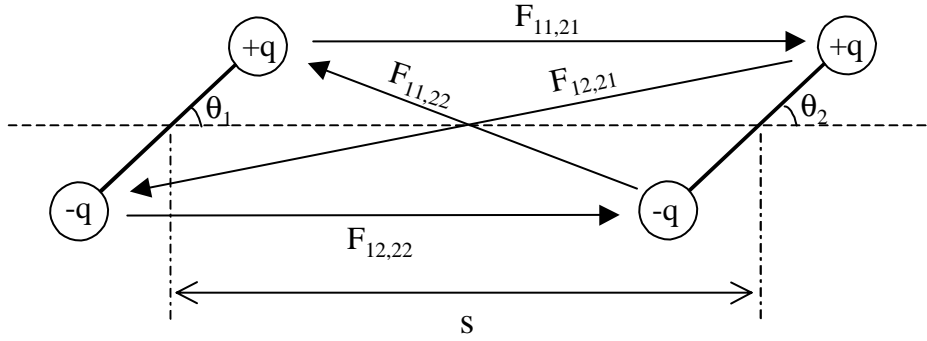
Figure 5.2 Dipole representation.

sented with the magnetic poles being represented as electric dipoles. A general three dimensional multi-spacecraft multipole EM analysis is presented in Section 5.4.1.

The force between two electric charges written in the vectorial form is given by:

$$\overrightarrow{F_{s,t}} = \frac{kq_s q_t}{\left|\overrightarrow{r_{s,t}}\right|^3}\overrightarrow{r}_{s,t} \tag{5.3}$$

where k is Coulomb's constant, q_s and q_t are the two interacting electric charges and $\overrightarrow{r}_{st}$ is the position vector from pole s to pole t. Using this electric dipole analogy, the overall force acting on each magnet is simply the sum of all the forces generated from the interaction between the poles on the magnet of interest to all the poles on the other magnet. The force on the magnet m is:

$$\overrightarrow{F_m} = \sum_{n=1}^{N} \sum_{a=1}^{M} \sum_{b=1}^{N} \overrightarrow{F_{ab,mn}} \tag{5.4}$$
$$a \neq m$$

where EM forces due to the poles on the same magnet are not considered. In the case of a two spacecraft ($M = 2$) with dipole magnets ($N = 2$), the force acting on the first spacecraft is:

$$\overrightarrow{F_1} = \overrightarrow{F_{21,11}} + \overrightarrow{F_{22,11}} + \overrightarrow{F_{21,12}} + \overrightarrow{F_{22,12}} \tag{5.5}$$

with the force acting on the second spacecraft simply being equal and opposite this force.

To relate the constant k to the magnetic constant, consider the case where the axes of the charges are aligned as shown in Figure 5.1 ($\theta_1 = \theta_2 = 0$ in Figure 5.2). The total force acting on the first magnet, broken down into the dipole interactions, is:

$$F_{1x} = kq_1q_2\left[-\frac{1}{s^2} + \frac{1}{(s+2l)^2} + \frac{1}{(s-2l)^2} - \frac{1}{s^2}\right] \tag{5.6}$$

where s is separation between the two dipoles and $2l$ is the length of each dipole. Note that the force shown in the equation acts only along the axis of both magnets since they are aligned.

For spacecraft formation flight considerations, the separation between the dipoles is very large in comparison with the size of the dipoles (i.e. $s \gg 2l$). As such, the two terms that involve the $2l$ term can be expanded to:

$$\frac{1}{(s+2l)^2} = \frac{1}{s^2}\frac{1}{\left(1+\frac{2l}{s}\right)^2}$$

$$= \frac{1}{s^2}\left[1 - 2\left(\frac{2l}{s}\right) + 3\left(\frac{2l}{s}\right)^2 + \text{HOT}\right] \tag{5.7}$$

and

$$\frac{1}{(s-2l)^2} = \frac{1}{s^2}\left[1 + 2\left(\frac{2l}{s}\right) + 3\left(\frac{2l}{s}\right)^2 + \text{HOT}\right] \tag{5.8}$$

Substituting these equations back into Equation 5.6 and ignoring the higher order terms, the force experienced by the first magnet is:

$$F_1 = \frac{24kq_1q_2l^2}{s^4} \tag{5.9}$$

Comparing this with the electromagnet equation given by Equation 5.2 and setting $s = B$, the EM force using the electric charge representation is obtained by making the following substitution:

$$k = \frac{\mu_o \pi \chi^2 a^4}{16l^2} \tag{5.10}$$

and the electric charges representing:

$$q_1 = n_1 i_1$$
$$q_2 = n_2 i_2$$

(5.11)

The analysis in the next four sections is based upon the dipole representation of the electromagnets in two dimensional space. This dipole representation seems to be adequate when large motions are considered. However, as will be shown in Section 5.4, the dipole representation is not adequate when the controllability issue of the system is explored. A more general multipole representation in three dimensional space will be presented then.

5.2 Maximizing Mission Efficiency

The objective of this section is to derive the fundamental relations for optimizing the mission efficiency of rotating separated spacecraft interferometers under EMFF. The measure of mission efficiency is science productivity divided by mission cost. In this analysis, science productivity is defined as rotation rate because the faster an interferometric version of the TPF telescope can rotate, the quicker it can survey the region around a potential terrestrial-planet-supporting star and therefore the more stars it can survey in a given amount of time. Of course, once this rotation rate becomes high enough, photon starvation will limit the rotation rate due to the need to achieve a certain signal-to-noise ratio. Cost is crudely defined as system mass. The productivity per cost is improved when either rotation rate is increased or mass is reduced. Maximizing mission efficiency entails calculating the required mass, generated force, and resulting rotation rate.

5.2.1 Two Spacecraft Without Magnetizable Cores

Consider the two spacecraft example shown in Figure 5.1. Assuming that both the spacecraft and coil designs are identical, the mass of each spacecraft comprises the core bus and payload (m_o), the EM coil (m_{coil}), and the solar array (m_{sa}):

$$m_{sc} = m_o + m_{coil} + m_{sa}$$

(5.12)

Obviously, other mass elements can be included to account for other power sub-system elements, etc. However, the mass elements modeled here do capture, at the coarsest level, the trades between coil size and consumed power.

The mass of the coil equals its density (ρ_c) times its volume (conductor length l_c times cross-sectional area A_c), which in turn depends on coil radius (a), conductor radius (r), and number of turns in the coil (n):

$$m_{coil} = l_c A_c \rho_c = (2\pi an)(\pi r^2)\rho_c = 2(\pi r)^2 na\rho_c \tag{5.13}$$

The solar array mass equals power (P) divided by specific power (P_w), or Watts generated per kilogram of solar array:

$$m_{sa} = \frac{P}{P_w} = \frac{i^2 R}{P_w} = \frac{i^2}{P_w}\frac{\rho_c l_c}{A_c} = \frac{i^2}{P_w}\rho_c\frac{2\pi an}{\pi r^2} = 2\left(\frac{i}{r}\right)^2\frac{\rho_c an}{P_w} \tag{5.14}$$

Power depends on resistance (R) which, in turn, depends on resistivity (ρ_c) and conductor geometry. To ensure that the coil is appropriately sized to handle the required current loading, a relationship between the cross-sectional radius of the coil and the current loading is formed:

$$A_m \le \frac{i}{\pi r^2} \tag{5.15}$$

where A_m is the current to cross-sectional area ratio limit. For gage wire application, this limit is set at 6 amps per square mm. To obtain the minimum mass design, the minimum limit on the radius is used. The combined coil and solar array mass can be re-written as:

$$m_{coil} + m_{sa} = 2\pi nia^2\left[\frac{\rho_c A_m^2 + \rho_c P_w}{A_m P_w}\right] \tag{5.16}$$

where the radius of the coil is eliminated from the equation. Now that total mass and therefore cost is modeled, the generated centripetal force can be used to derive rotation rate and therefore productivity. From Equation 5.2, the generated force for two identical spacecraft without a magnetizable core is:

$$F_M = \frac{3}{2}\mu_o\pi\frac{n^2 i^2 a^4}{B^4} \tag{5.17}$$

Equating this magnetic force to the centripetal force (Equation 5.1) allows the rotation rate to be found:

$$\omega = \sqrt{\frac{3\mu_o\pi}{B^5}} \frac{nia^2}{\sqrt{m_{sc}}} \tag{5.18}$$

As expected, increasing mass and separation distance reduces rotation rate while increasing amp-turns (ni) and the area enclosed by the coil (a^2) increases rotation rate.

By defining a mission efficiency metric (J) that divides rotation rate by total system mass (m_{sys}), increasing coil and solar array masses drive the metric downward while increasing rotation rate drives the metric up:

$$J = \frac{\omega}{c_o m_{sys}} = \frac{\omega}{c_o 2 m_{sc}} = \frac{nia^2}{2c_o m_{sc}^{3/2}} \tag{5.19}$$

where

$$m_{sys} = 2m_{sc} \tag{5.20}$$

and

$$c_o = \sqrt{\frac{3\mu_o\pi}{B^5}} \tag{5.21}$$

Maximizing the metric with respect to the number of turns in the coil:

$$\frac{\partial J}{\partial n} = 0 \Rightarrow n_{opt} = \frac{m_o}{\pi ai\left(\frac{p_c A_m^2 + \rho_c P_w}{P_w A_m}\right)} \tag{5.22}$$

As expected, more coil turns are needed for more massive payloads and core buses while less coil turns are needed as coil diameter increases. This relationship for the optimum number of turns can then be used to update the total mass:

$$m_{sc}\Big|_{n_{opt}} = 3m_o \tag{5.23}$$

This is a surprisingly simple result that states that the optimum total mass of the spacecraft is simply a function of the payload and associated bus mass. The mission efficiency metric can also be updated giving:

$$J\big|_{n_{opt}} = \frac{a}{6\sqrt{m_o}} \sqrt{\frac{\mu_o}{\pi B^5}} \left[\frac{P_w A_m}{p_c A_m^2 + \rho_c P_w}\right] \tag{5.24}$$

While the maximum efficiency depends upon payload, solar array, and conductor properties, which are likely fixed by current technology, it is proportional to coil radius. The larger the coil, the more area it encloses and the more efficient the design. Obviously, the need to mount and support large coils will eventually place an upper limit on achievable coil geometry.

Note that this updated mission efficiency is in fact independent of the current loading in the coil. Hence, Equation 5.22 not only gives the optimal number of turns in the coil, but the optimal amp-turns of the coil:

$$ni\big|_{opt} = \frac{m_o}{\pi a \left[\dfrac{p_c A_m^2 + P_w \rho_c}{P_w A_m}\right]} \tag{5.25}$$

This has been an interesting exercise in that it has revealed that there are clearly preferable designs within the design trade space. However, it has only captured a few of the most important design issues. The following subsections expand upon this analysis to include additional spacecraft as well as magnetizable cores within the coils to enhance field strength.

5.2.2 Adding a Combiner Spacecraft

Clearly, optical interferometry requires that a combiner system be placed at an equal optical path length location. In this example, that location will be assumed to be at the center of rotation. This requires the addition of a third, combiner spacecraft. Therefore, assume all satellites are identical and a third identical satellite is placed at the center of rotation. Now, summing the forces on a collector spacecraft and equating that to the requisite centripetal force gives:

$$\frac{1}{2} m_{sc} \omega^2 B = \frac{3}{2} \mu_o \pi n^2 i^2 a^4 \left[\frac{1}{(B/2)^4} + \frac{1}{B^4}\right] \tag{5.26}$$

where the two terms in parentheses confirm that two spacecraft exert attractive forces on the third, although the force from the other collector spacecraft is only one-sixteenth the force from the combiner. Now the efficiency metric is:

$$J = \frac{\omega}{c_o m_{sys}} = \frac{\omega}{c_o 3 m_{sc}} = \frac{\sqrt{17}}{3} \frac{nia^2}{m_{sc}^{3/2}} \tag{5.27}$$

Notice that this expression for the three spacecraft mission efficiency is identical to that for two spacecraft with the exception of the numerical constant. Therefore, the optimization process, with respect to the design parameters, is identical yielding the same optimum values. As a result, the relative efficiency between the three and two spacecraft arrays can be found by dividing Equation 5.27 by Equation 5.19 to give:

$$\Sigma = \frac{J_3}{J_2} = \frac{\dfrac{\sqrt{17}}{3} \dfrac{nia^2}{m_{sc}^{3/2}}}{\dfrac{nia^2}{2 m_{sc}^{3/2}}} = \frac{2}{3}\sqrt{17} = 2.75 \tag{5.28}$$

For the system without a core, adding a combiner almost triples the mission efficiency due to the placement of an identical spacecraft at the midpoint of the two spacecraft array and thereby inserting an electromagnet into the system that exerts a force on the collector spacecraft that is sixteen times that exerted by the other collector.

5.2.3 Two Spacecraft With Magnetizable Cores

By wrapping the coil around a magnetizable material, such as steel, which increases the magnetic susceptibility of the coil's interior volume, a significant improvement in electromagnetic efficiency can be realized. The effect of having a magnetizable core is to introduce a multiplier (χ) in front of the coil's ampere-turns. This allows the geometry of the coil to be greatly reduced so that most of the spacecraft is outside of the region of high magnetic field strength. In the following development, it is assumed that the coil conductor is wrapped tightly along the entire length of the core and that the longitudinal axes of the coils are again co-linear.

The balance between electromagnetic attraction and centripetal force is now:

$$F = \frac{3}{2}\frac{\mu_o}{\pi}\frac{\mu_a^2(\chi+1)^2}{B^4} = \frac{1}{2}mB\omega^2 \tag{5.29}$$

where
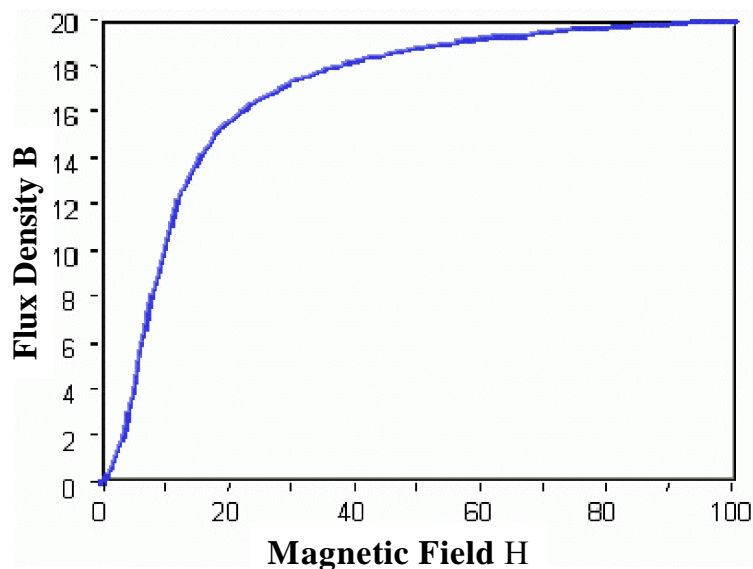
Figure 5.3   Example of magnetization intensity as a function of
applied magnetic field for a ferromagnetic material.

$$\mu_a = ni\pi a^2 \tag{5.30}$$

is the magnetic moment that results from the conducting coil.

The susceptibility of the ferromagnetic material is actually a function of the applied magnetic field. Shown in Figure 5.3 is the magnetization curve for a ferromagnetic material as a function of the applied field. When the applied magnetic field is low, the magnetization contribution from the core is also low. However, as the strength of the applied field is increased, the magnetization effect increases at a rather rapid rate till it saturates at about 80 units. Beyond this saturated applied field, no amount of applied magnetic field can increase the magnetic field contribution from the core as all the magnetic poles in the core are already aligned with the applied field.

An example of the core susceptibility plotted as a function of the applied field is shown in Figure 5.4. In this plot, the saturation effect is clearly observed when the applied field is in the order of 10 units. As the applied field is increased, the effective susceptibility of the material decreases as the magnetization effect of the material is already at its maximum. Hence, for a given electromagnet, the amplification effect of increasing the current in the coils beyond the saturation point of the core material is significantly reduced. Beyond this point, incremental magnetic fields come predominantly from the current in the conducting loops.
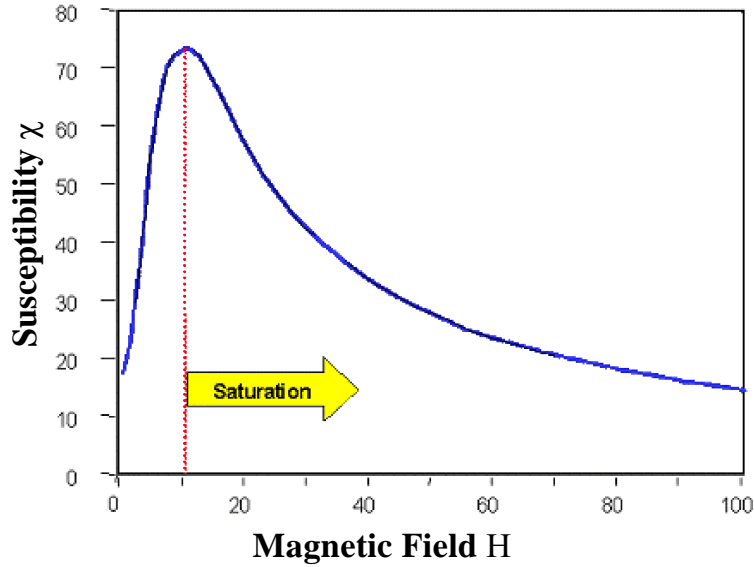
Figure 5.4   Relative susceptibility as a function of applied mag-
netic field for a ferromagnetic core.

The applied magnetic field can be determined from the number of amp-turns in the coil by assuming an infinite solenoid approximation:

$$\beta = \mu_o H_m = \frac{\mu_o ni}{2l} = \frac{\mu_o ni\alpha}{2a} \tag{5.31}$$

where the substitution

$$a = \alpha l \tag{5.32}$$

is made since a high aspect ratio for the coil, and therefore the core, must be selected to validate the approximation. The variable a corresponds to the radius of the coil/core while l is the half length of the core.

The total mass of the spacecraft can be written in terms of the applied magnetic field required to compensate for the centripetal load experienced by the spacecraft:

$$m_{sc} = m_o + \mu_a \left[\frac{\mu}{m}\right]_{coil}^{-1} + \chi\mu_a \left[\frac{\mu}{m}\right]_{core}^{-1} \tag{5.33}$$

where $\left[\dfrac{\mu}{m}\right]_{coil}$ and $\left[\dfrac{\mu}{m}\right]_{core}$ are the magnetic moment per unit mass for the coil and core respectively. Combining the solar array and coil mass required to generate the applied magnetic field, the magnetic moment per unit mass for the solar array and coil combination is:

$$\left[\frac{\mu}{m}\right]_{coil} = \frac{a}{2}\left[\frac{A_m P_w}{P_w \rho_c + p_c A_m^2}\right] \tag{5.34}$$

which in fact gives the same solar array and coil mass expression given by Equation 5.16 when its inverse is multiplied with the applied magnetic moment (μ_a). The magnetic moment per unit mass for the ferromagnetic core can also be written in this form:

$$\frac{\chi H_m}{\rho_s} = \frac{niA}{2lA} = \left[\frac{\mu}{m}\right]_{core} \tag{5.35}$$

since H_m is the applied magnetic field generated by coil. Since the magnetic flux generated by the core due to the applied field can be written as:

$$B_s = \chi\mu_o H_m \tag{5.36}$$

the magnetic moment per unit mass for the core is simply:

$$\left[\frac{\mu}{m}\right]_{core} = \frac{B_s}{\mu_o \rho_s} \tag{5.37}$$

and the mass of the ferromagnetic core can be written as:

$$m_{core} = \chi\mu_a \left[\frac{\mu}{m}\right]_{core}^{-1} = \rho_s(\pi a^2)\left(2\frac{a}{\alpha}\right) \tag{5.38}$$

where the variable a can be explicitly be re-written as:

$$a = \left[\frac{\alpha\chi\mu_a}{2\rho_s\pi}\left[\frac{\mu}{m}\right]_{core}^{-1}\right]^{1/3} \tag{5.39}$$

Substituting this term back into Equation 5.34, the total mass of the spacecraft is simply a function of the applied magnetic field:

$$m_{sc} = m_o + \mu_a^{\frac{2}{3}} \left[\frac{P_w \rho_c + p_c A_m^2}{A_m P_w} \right] \left[\frac{2^4 \pi \rho_s}{\alpha \chi} \right]^{\frac{1}{3}} \left[\frac{\mu}{m} \right]_{core}^{\frac{1}{3}} + \chi \mu_a \left[\frac{\mu}{m} \right]_{core}^{-1} \tag{5.40}$$

and since the force balancing equation is also written in terms of the applied magnetic moment, the mission efficiency design can now be determined in terms of the applied magnetic moment.

Consider for the case where the applied magnetic moment for the system is known. The total spacecraft mass of the system is now a function of the applied magnetic field due to the magnetic moment per unit mass terms. Taking the derivative of this spacecraft mass with respect to the applied magnetic field and setting it to zero, the minimum mass configuration is obtained when the system is designed to operate at the following susceptibility condition:

$$\frac{\partial m_{sc}}{\partial H} = 0 \Rightarrow \frac{\partial \chi}{\partial H_m} = -\frac{\chi}{H_m} \tag{5.41}$$

and for a ferromagnetic material with a maximum susceptibility of 5000 and a magnetization flux of 2.45 Tesla, this condition equates to:

$$\frac{\partial \chi}{\partial H_m} = -12.8 \approx 0 \tag{5.42}$$

which is approximately zero when compared to the susceptibility value of 5000. This condition basically indicates that the minimum mass configuration is obtained when EM system is designed to operate slightly beyond the saturation point, where the largest magnetization effect of the core can be realized using the least applied magnetic field. For the ferromagnetic core considered in this study, the magnetic moment per unit mass at the saturation point is:

$$\left[\frac{\mu}{m} \right]_{core} = \frac{B_s}{\mu_o \rho_s} = 252 \frac{Am^2}{kg} \tag{5.43}$$

Substituting this back into the mass equation, the mission efficiency metric is now simply a function of the applied magnetic moment (μ_a). The optimal mission efficiency configuration with respect to the applied magnetic moment can be determined by taking the derivative of the mission efficiency metric and setting it to zero to get:

TABLE 5.1 Optimized design parameters for two spacecraft array without and with magnetizable cores.

Coil/core	Without Core	With Core
Diameter	N/A	$a_{opt} = \sqrt[3]{\dfrac{m_o \alpha}{2\pi\rho_s}}$
Length	N/A	$l_{opt} = \sqrt[3]{\dfrac{m_o}{2\pi\alpha^2\rho_s}}$
Amp-turns	$ni\big|_{opt} = \dfrac{m_o}{\pi a}\left[\dfrac{P_w A_m}{p_c A_m^2 + \rho_c P_w}\right]$	$ni\big|_{opt} = \sqrt[3]{\dfrac{2m_o\rho_s^2}{\pi\alpha^2}}\,\chi^{-1}\left[\dfrac{\mu}{m}\right]_{core}$
Magnetic-moment	$\mu_a\big|_{opt} = a m_o\left[\dfrac{P_w A_m}{p_c A_m^2 + \rho_c P_w}\right]$	$\mu_a\big|_{opt} = 2\dfrac{m_o}{\chi}\left[\dfrac{\mu}{m}\right]_{core}$
Spacecraft		
Mass	$m_{opt} = 3m_o$	$m_{opt} = 3m_o + 2\dfrac{m_o}{\chi}\left[\dfrac{\mu}{m}\right]_{core}\left[\dfrac{\mu}{m}\right]_{coil}^{-1}$
Power	$P_{opt} = 2m_o p_c A_m\left[\dfrac{P_w A_m}{p_c A_m^2 + \rho_c P_w}\right]$	$P_{opt} = 4\dfrac{A_m p_c}{\chi}\left(\dfrac{\pi m_o^2 \rho_s}{\alpha}\right)^{\frac{1}{3}}\left[\dfrac{\mu}{m}\right]_{core}$
Rotation Rate	$\omega_{opt} = a\sqrt{\dfrac{\mu_o m_o}{\pi B^5}}\left[\dfrac{P_w A_m}{p_c A_m^2 + \rho_c P_w}\right]$	$\omega_{opt} = \dfrac{\sqrt{\dfrac{3\mu_o}{\pi B^5}}\,m_o\dfrac{(\chi+1)}{\chi}\left[\dfrac{\mu}{m}\right]_{core}}{\sqrt{3m_o + 2m_o\left[\dfrac{\mu}{m}\right]_{core}\left[\dfrac{\mu}{m}\right]_{coil}^{-1}}}$
System		
Mass	$m_{opt} = 6m_o$	$m_{opt} = 6m_o + 4\dfrac{m_o}{\chi}\left[\dfrac{\mu}{m}\right]_{core}\left[\dfrac{\mu}{m}\right]_{coil}^{-1}$
Efficiency	$J_{opt} = \dfrac{a}{6}\sqrt{\dfrac{\mu_o}{\pi B^5}}\left[\dfrac{P_w A_m}{p_c A_m^2 + \rho_c P_w}\right]$	$J_{opt} = \dfrac{\sqrt{\dfrac{3\mu_o}{\pi B^5}}\,m_o\dfrac{(\chi+1)}{\chi}\left[\dfrac{\mu}{m}\right]_{core}}{2\left(3m_o + 2m_o\left[\dfrac{\mu}{m}\right]_{core}\left[\dfrac{\mu}{m}\right]_{coil}^{-1}\right)^{\frac{3}{2}}}$

$$\frac{\partial J}{\partial \mu_a} = 0 \Rightarrow \mu_{aopt} = 2\frac{m_o}{\chi}\left[\frac{\mu}{m}\right]_{core} \tag{5.44}$$

which can then be inserted back into the relationships for mass and efficiency to yield:

$$m_{opt} = 3m_o + 2\frac{m_o}{\chi}\left[\frac{\mu}{m}\right]_{core}\left[\frac{\mu}{m}\right]_{coil}^{-1} \tag{5.45}$$

and

$$J_{opt} = \frac{1}{2}\sqrt{\frac{3\mu_o}{\pi B^5}}\frac{m_o\left(1 + \frac{1}{\chi}\right)\left[\frac{\mu}{m}\right]_{core}}{\left(3m_o + 2\frac{m_o}{\chi}\left[\frac{\mu}{m}\right]_{core}\left[\frac{\mu}{m}\right]_{coil}^{-1}\right)^{3/2}} \tag{5.46}$$

which are written in terms of all the known parameters. This completes the design.

As opposed to the non-core case, there now exists an optimum coil geometry. The relationships governing the optimum system parameters are given in Table 5.1. Notice that mission efficiency increases with increasing solar array specific power and reduced coil aspect ratio, and decreases with increasing core mass, conductor density, core density, and conductor resistivity. Again, a maximum efficiency exists as a function of the applied magnetic moment (μ_a) from the coil. Unlike without the core, an optimum core/coil length and diameter exist. Smaller core/coil geometries are less massive but also enclose less area.

As with the case when no core was included, the addition of a combiner spacecraft at the center of rotation improves the efficiency of the array. The ratio of improvement is the same as without the core.

5.3 Case Study: TPF

The analysis performed in the previous section is now extended to the five spacecraft TPF interferometer. The relative positions of the spacecraft are shown in Figure 5.5. The TPF interferometer is currently envisioned to be 75 m in total baseline, rotated at a rate of one rotation in every eight hours [Beichman et al, 1999]. In this section, mission parameters specific to the TPF interferome-
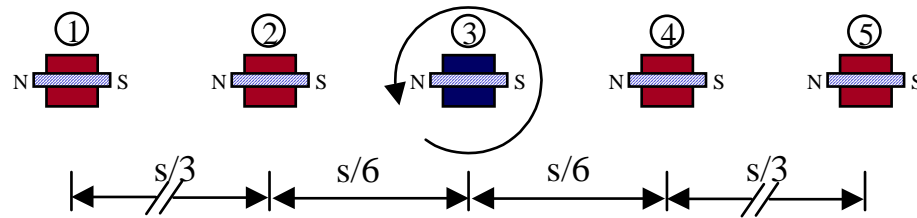
Figure 5.5   Five spacecraft EMFF TPF interferometer.

ter are presented. The best design based upon these parameters is then determined and compared to the proposed TPF system.

5.3.1 Mission Parameters

TPF Spacecraft Dry Mass

The dry mass of the spacecraft is obtained based upon the total spacecraft mass from the TPF book [Beichman et al, 1999]. To fairly compare the various systems, the dry mass of the spacecraft will exclude not only the propellant mass allocated for the TPF mission, but also the propulsion system and the solar array mass that are associated with it. The breakdown of both the combiner and collector spacecraft masses, together with the budgeted power, is shown in Table 4.3.

Conducting Coil

The strength of the magnetic attraction between the spacecraft is proportional to the product of the currents in the conducting coils as indicated in Equations 5.2, 5.26, and 5.29. As such, to minimize the power required, the conducting coils should be made out of materials with low resistivities. Hence, copper is chosen. The density and resistivity of copper at room temperature are 8950 kgm^{-3} and $1.7x10^{-8}$ Ωm, respectively. To conform with gage wire standard, a current per unit area ratio (A_m) limit of 6 Amps/mm^2 is set.

Solar Array

The power required for this EMFF concept is assumed to be generated entirely from the solar arrays. In this study, a specific power of 25 W/kg is assumed for the solar arrays [Larson et al, 1998]. Together with the parameters given by the conducting coil, the magnetic moment per unit mass generated by the coil is:

$$\left[\frac{\mu}{m}\right]_{coil} = \frac{a}{2}\left[\frac{A_m P_w}{P_w \rho_c + p_c A_m^2}\right] = 90a \frac{\text{Am}^2}{\text{kg}} \tag{5.47}$$

Magnetizable Core

The role of the magnetizable core is to serve as magnetic field magnifiers since the EM force is generated by the conducting coils. For the purpose of this study, a steel core with an aspect ratio (α) of 0.1 is chosen. Considering a steel core, the density of the core is 7750 kgm^{-3}. Since the minimum mass configuration is to operate near the magnetic saturation of the core, the magnetic flux and susceptibility at saturation is 2.45 Tesla and 5000 respectively. The corresponding magnetic moment per unit mass is calculated to be 252 Am^{2}kg^{-1}. Comparing with the magnetic moment per unit mass for the coil, the bulk of the magnetic moment contribution comes from the ferromagnetic core when the size of the core is less than 2.8 m. Beyond this core radius, the contribution from the coil becomes more significant than that of the core.

5.3.2 Maximizing Mission Efficiency Design

The Maximizing Mission Efficiency (MME) design methodology outlined in the previous section is now extended to the five spacecraft TPF interferometer. By assuming symmetry, the dynamic constraints that must be satisfied by the two collector spacecraft rotating about the combiner are given by:

$$\frac{m_{sc1}\omega^2 B}{2} = \frac{3}{2}\frac{\mu_o}{\pi}(\chi+1)^2\mu_1\left[\frac{\mu_2}{(B/3)^4} + \frac{\mu_3}{(B/2)^4} + \frac{\mu_2}{(2B/3)^4} + \frac{\mu_1}{B^4}\right] \tag{5.48}$$

and

$$\frac{m_{sc2}\omega^2 B}{6} = \frac{3}{2}\frac{\mu_o}{\pi}(\chi+1)^2\mu_2\left[-\frac{\mu_1}{(B/3)^4} + \frac{\mu_3}{(B/6)^4} + \frac{\mu_2}{(B/3)^4} + \frac{\mu_1}{(2B/3)^4}\right] \tag{5.49}$$

which clearly show the EM force interactions between these spacecraft and all the others in the interferometer. Note that the rotational rates, ω, in both these equations are in fact the same. Equating these two equations to eliminate ω, yields an expression for the magnetic moment (μ_3) in the combiner spacecraft. Dividing either Equation 5.48 or Equation 5.49 by the total mass of inter-

TABLE 5.2 MME design for TPF configuration

Parameters	S/C 1	S/C 2	S/C 3	Total Array
a (m)	0.16	0.02	0.27	-
$2l$ (m)	3.2	0.4	5.4	-
ni (A-turns)	620	72	1050	-
μ (A m^2-turns)	50	0.1	240	-
P (W)	60	0.9	180	-
m_{sc} (kg)	1560	600	5340	9660
ω (rad/s)	-	-	-	1.2×10^{-3}
$J = \omega / m_{tot}$	-	-	-	1.3×10^{-7}
F_{cent} (mN)	89	11	-	-

ferometer and substituting the expression for μ_3, the mission efficiency metric for this system is then a function of applied magnetic moments of the two collector spacecraft:

$$J_{MME} = \frac{\omega}{m_{Tot}} = f(\mu_1, \mu_2) \tag{5.50}$$

In the ideal situation, optimal design using this mission efficiency metric can be determined by simply taking the first derivative of Equation 5.50 with respect to one of the two variables and setting it to zero to obtain the optimal design for that variable. This optimal variable can then be substituted back into Equation 5.50, which makes it dependent on only the remaining variable. This process can then be repeated once more to determine the applied magnetic moment in terms of all the other known parameters. Unfortunately, as the number of spacecraft in the array increases, analytical determination of the optimal solution is no longer practical. However, one can resort to numerical optimization techniques.

Using the *fmincon* optimization routine in the Matlab® numerical package [Mathworks, 2001], the best design obtained is tabulated in Table 5.2. The dimensions of the coil and core in this design seem to be reasonable in that they are not excessively large. However, these dimensions do translate to a rather massive system when compared to the dry mass of the spacecraft of 600 kg. In fact, the overall mass of the system is more than twice the dry mass of the system with most of it residing in the combiner spacecraft. This will then indicate that most of the magnetic attraction contri-

bution comes from electromagnet in the combiner spacecraft. This tends to make sense since the combiner spacecraft is located at the center of the array and the additional mass required does not experience any centripetal load. As for the power requirements, rather low values are required since the system is designed to operate at the saturation point of the ferromagnetic core. These power requirements translate to the applied magnetic field strength of 390 Am^{-1} where the maximum magnetization effect of the core can be utilized. Even though this design maximizes the mission efficiency, the interferometer is rotating at a rate rotation rate of one every 1.5 hours, which is faster than the one rotation per eight hours that is currently specified for the TPF interferometer.

In the next subsection, the optimization is repeated with the rotation rate of the interferometer being specified. The mission efficiency metric is reduced to a mass minimization metric where the dynamic constraints (Equation 5.48 and Equation 5.49) must again be satisfied.

5.3.3 Fixed Rotation Rate Designs

The approach taken here is similar to the one in the previous subsection. First, the applied magnetic moment in the combiner spacecraft (μ_3) is found by equating the two dynamic equations (Equation 5.48 and Equation 5.49). Then, with the rotation rate being specified, an expression for the applied magnetic moment in the inner collector spacecraft (μ_2) is determined from one of the two dynamic equations. Substituting these two current expressions, the total mass of the interferometer can be expressed as a function of the applied magnetic moment in the outer collector spacecraft:

$$m_{Tot} = f(\mu_1) \tag{5.51}$$

as opposed to two in the previous subsection.

Again, the best designs for the various rotation rates are determined using the *fmincon* optimization routine in Matlab® with the results plotted in Figure 5.6. For interferometers that are rotating at low angular rates, the required EM masses are quite low. In fact, the total mass asymptotes to the dry mass of the interferometer (2968 kg) when a zero rotation rate is considered. However, as the rotation rate increases, larger coils and cores are needed to balance the higher centripetal load experienced by the collector spacecraft.
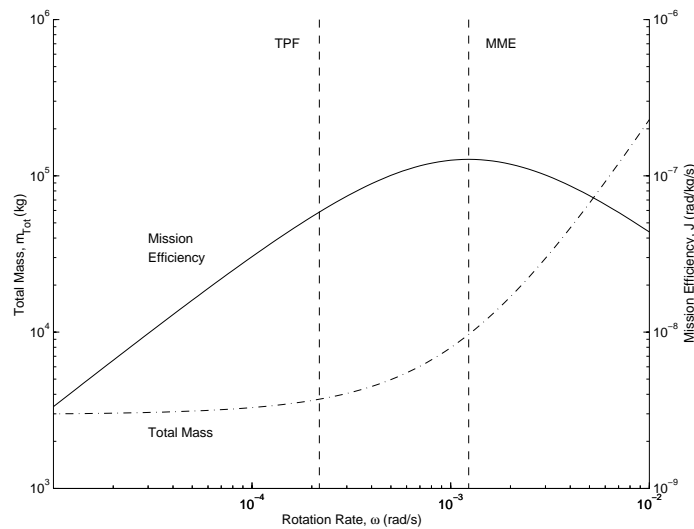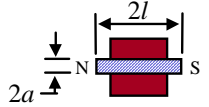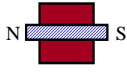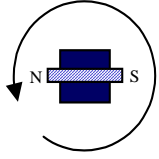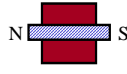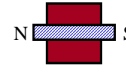
Figure 5.6   Total interferometer mass and mission efficiency as a
function of rotation rate of the interferometer.

The corresponding mission efficiencies are also shown in the figure. An optimum exists where the mission efficiency of the system can longer be improved. Clearly, the preference is to operate the interferometer near this optimum if the rotation rate or the total mass are not subjected to any constraints. However, if constraints exist, the achievable mission efficiency can then be determined together with either the corresponding minimum total mass or maximum rotation rate that is to be expected. The optimum shown in the figure does in fact correspond to the MME design obtained in the previous subsection.

Also shown in the figure is the best EM TPF design based upon the proposed rotation rate of one rotation every eight hours [Beichman et al, 1999]. At this rate, the maximum achievable mission efficiency is only 5.86×10^{-8} rad/kg/s compared with the MME design of 1.27×10^{-7} rad/kg/s. However, this EM TPF design requires only 754 kg of additional EM subsystem mass (3722 kg total mass). Compared with the extra 6703 kg required for the MME design, this EM TPF design is realizable.

Additional design parameters for this EM configuration are tabulated in Table 5.3. The first item shown in the table is the power required for all the spacecraft. Again, similar to the MME design, lower power levels are required for all the spacecraft so that the maximum magnetization effect of

TABLE 5.3   EMFF design for TPF interferometer based upon constant χ.

Power (W)	20	0.4	35	0.4	35
a (mm)	89	13	119	13	89
2l (m)	1.77	0.27	2.37	0.27	2.37
ni (A-turns)	350	50	460	50	350
μ (A m^2-turns)	8.6	~0	20	~0	20
$F_{on\ 1}$ (mN)	$F_{cent} = -1.376$	$F_{12} = 0.010$	$F_{13} = 1.331$	$F_{14} = 0.001$	$F_{15} = 0.035$
$F_{on\ 2}$ (mN)	$F_{21} = -0.010$	$F_{cent} = -0.357$	$F_{23} = 0.366$	$F_{24} = \sim0$	$F_{25} = 0.001$

the core can be obtained using as little applied magnetic field as possible. The dimensions of the core and the coil designs seem to be quite reasonable as well. Both the centripetal and magnetic forces acting on the two collector and combiner spacecraft are also shown in the table. For the outermost spacecraft, the centripetal loading on the spacecraft seems to be the highest, as it is furthest away from the center of the array. To offset the centripetal load, the magnetic attraction from this spacecraft to the combiner spacecraft is the largest. Since the combiner spacecraft does not experience any centripetal load, it makes sense that the required EM mass is concentrated onto this spacecraft. As for the inner collector spacecraft, it requires little EM related mass since the bulk of the attraction force is provided by the combiner spacecraft.

With a total mass of 3722 kg, the EMFF design is in fact within the margins currently allocated for TPF interferometer (4769 kg). As such, the currently designed system can easily be launched on the 6100 kg capacity VentureStar Re-usable Launch Vehicle, the proposed launch vehicle for the TPF interferometer. Should the availability of this launch vehicle becomes an issue, the EMFF interferometer can easily be launched on either Arianespace's Ariane 5 or Lockheed Martin's Proton M launch vehicle. With a core length of only 2.4 m in only one direction, the EMFF spacecraft should not have any issues with the volume constraints on these launch vehicles.

5.3.4 TPF Comparison
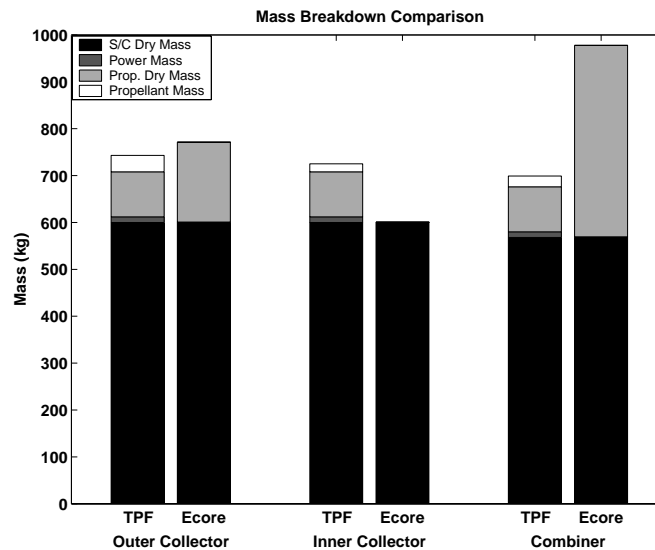
Figure 5.7 Mass comparison between designs from TPF book and
EMFF concept.

To determine the feasibility of the EMFF design as applied to the TPF mission, a comparison with the currently proposed system [Beichman et al, 1999] is shown in Figure 5.7. The total mass of each spacecraft is broken down into the dry mass of the spacecraft, the propulsion-related mass, the propellant mass, and the incremental mass required for the EMFF concept. Based upon this figure, the current system design requires less mass for each spacecraft. However, the current TPF interferometer is only designed to operate for a total lifetime of only five years. Should there be a need to operate the system beyond the five year requirement, more propellant will be required. In contrast, for the EMFF interferometer, no additional mass is required. In fact, the lifetime of the mission is not dependent upon any consumable, but only on the reliability of the system.

A plot of the total system mass as a function of mission lifetime for both these designs is shown in Figure 5.8. The break even point measured in terms of the total system mass is approximately 8.3 years. Should the mission be extended to beyond this 8.3 years lifetime, it makes sense to select the EMFF option.
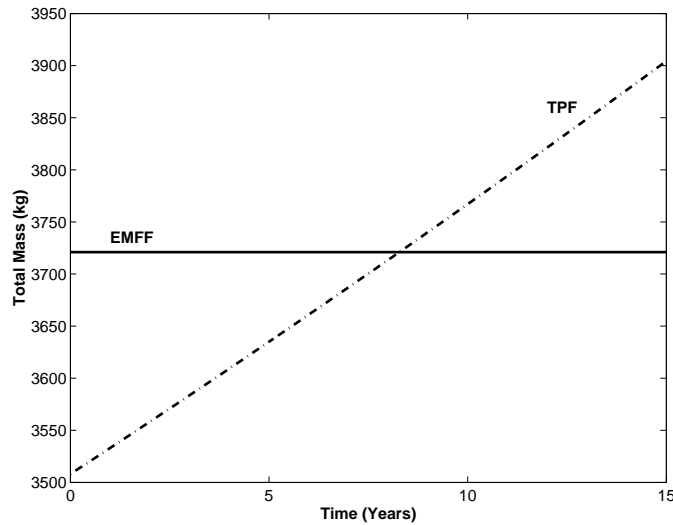
Figure 5.8   Total system mass as a function of mission lifetime.

5.4 Small Perturbation Control

In the previous section, the large motion requirements for the TPF interferometer using the EMFF concept were determined and initial results are quite encouraging for the EMFF concept. This large motion analysis gives an overview estimate of the overall mass and power requirements for the TPF array. It does not, however, say anything about the ability of the system to reject noise introduced into the array.

The TPF interferometer is an infrared detection system. To adequately detect a planet, the optical system of the interferometer must be controlled to at least an order of magnitude less than the observation wavelength (μm). This precision in control is achieved through the use of a multi-stage control system: coarse level control (thrusters) that ranges from meter to centimeter levels of authority, medium level control (optical delay lines) that ranges from centimeter to micrometer levels, and fine level of control (fast steering mirrors) that ranges from micrometer to nanometer levels. It is envisioned that the proposed EMFF concept can adequately provide the course level disturbance rejection capability.

In this section, the requirements to reject small perturbations using only the introduced EMFF concept are determined. A general kinematic formulation for a multi-spacecraft multipole system is
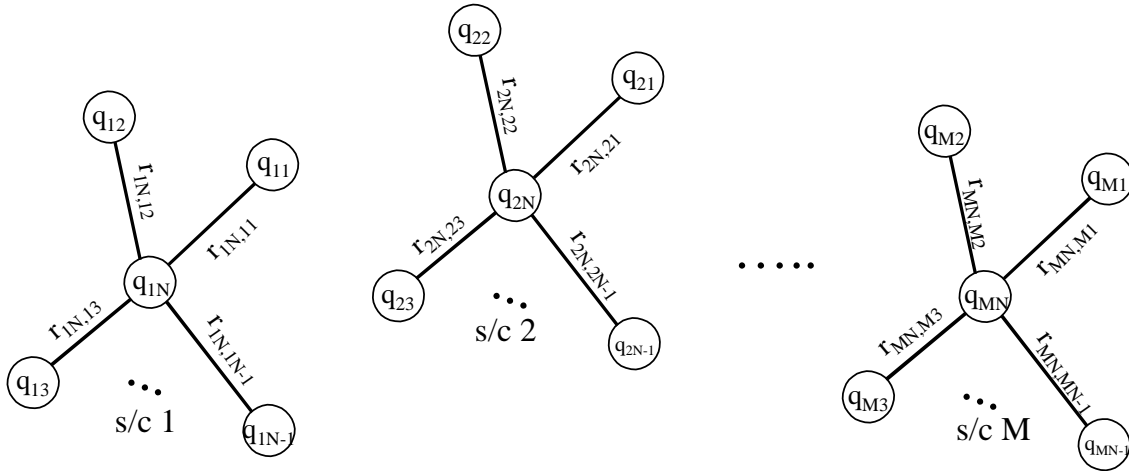
Figure 5.9 Multi-spacecraft Multipole Electromagnets.

first presented. From these kinematic relationships, a state space representation of the system is determined, specifically the dynamic (**A**) and control (**B**) matrices. Using these matrices, the controllability of the system is determined to ensure that the system can adequately reject disturbances in all the required degrees of freedom.

5.4.1 Multi-spacecraft Multipole Electromagnets

The general multi-spacecraft multipole system is shown in Figure 5.9. In this formulation, a general system of M spacecraft, each with N magnetic poles, is considered. The force interaction between two poles is given by Equation 5.3, and the total force acting on the spacecraft is given by Equation 5.4. The acceleration experienced by each spacecraft is then simply the force in Equation 5.4 divided by the individual spacecraft mass:

$$\ddot{\vec{x}}_m = \frac{\vec{F}_m}{m_{sc_m}} \tag{5.52}$$

Since these poles are generally not located at the centroid of the spacecraft, each spacecraft will inherently experience a torque. The torque for each spacecraft can be determined by taking the sum of the cross products between the moment arms and the forces experienced by each pole:

$$\overrightarrow{T}_m = \sum_{n=1}^{N-1} \left[\overrightarrow{r_{mN,\,mn}} \times \sum_{\substack{a\,=\,1 \\ a \neq m}}^{M} \sum_{b=1}^{N} \overrightarrow{F_{ab,\,mn}} \right] \tag{5.53}$$

where the N-th pole of each spacecraft represents the centroid of the spacecraft and $\overrightarrow{r_{mN,\,mn}}$ is the position vector of the n-th pole of the m-th spacecraft relative to the center of the spacecraft, written in the inertial reference frame. This torque equation can then be substituted into the following Euler equation:

$$I_{p,\,m}\overrightarrow{\dot{\omega}_m} = \overrightarrow{T}_m - \overrightarrow{\omega}_m \times I_{p,\,m}\overrightarrow{\omega}_m \tag{5.54}$$

to obtain the angular acceleration vector ($\overrightarrow{\dot{\omega}_m}$) of the m-th spacecraft. Note that this equation can be written in terms of either the inertial reference frame or the respective spacecraft body coordinate system. To simplify the calculation, the latter coordinate system is chosen such that the direction of the three spacecraft angular rates coincide with the principal axes of the spacecraft. The angular acceleration of the spacecraft written in terms of the spacecraft body coordinates is therefore:

$$\overrightarrow{\dot{\omega}_{m,B}} = I_{p,\,m}^{-1} \left[\sum_{n=1}^{N} \sum_{\substack{a\,=\,1 \\ a \neq m}}^{M} \sum_{b=1}^{N} (\overrightarrow{r_{mn}} \times Q_m^T \overrightarrow{F_{ab,\,mn}}) - \overrightarrow{\omega}_m \times I_{p,\,m}\overrightarrow{\omega}_m \right]_B \tag{5.55}$$

Finally, since magnetic monopoles do not exist, the sum of the charges in each spacecraft must equal to zero:

$$\sum_{n=1}^{N} q_{mn} = 0 \tag{5.56}$$

The next step in this section is to rewrite both Equations 5.4 and 5.53 in state space representation. To do so, both the state and control variables for the system must first be defined.

5.4.2 State Space Representation

In an *M*-spacecraft system, the total number of acceleration vectors (Equation 5.52) is simply *M*. These acceleration vectors are defined with respect to the inertial reference frame. Of importance, however, are the *relative* displacements and velocities between the spacecraft since it is the *difference* in path lengths that light rays travel that must be controlled. The position and velocity vectors for the *M*-1 spacecraft relative to the first spacecraft is:

$$\vec{x}_p = \left[\overrightarrow{\Delta x_{1,2}}\ \overrightarrow{\Delta x_{1,3}}\ ...\ \overrightarrow{\Delta x_{1,M}}\ \overrightarrow{\Delta \dot{x}_{1,2}}\ ...\ \overrightarrow{\Delta \dot{x}_{1,3}}\ \overrightarrow{\Delta \dot{x}_{1,M}} \right]^T \tag{5.57}$$

where each relative position (and corresponding relative velocity) consists of the three cartesian coordinate variables:

$$\overrightarrow{\Delta x_{1,m}} = \left[x_{1,m}\ y_{1,m}\ z_{1,m} \right]^T \tag{5.58}$$

making the total number of position and velocity state variables equal to 6*(*M*-1).

The attitude control for each spacecraft is described using a quaternion representation. Although four variables are required, instead of three when using an Euler angle representation, ambiguities that are inherent using Euler angles are completely eliminated. The quaternion variables for each spacecraft in the system are:

$$\vec{\varepsilon}_m = \left[\varepsilon_{1,m}\ \varepsilon_{2,m}\ \varepsilon_{3,m}\ \varepsilon_{4,m} \right]^T \tag{5.59}$$

The angular velocities for the spacecraft, however, are described using only three variables:

$$\overrightarrow{\omega_{m,B}} = \left[\omega_{1,m}\ \omega_{2,m}\ \omega_{3,m} \right]^T_B \tag{5.60}$$

Hence, for each spacecraft, seven variables are required to describe the attitude of the spacecraft and for the entire system, 7*M* variables are required. To adequately describe the system in terms of state space representation, the quaternion rates in terms of the quaternion and angular velocities are given by [Hughes, 1986]:

$$\dot{\vec{\varepsilon}}_{1-3, m} = \frac{1}{2}(\vec{\varepsilon}_{1-3, m}^{\times} + \varepsilon_{4, m}\mathbf{I})\vec{\omega}_{m, B}$$

$$\dot{\varepsilon}_{4, m} = -\frac{1}{2}\vec{\varepsilon}_{1-3, m}^{T}\vec{\omega}_{m, B} \tag{5.61}$$

where the $\vec{\varepsilon}_{1-3, m}$ vector represents the first three quaternion variables, $\varepsilon_{4, m}$ represents the fourth, and **I** represents the identity matrix. The notation $(\ )^{\times}$ represents the formation of the skew-symmetric matrix $\vec{\varepsilon}_{1-3, m}^{\times}$ from the elements of $\vec{\varepsilon}_{1-3, m}$ according to the pattern given by:

$$\vec{\varepsilon}_{1-3, m}^{\times} \equiv \begin{bmatrix} 0 & -\varepsilon_3 & \varepsilon_2 \\ \varepsilon_3 & 0 & -\varepsilon_1 \\ -\varepsilon_2 & \varepsilon_1 & 0 \end{bmatrix} \tag{5.62}$$

To summarize, for a system with M spacecraft, the total number of variables required to adequately describe the system is $13M$-6. In this thesis, these variables are arranged as follow:

$$\vec{x} = \begin{bmatrix} \vec{\Delta x}_{1, 2} & \cdots & \vec{\Delta x}_{1, M} & \vec{\varepsilon}_1 & \cdots & \vec{\varepsilon}_M & \vec{\Delta \dot{x}}_{1, 2} & \cdots & \vec{\Delta \dot{x}}_{1, M} & \vec{\omega}_{1, B} & \cdots & \vec{\omega}_{M, B} \end{bmatrix}^T \tag{5.63}$$

The control variables in this system are the strengths of the charges in the poles. Since the total charge for each N-pole spacecraft must equate to zero (Equation 5.56), the number of control variables for each spacecraft is simply N-1:

$$\vec{u}_m = \begin{bmatrix} q_{m, 1} & q_{m, 2} & \cdots & q_{m, N-1} \end{bmatrix}^T \tag{5.64}$$

and for the entire system, the total number of control variables is $M(N$-1).

The control variables shown in Equation 5.64 assume the relative positions and orientations of the spacecraft are controlled purely by the electromagnets. If these electromagnets are augmented with reaction wheels, the control vector for the m-th spacecraft will be:

$$\vec{u}_m = \begin{bmatrix} q_{m, 1} & q_{m, 2} & \cdots & q_{m, N-1} & w_{m, 1} & w_{m, 2} & w_{m, 3} \end{bmatrix}^T \tag{5.65}$$

where $w_{m, i}$ represents the acceleration of the reaction wheel in the i-th direction in an m-th spacecraft.

5.4.3 Linearization

The dynamic (**A**) and control (**B**) matrices in the control framework are obtained by linearizing the equations of motions with respect to the state and control variables. For this, both the force and torque equations must be explicitly expressed in terms of the state and control variables.

In both the force and torque equations, the EM forces are directly dependent on the position vectors between the poles of interest:

$$\overrightarrow{F_{ab,\,mn}} = \frac{kq_{mn}q_{ab}}{\left|\overrightarrow{r_{ab,\,mn}}\right|^3}\overrightarrow{r_{ab,\,mn}} \tag{5.66}$$

where the product between the two charges (q_{mn} and q_{ab}) indicates whether the force between the poles is attractive. Since the N-th node of each spacecraft is defined as the centroid of the space-craft, the position vector $\overrightarrow{r_{ab,\,mn}}$ can then be rewritten in terms of the state variables given by Equation 5.63:

$$\overrightarrow{r_{ab,\,mn}} = \overrightarrow{\Delta x_{1,\,m}} - \overrightarrow{\Delta x_{1,\,a}} + Q_m\overrightarrow{r_{mn}} - Q_a\overrightarrow{r_{ab}} \tag{5.67}$$

where the first two terms are position vectors of the two spacecraft relative to the first one, and Q_m and Q_a are the rotational matrices describing the orientation of the respective spacecraft in the inertial reference frame using the quaternion variables:

$$Q_m = \begin{bmatrix} \varepsilon_1^2 - \varepsilon_2^2 - \varepsilon_3^2 + \varepsilon_4^2 & 2(\varepsilon_1\varepsilon_2 - \varepsilon_3\varepsilon_4) & 2(\varepsilon_1\varepsilon_3 + \varepsilon_2\varepsilon_4) \\ 2(\varepsilon_1\varepsilon_2 + \varepsilon_3\varepsilon_4) & -\varepsilon_1^2 + \varepsilon_2^2 - \varepsilon_3^2 + \varepsilon_4^2 & 2(\varepsilon_2\varepsilon_3 - \varepsilon_1\varepsilon_4) \\ 2(\varepsilon_1\varepsilon_3 - \varepsilon_2\varepsilon_4) & 2(\varepsilon_2\varepsilon_3 + \varepsilon_1\varepsilon_4) & -\varepsilon_1^2 - \varepsilon_2^2 + \varepsilon_3^2 + \varepsilon_4^2 \end{bmatrix}_m \tag{5.68}$$

The $\overrightarrow{r_{mn}}$ and $\overrightarrow{r_{ab}}$ vectors are the position vectors of the poles relative to the center node of the respective spacecraft written in the spacecraft body frame. Making this substitution into Equations 5.52 and 5.54, the position and rotation equations of motions are written entirely in terms of the state variables defined in Equation 5.63.

The final step in the process is to linearize the equations of motions with respect to both the state and control variables. Expanding the two equations of motion about a nominal trajectory and

ignoring second and higher order terms, the general linearization of these equations can be written as:

$$\dot{\vec{x}} = \frac{\partial}{\partial \vec{x}} f(\vec{x}, \vec{u}) \Big|_{(\vec{x}_o, \vec{u}_o)} \vec{x} + \frac{\partial}{\partial \vec{u}} f(\vec{x}, \vec{u}) \Big|_{(\vec{x}_o, \vec{u}_o)} \vec{u} \tag{5.69}$$

where evaluation of the partial derivative with respect to $\vec{x}$ is required to fill in the **A** matrix while that with respect to $\vec{u}$ is for the **B** matrix.

A & B Matrix Organization

The generation of the **A** and **B** matrices can be obtained by simply taking the partial derivative of the linear and angular acceleration equations with respect to both the state and control variables. In this section, only a summary of the organization of these matrices is presented. For a full derivation of the entries in the **A** and **B** matrices, the reader is referred to Appendix A. The corresponding Matlab code written to automate the generation of these matrices is also presented in Appendix A.

Based upon the state and control vector organizations (Equations 5.63 and 5.64), the resultant **A** matrix is organized as follows:

$$(5.70)$$

It is a 13*M* - 6 square matrix with a number of distinct features. The first is an identity matrix relating the rates of the state variables on both sides of the dynamic equation. The second row is the result of using the quaternion variables to represent the orientation of each spacecraft. These two entries ($A_{b,b}$ and $A_{b,d}$) are block diagonal since the orientation description of each spacecraft is independent of each other. Then there is the fully populated bottom left corner of the matrix. These entries comprise both the relative linear and angular accelerations of all the spacecraft differentiated with respect to the state variables. Since the linear and the angular accelerations of the spacecraft are affected by the orientation and the relative separations of the spacecraft, the resulting square matrix is of the size 7*M* - 3. The final entry in the matrix results from the angular rates that exist in Equation 5.54.

The corresponding **B** matrix is given by:

$$(5.71)$$

where the first two rows in the matrix are simply zero since the control variables exist only in the force and torque equations. This (13*M* - 6) x *M*(*N* - 1) matrix only considers *N* - 1 control variables for each spacecraft as the constraint in Equation 5.56 has already been taken into account.

In the next subsection, the controllability issues for a system of EMFF spacecraft are investigated. The **A** and **B** matrices for the N spacecraft system can be easily generated using the Matlab code given in Appendix A. To demonstrate the application of the code, the results for a two spacecraft system in two dimensional space are presented. Control issues using various pole configurations are also discussed.

5.4.4 Controllability

The controllability for a separated spacecraft interferometer using the EMFF concept are explored by first considering a two spacecraft system. Both the control matrices, **A** and **B**, are needed to obtain the controllability matrix, C:

$$C = \begin{bmatrix} B & AB & A^2B & \dots & A^{n-1}B \end{bmatrix} \tag{5.72}$$

where n is the size of the square matrix **A**. In order for the system to be fully controllable, matrix C must be full rank. Or simply put, it must be rank n.

Dipole

The input parameters for to the Matlab code must first be generated. To do so, the two spacecraft are assumed to be at rest with their magnetic dipoles aligned as shown in Figure 5.1. To obtain realistic dynamics, these two spacecraft will assume the design obtained for the outermost spacecraft given in Table 5.3. Together with the physical properties specified in Section 5.3, the inputs for these two spacecraft are generated and exemplified in Appendix A.2.1.

Since we are considering only a simplified two-dimensional case, the **A** and **B** matrices obtained from the code contain states that are uncontrollable, i.e. in the z direction. As such, to appropriately determine the rank of the C matrix, the size of these control matrices must be truncated. The $13M$ - 6 square **A** matrix can be reduced to a $7M$ - 4 square matrix by removing the both the differential position and velocity z state variables, the first two of the four quaternion variables and the first two of the three rotation variables for each spacecraft. As for the B matrix, only the corresponding rows need to be removed. As such, for the two spacecraft example, these new **A** and **B** matrices can be obtained by removing the 3-rd (Δz), 4-th and 5-th ($\varepsilon_{1,1}$, $\varepsilon_{2,1}$), 8-th and 9-th ($\varepsilon_{1,2}$,
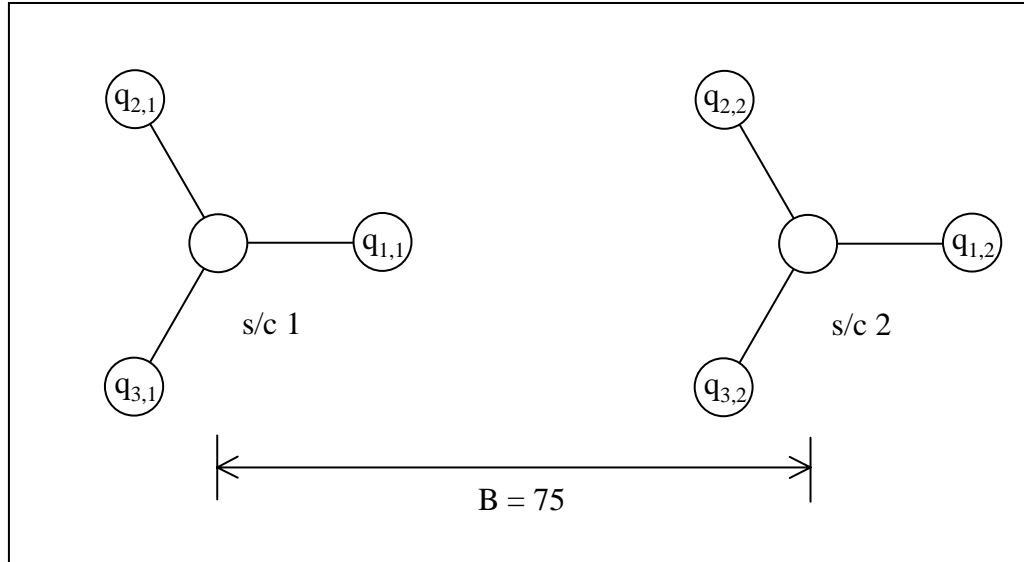
Figure 5.10   Two spacecraft Y-pole configuration.

$\varepsilon_{2,2}$), 11-th ($\Delta \dot{z}$), 15-th and 16-th ($\omega_{1,1}$, $\omega_{2,1}$), and 18-th and 19-th ($\omega_{1,2}$, $\omega_{2,2}$) rows and the corresponding columns from the **A** matrix.

Note that both control matrices now contain ten rows. However for a two spacecraft system in two-dimensional space, there should only be eight state variables: two for the relative x and y position variables, two for the corresponding velocities, one each for rotation for each spacecraft about the z axis and one each for the corresponding rotation rates. This seem to contradict the ten state variables given by the new control matrices. This difference comes from the fact that a quaternion representation is used to describe the spacecraft rotation variables. Instead of the normal three rotation variables, the quaternion representation requires four variables. However, the quaternion variables for each spacecraft must also satisfy the following equation:

$$\varepsilon_1^2 + \varepsilon_2^2 + \varepsilon_3^2 + \varepsilon_4^2 \; = \; 1 \tag{5.73}$$

When reducing the original control matrices, the last two of the four quaternion variables for each spacecraft must be maintained since they are not necessarily zero. Therefore, in order to determine the controllability of this reduced system, the rank of the C matrix needs to be only eight.

The reduced **A** and **B** matrices for this two spacecraft dipole example gives a controllability matrix with a rank of only two. Looking at Figure 5.1, one can intuitively observe that only the position

and velocity along the vector connecting the spacecraft can be controlled by varying the currents in the spacecraft. It would seem to also make sense that it would not be possible to control all eight states with only two control variables.

Y-pole

Instead of the dipole, a two spacecraft system with three poles each is considered. The poles are arranged such that they are evenly distributed at 120° apart, as shown in Figure 5.10. In this thesis, this configuration is known as the Y-pole.

The rank of the controllability matrix for using the Y-pole configuration is eight. Compared to the dipole case, two more control variables have been added while the number of state variables that need to be controlled remains the same. Although the number of variables is still eight, the number of directions that need to be controlled is only four. So, the four control variables available for the two spacecraft seem to be adequate to control the system.

TPF 2-D Case

Extending the analysis to the five spacecraft TPF interferometer, full controllability of the interferometer is only achieved if a rank of 26 is achieved for the *C* matrix. In the case when all the spacecraft are fitted with the dipole configuration, a rank of only eight is achieved. However, when the Y-pole configuration is considered, the rank of the system is found to be 26. This clearly indicates that full controllability of the interferometer in two-dimensional space can only be achieved if the number of poles assigned for each spacecraft is at least three. Note that the number of control variables in this case is only ten (five spacecraft, each with two control variables) compared to the 13 independent state variables.

TPF 3-D Case

Further extending the analysis to consider the TPF interferometer in the three dimensional space indicates that a four-pole configuration must be implemented before full controllability of the interferometer can be achieved. For this full-blown three-dimensional case, the full rank of 54 is only achieved when all four poles on each spacecraft are arranged such that they are not contained in the same plane. A possible configuration is to place the nodes on the vertices of a triangular-
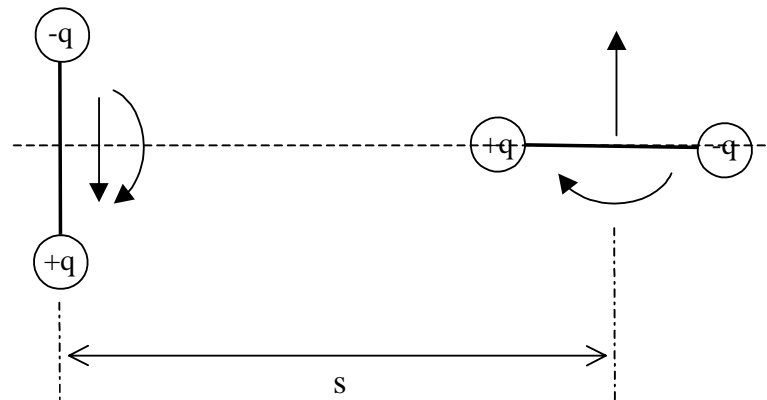
Figure 5.11   Orthogonal dipole interaction [Miller et al, 2002].

based pyramid. Again, similar to the previous case, the number of control variables (15) required is actually less than the number of independent state variables (27).

5.5 Further Considerations

The significant benefits that can be reaped from using a propulsion system that does not require expenditure of any propellant warrant further exploration. In this section, several promising concepts are considered for future work.

Spin-up (Transient)

In this thesis, the steady-state operation (Section 5.3) and preliminary controllability issues (Section 5.4) associated with a five spacecraft interferometer have been discussed. In the steady-state operation scenario, the assumption is that the array is already spinning at the appropriate rate. There is, however, the issue as to how to spin-up the array in the first place. In this section, a summary of this spin-up work done by researchers at the MIT Space System Laboratory is presented [Miller et al, 2002]. Note that this work is still at a very preliminary stage.

The spinning-up of the interferometer made possible through EMFF is the ability to provide 'torque at a distance' [Miller et al, 2002]. Dipoles that are oriented orthogonally to each other, as shown in Figure 5.11, have the ability to create torques on each other while pushing each other in opposing directions. Together with the use of reaction wheels to generate the counteracting
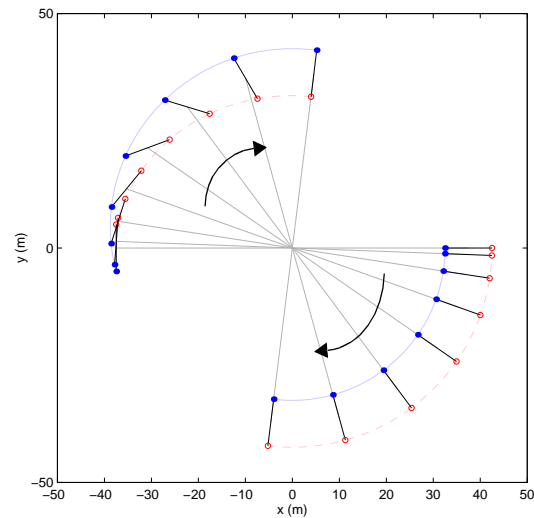
Figure 5.12 Two spacecraft EMFF spin-up maneuver [Miller et al, 2002].

torques to maintain the relative orientation of the two dipoles, the dipoles can be made to rotate about their common center, thus the spinning-up process.

The profile for two spacecraft performing the spin-up maneuver is shown in Figure 5.12, where solid dots represent the positive pole and the circles represent its negative counterpart. The maneuver begins with the two dipoles at right angles to one another, since at zero angular velocity, no centripetal force is necessary. As the spacecraft begin to move, the dipoles are turned slightly toward parallel, to provide the necessary radial force. Finally, as the maximum desired rotation rate is achieved, the dipoles are completely aligned, so that no additional torque is provided. Both the overall strength and direction of the force and torque, as well as the ratio of the two, can be varied, so that a great variety of motions exist.

The ability to spin the array is not limited to the two spacecraft case. Figure 5.13 shows a similar plot for the five spacecraft representative of the TPF mission. Here we can see that alternating spacecraft have dipoles that are nearly orthogonal to one another at the start of the rotation. This is indicative of the primary torques being generated by a spacecraft's nearest neighbors, since the force law drops off rapidly with distance.
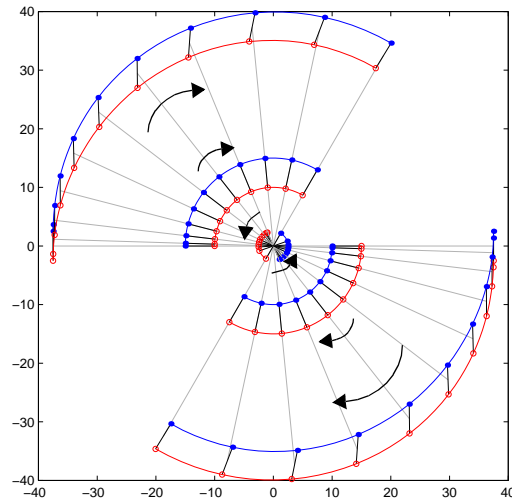
Figure 5.13   Five spacecraft EMMF spin-up maneuver [Miller et al, 2002].

Array Reconfiguration

The ability to spin-up an array of EMFF spacecraft creates an interesting opportunity in that the array can be reconfigured without the use of consumables [Miller et al, 2002]. In the simplest scenario, the five spacecraft interferometer will first spin-up to the required spinning rate from rest, and perform the required detection process. It then reverses the process to de-spin. Once stationary, each spacecraft can then reconfigure itself around the baseline of the array without the use of propellant, but through the use of a gimbaled reaction wheel assembly. Once all the spacecraft are aligned, the process can be repeated, again without the use of any propellant. The array can switch between any two rotation disks, provided it is halted on the common line formed by the intersection of the disks. In theory, the array could operate indefinitely. Preliminary results indicate that there exist a number of motions to spin-up an array of EMFF spacecraft. This opens up the opportunity to determine the trajectory that is best suited to spin-up the spacecraft.

The EMFF concept also allows the possibility of increasing or decreasing the overall baseline of the array. The 75 m baseline chosen for the TPF is, in fact, ideal to detect Earth-like planets in extrasolar systems that are located ten parsecs away. However, since the TPF interferometer is required to survey extrasolar systems in the range of five to fifteen parsecs away, it makes sense to change the overall baseline of the interferometer to give the best detection possible. To achieve

this, one possible method is to simply change the baseline of the interferometer while holding the orientation of the dipoles fixed. Another possible maneuver is to change both the size and the rotation rate of the array. This maneuver is obviously more complicated and may involve the use of reaction wheels.

Earth Orbit Concept

EMFF in low Earth orbit is also a possibility. EMFF can be used to counteract secular drift between spacecraft due to J_2 perturbations [Sedwick et al, 1999]. It may also be feasible for re-orienting or resizing arrays instead of using propellant-based thrusters as explored in Chapter 3. Considerations now include operation in the presence of Earth's magnetic field, the strength needed to counteract differential drag and solar pressure, and interference with communication and radar payloads.

Close-Proximity Operations

This EMFF concept may also find application in rendezvous and docking, magnetic trapping of mirror facets into large segmented mirrors, etc. Close-proximity operations such as these are best suited for EMFF since the magnetic fields are stronger, and avoiding plume impingement becomes more difficult at closer separations. One could also envision a space-based version of the Keck Observatory where there is no need for a backbone truss to support the weight of the mirror segments. Only segment edge control is necessary and it is provided electromagnetically. Due to the soft interfaces, damaged facets can be removed and additional facets can be launched and integrated into the array on an as-needed as-afforded basis.

Concept Comparisons

The EMFF concept was compared to a propulsion-based system that is proposed for the TPF interferometer. There are, however, concepts such as using a truss structure or using tethers to offset the centripetal load experience by the spacecraft. Previous studies have indicated that it is more advantageous to use a propulsion-based system when compared with a truss-based system due to the long baselines that are being considered [Stephenson, 1998]. In another study, a structurally connected system that resembles a tether like structure can in fact be more mass efficient [Surka, 1996].

These comparisons were performed based upon the steady operation of the system only, as was done in this study. To fairly compare all the different concepts, one must also consider the spin-up or transient operations of these systems. For the EMFF, initial studies indicate that the spin-up of the system can be performed using only the electromagnets. As for the truss concept, the use of reaction wheels have been proposed. However, spinning up a tether that connects five spacecraft is complicated. Since the tether system was found to be quite favorable in previous studies, future studies should consider the spin-up operation such that a fair comparison between the various concepts can be made.

Material Considerations

The analysis in this thesis uses the physical properties of materials at room temperature. The operation of the TPF interferometer at infrared wavelengths in free space requires the interferometer to operate at temperatures of about 40^oK. At this temperature, significant improvements in material properties, such as the conductivity of the coil, can be achieved. The use of high-temperature superconductors and other magnetizable materials with larger magnetic moment per unit mass for the core should also be explored. The possibility of using passive magnets to augment the electromagnets and increase the magnetic strength per mass of the system should also be considered.

Magnetic Field Considerations

Another consideration is the effect that such fields can have on spacecraft avionics. Shielding using materials such as mu-metal, analogous to a Faraday cage for electric fields, will help. Another option is to place small, oppositely poled dipoles within the avionics bay to locally warp the magnetic field around the avionics.

The 2.45 Tesla magnetic flux density created by the electromagnets is quite large, considering that the Earth's magnetic flux density is only 5 x 10^{-5} Tesla. This large magnetic flux density may change the local environment of the interferometer if cosmic ray particles are trapped in this magnetic flux. Similar to the Earth's Van Allen Belt, a localized construct of this effect may be observed by the interferometer. Since the interferometer's magnetic field can be turned off, one may consider limiting the interferometer to short duration operations to reduce the trappings of these cosmic ray particles. Future studies should investigate this localized effect to minimize its impact on the interferometer's operation.

5.6 Summary

The Electromagnetic Formation Flight concept for a rotating multi-spacecraft interferometer has been introduced. This concept is particularly attractive for missions such as the Terrestrial Planet Finder since it theoretically requires no propellant. The lack of reliance on propellant-based systems also eliminates the plume impingement and contamination issues that are associated with these systems.

In Section 5.2, a mission efficiency metric is introduced to evaluate the best design for a rotating interferometer. This metric favors the selection of interferometers with high rotation rates while requiring little mass. The design exercise for a two spacecraft interferometer is carried out, resulting in the optimal total system mass of $6m_o$, or $6m_o + 4\dfrac{m_o}{\chi}\left[\dfrac{\mu}{m}\right]_{core}\left[\dfrac{\mu}{m}\right]_{coil}^{-1}$ when a third spacecraft is considered.

In Section 5.3, the best design for a five spacecraft interferometer based upon the requirements of the TPF mission is obtained. Even though it is not optimal in terms of mission efficiency, the EMFF design is comparable to the currently proposed propulsion-based system in terms of mass fractions, power demands and volume requirements. The possibility of eliminating both pollution and contamination issues associated with propellant-based systems makes the EMFF concept more desirable.

The controllability for this EMFF concept is explored in Section 5.4. The ability to reject small perturbations is important to ensure that light collected from the collector spacecraft can be adequately interfered. Using the pole representation introduced in Section 5.1, the generation of the **A** and **B** control matrices is derived and automated. These matrices are then used to determine the controllability of the various EMFF control topologies. Full controllability can only be achieved if the Y-pole configuration is used in two-dimensional space, while a four-pole system is required in three-dimensional space.

Future work that warrants further investigation is presented in Section 5.5. A brief discussion is presented on the spin-up a rotating interferometer. The ability to spin-up the interferometer using only the electromagnets opens up the possibility of re-targeting, re-sizing, and changing the rotation rate of the interferometer without reliance on consumables. Furthermore, there seem to be

multiple ways to reconfigure the array and, thus, an opportunity to determine the optimal reconfigurations for these spacecraft.

The prospect of eliminating propellant from a mission such as the TPF makes the EMFF concept extremely attractive. In this chapter, the viability of the EMFF as applied to the TPF mission has been demonstrated. The ground work for the control design has also been laid down for a multi-spacecraft multipole EMFF system. The possibilities of extending the EMFF concept to include close-proximity operations, such as docking and formation control in low Earth orbits, are also discussed. Again, the significant benefits that can be reaped from a system that requires no thrusters make EMFF a technology warranting further exploration.

Chapter 6

CONCLUSIONS AND RECOMMENDATIONS

6.1 Thesis Summary

The main objective of this thesis is to systematically analyze the ability of multi-spacecraft systems to meet both the science and mission requirements with the limited resources allocated to them. To achieve this objective, the following four sub-objectives were recognized:

- Determine the framework to determine the trajectories for multi-spacecraft systems;
- Understand and formulate the science or mission requirements into the chosen framework;
- Demonstrate the proposed methodology on currently proposed missions;
- Determine the viability of the proposed systems to meet the given requirements.

Based upon the tools that have already been developed, the optimal control framework was chosen to determine the trajectories for the various multi-spacecraft systems considered in this thesis. The science requirements of these systems were determined and formulated into the optimal control framework. The framework was then applied to two multi-spacecraft missions, namely the Air Force TechSat 21 Earth orbiting cluster and NASA's Terrestrial Planet Finder, originally designed for planet detection. The viability of these proposed missions, including the proposed Electromagnetic Formation Flight concept, to meet the given requirements were analyzed. The following is a chapter-by-chapter summary of the research performed to achieve these objectives.

Chapter 2

The first objective of the thesis was met by choosing the optimal control framework for the multi-spacecraft trajectory optimization work performed in this thesis. This framework was determined

to be the most appropriate due to the extensive tools that have been developed. One such tool is the Linear Quadratic controller. For a linear dynamic system with quadratic cost function, the optimal LQ controller can simply be written in terms of the state and co-state variables of the system. Throughout this thesis, this controller was used to determine the multi-spacecraft trajectories for the various missions.

The theoretical development using the calculus of variation technique as applied to optimal control problems was first presented. Both the necessary and boundary conditions required to determine the optimal trajectories were determined. Since analytical solutions to the optimal control problem can only be obtained for the simplest cases, numerical techniques must be considered. In this thesis, the multiple shooting technique was considered to be the most appropriate from the stability point of view. This technique, however, can be computationally expensive.

Chapter 3

The first multi-spacecraft mission considered for this research is the Earth orbiting TechSat 21 Space Based Radar mission. The program was initiated by the Air Force Research Laboratory to explore the basic technologies required to enable a Distributed Satellite System, one of which is formation flight. Using the optimal control framework presented in Chapter 2, the optimal trajectories for the multi-spacecraft cluster were determined.

The sparse aperture requirement requires that the spacecraft in the cluster to be maintained in some sort of formation. Using the modified set of linearized Hill equations, closed formation trajectories were found such that spacecraft in a cluster can remain in a closed formation with minimal effort. Since the goal is to obtain trajectories to allow the spacecraft to reach these closed formation trajectories, terminal conditions specific to these Earth orbiting clusters were developed. Together with the quadratic electrical energy cost function, the initializing and resizing trajectories for the TechSat 21 flight experiment cluster of three spacecraft were determined.

Based on the current system design, the TechSat 21 cluster can actually be initialized in as little as half an orbital period. However, it is recommended that the initialization time be increased to at least one orbital period as ΔV savings of more than 67% can be achieved. Also, it was found that most of the effort was spent on changing the spacecraft orbital inclination.

For the currently designed system, resizing the cluster to the 2.5 km elliptical trajectory is only possible if a maneuvering time of at least half an orbital period is prescribed. For shorter maneuvering times, the resizing maneuver can cost at least 30% of the ΔV budgeted for the entire mission. As such, maneuvering times of greater than one orbital period is recommended, but the maneuver still comes at a steep ΔV cost of 10 m/s, which is about 25% of the total.

Chapter 4

In Chapter 4, the optimal control framework is applied to a multi-spacecraft stellar imaging system operating in a 'gravitational-free' environment. Considering both the science and traditional control metrics, the imaging trajectories for a two spacecraft interferometer were determined. The framework was then applied to determine the viability of the current multi-spacecraft TPF design to meet the imposed imaging requirements.

A review of some the proposed imaging metrics indicates that a well distributed u-v coverage system is more preferable to one with redundant coverage, especially when characteristics of the targets are not well known. Even though redundant u-v coverage can improve the signal-to-noise ratio of the measurements, information obtained from additional u-v points can contribute to better image quality. Based upon this observation, an imaging metric that penalizes both redundant and extremely short baseline coverages while encourages long baseline coverages was developed. Introducing this metric into the optimal control framework, intermediate boundary conditions were found to exist at the predefined imaging times. Discrete jumps in the co-state trajectories were found while state trajectories remained smooth as was shown in the two spacecraft example.

The framework is then applied to NASA's TPF mission. Originally designed to detect the existence of Earth-like planet around extra-solar systems, a general astrophysical imaging requirement has been levied onto the mission to make it more attractive. The optimal trajectories based upon a four collector spacecraft arranged in a Cornwell imaging configuration were determined. The results indicate the currently designed system can meet the imaging requirements of the proposed scientific plan. Assuming that 26% of the resources are allocated to the astrophysical imaging process, up to 1000 images can be obtained with the currently designed system.

Chapter 5

In this chapter, a formation flight concept that based upon the use of electromagnetic forces between spacecraft to control formation geometry is explored. This concept is particularly attractive for TPF since it theoretically requires no propellant, thus eliminating both plume impingement and contamination issues associated with propellant based systems.

To determine the best system for a rotating interferometer, a mission efficiency metric that favors selection of systems with high rotation rates while requiring little mass was proposed. When applied to the five spacecraft TPF interferometer, the mission efficiency design was found to be quite massive compared to the proposed system while rotating at a speed that is most likely to be too fast for the interferometer to collect enough photons to detect the Earth-like planet. However, in order to fairly compare the EMFF concept with the proposed system, the minimum mass design was determined based upon a fixed rotation rate of one rotation in every eight hours. This EMFF design is in fact comparable to the currently proposed propulsion based system in terms of mass fractions, power demands and volume requirements. The possibility of eliminating both pollution and contamination issues associated with propellant based systems makes the EMFF that much more desirable.

To further demonstrate the viability of the EMFF concept, the controllability of the system was also investigated. The ability to reject small perturbations is important to ensure that light collected from the collector spacecraft can be adequately interfered. Using the pole representation introduced in the chapter, the generation of the **A** and **B** control matrices was derived and automated. From these matrices, it was determined that full controllability of the system can only be achieved if the Y-pole configuration is used in the two dimensional space, while a minimum of four pole per spacecraft is required in the three dimensional space.

The prospect of eliminating propellant from a mission such as the TPF makes the EMFF concept extremely attractive. Even though the optimal control framework was not applied to this EMFF concept in this thesis, the possibility of using this framework to determine the optimal trajectories to spin-up, re-target or resize the array exists. Furthermore, the system analysis performed in this thesis was adequate to prove the viability of the EMFF concept.

6.2 Contributions

The key contribution made in this thesis is the ability to obtain multi-spacecraft trajectories that are optimized based upon both the control and science requirements. Much work has been done in optimal control theory where optimal trajectories are obtained based upon either a minimum fuel or minimum energy metric. Though these initial optimal control works are important, often times the results are obtained decoupled from the science requirements. These science requirements are usually very different from the control metrics and need to be seriously considered. This is especially true for multi-spacecraft missions. In this thesis, the science requirements for the various multi-spacecraft missions are first considered. These requirements are then translated into the optimal control framework where control tools that have already been developed can be exploited. Throughout the thesis, optimal trajectories based upon these combined metrics are obtained to enable the various trade analysis performed in this study. Specific contributions in this thesis are listed below, grouped in terms of the key chapters.

Key Contributions from Chapter 3

The following are the specific contributions of this thesis for the Air Force TechSat 21 mission:

- Developed terminal conditions that correspond to the sparse aperture radar requirements in the optimal control framework;
- Developed trade analysis tools to evaluate the capability of a multi-aperture Earth orbiting constellation for both initialization and resizing problems.

Key Contributions from Chapter 4

In Chapter 4, two distributed spacecraft imaging missions are considered. The specific contributions from this study are:

- Framed imaging metric in the optimal control framework based upon the interferometric science requirement;
- Demonstrated the viability of the TPF multi-spacecraft interferometer designed originally for planet detection to meet the newly imposed imaging requirements.

Key Contributions from Chapter 5

In Chapter 5, the Electromagnetic Formation Flight (EMFF) concept is proposed for a separated spacecraft interferometer. The following are the key contributions from the study:

- Proposed and demonstrated the viability of EMFF concept for a rotational separated spacecraft interferometer, specifically the Terrestrial Planet Finder interferometer;

- Automated the generation of **A** and **B** control matrices for a multi-spacecraft multi-pole Electromagnetic Formation Flight interferometer as ground work for future control analysis;

- Analyzed the controllability issues of various EMFF control topologies in both two and three dimensional frames.

6.3 Recommendations For Future Work

The analysis performed here allowed all the objectives of the thesis to be successfully met. As with any on going research, there is always room to improve upon the fidelity of the analysis, thus giving better confidence in the obtained results. Listed here is a recommendation of the future work that warrant considerations.

Plume Impingement. Plume impingement is a serious concern for close proximity operation of multi-spacecraft systems. Be it for Earth orbiting clusters or operation in a gravitational-free environment, direct plume impingement can seriously affect dynamic stability of neighboring spacecraft. In some cases, the high speed particle ejection can ablate material off the spacecraft causing permanent damage. As such, future work in multi-spacecraft trajectory optimization must ensure that only minimal thruster firings are allowed when either the spacecraft are close together or the thrusters are aimed at the other spacecraft.

Plume Contamination. Even if precautions are taken against direct impingement, propulsion plume left floating around can also affect the mission. As an example, the propellant plume can put a thermally bright haze across the line-of-sight of the telescope for the TPF interferometer operating in the infrared regime. There is also the possibility that particulate depositing on sensitive sensors thus affecting the performance of the sensors. Both experimental and theoretical work are needed to model these propellant plumes accurately such that 'keep-out' zones can be defined in the trajectory optimization problem.

Resource Allocation. A concern with multi-spacecraft array maintenance is the unequal resource usage by the spacecraft in the cluster. The trajectory optimization performed in this thesis minimizes the overall system metric. It however, does not consider where the resources are obtained from. To ensure the required resources are equally distributed among the spacecraft in the cluster,

it may be necessary to add a metric that minimizes the variation in the resource usage among the spacecraft. Again, similar to additional constraints, this additional metric may require more overall resources but will result in more uniformity in resource usage.

Imaging Plan. One of the drawbacks in the distributed spacecraft imaging work performed in this research is the lack of knowledge as to types of targets that the TPF interferometer is supposed to image. As such, the imaging metric considered is based upon a general consensus that an image that results from a well distributed u-v coverage should provide good image quality. This, however, is not exactly accurate a image quality is dependent upon the type of targets that are being imaged. To maximize the science returns, science requirements that correspond to these targets must be obtained. With this information, imaging trajectories tailored to the types of targets can be obtained, thus giving a better estimate of the resources required.

Reconfiguration Trajectories for EMFF. In order to achieve the various science goals of the mission, the TPF is required to either change rotation rate or the overall baseline of the interferometer. Slower rotation rates are required when medium or high spectroscopy analysis of the detected planet is performed. As for changing the overall baseline, the TPF is required to survey planets in the range of 5 to 15 parsecs away from our solar system. As such, to ensure that light from the parent star is adequately nulled out, the resolution of the interferometer must be changed, thus the overall baseline. Since there are a number of ways to reconfigure these spacecraft, there exists the possibility to optimize these reconfiguration maneuvers. The framework used in this thesis can be applied to the EMFF interferometer.

Applications for EMFF. With the possibility of eliminating both plume and contamination issues associated with propellant based systems, the EMFF concept must be seriously considered for close proximity operations where plume avoidance can be quite difficult. The EMFF concept is best suited for rendezvous and docking operations since stronger magnetic fields can be obtained. One could also envision a space-based version of the Keck Observatory where there is no need for a backbone truss to support the weight of the mirror segments. Only segment edge control is necessary and it is provided electromagnetically. Due to the soft interfaces, damaged facets can be removed and additional facets can be launched and integrated into the array on an as-needed as-afforded basis.

EMFF in Earth's Potential Field. Another possibility that warrants serious consideration is the application of the EMFF concept to Earth orbiting clusters. To hold the cluster formation, the Earth gravitational field is exploited since effort free trajectories can be found (Chapter 3). The EMFF concept can then be exploited when the cluster needs to be reconfigured. In this case, the gravitational field acts as a constraint while the EM field is the transport mechanism. This EM control can also be used to reject small disturbances even when the spacecraft are on the free elliptical trajectory. The optimal control formulation presented in this study should be adapted to determine the optimal reconfiguration for this multi-spacecraft system operating in multiple potential fields.

6.4 Concluding Remarks

The main objective of this thesis, which is to systematically analyze the ability of multi-spacecraft systems to meet both the science and mission requirements, has been achieved. Using the optimal control framework, optimal spacecraft trajectories for both Earth orbiting and gravitational free clusters were determined by considering both the science and traditional control metrics. Based upon these results, the capability of these currently designed systems to satisfy both their science and mission requirements were analyzed. Also proposed in the thesis is a multi-spacecraft system operating in a self-induced potential field for rotating interferometers. Using only renewable source of energy, electric power, the relative positions and orientations between spacecraft are controlled by the electromagnets. The viability of the Electromagnetic Formation Flight concept as applied to the Terrestrial Planet Finder mission was investigated and found to be comparable to the currently proposed system. The possibility of eliminating plume impingement and contamination issues associated propellant based systems warrant serious consideration for the EMFF concept.

REFERENCES

[Beichman et al, 1999] Beichman, C. A., Woolf, N. J., and Lindensmith, C. A., eds., *The Terrestrial Planet Finder (TPF): A NASA Origins Program to Search for Habitable Planets*, JPL Publication 99-3, May 1999.

[Betts, 1998] Betts, J. T., *Survey of Numerical Methods for Trajectory Optimization*, Journal of Guidance, Control, and Dynamics, Vol. 21 No. 2, March - April 1998.

[Bracewell et al, 1979] Bracewell, R., and MacPhie, *Searching for Nonsolar Planets*, ICARUS Vol. 38, pp 136-147, 1979.

[Burton et al, 1998] Burton, R. L., and Turchi, P. J., *Pulsed Plasma Thruster*, Journal of Propulsion and Power, Vol. 14, No. 5, 1998.

[Cornwell, 1988] Cornwell, T. J., *A Novel Principle for Optimization of the Instantaneous Fourier Plane Coverage of Correlation Arrays*, IEEE Transactions on Antennas and Propagation, Vol. 36, No. 8, August 1988.

[Decou, 1991] Decou, A. B., *Multiple Spacecraft Optical Interferometry: Prelimnary Feasibility Assessment*, Internal Report D-8811 Jet Propulsion Laboratory, Pasadena, California, August 1991.

[Golay, 1971] Golay, M., *Point Arrays Having Compact Non-Redundant Autocorrelations*, Journal of Optical Society America, Vol 61, pg 272, 1971.

[Hill, 1878] Hill, G. W., *Researches in the Lunar Theory*, American Journal of Mathematics, Vol. 1, No. 1, pp. 5-26, 1878.

[Hruby et al, 1999] Hruby, V., Monheiser, J., Pote, B., Freeman, C., and Connolly, W., *Lower Power, Hall Thruster Propulsion System*, IEPC-99-092, 1999.

[Hughes, 1986] Hughes, P. C., *Spacecraft Attitude Dynamics*, John Wiley and Sons, 1986.

[Inalhan et al, 2001] Inalhan, G., Tillerson, M., and How, J. P., *Relative Dynamics and Control Spacecraft Formations in Eccentric Orbits*, Accepted for publication, Journal of Guidance, Dynamics, and Controls, Sept. 2001.

[Kirk, 1970] Kirk, D. E., *Optimal Control Theory - An Introduction*, Prentice Hall Inc., 1970.

[Kong, 1998a] Kong, E.M., and Miller, D.W., *Optimization of Separated Spacecraft Interferometer Trajectories in the Absence of A Gravity-Well*, SPIE's International Symposium on Astronomical Telescopes and Instrumentation, Paper no. 3350-13, March 1998.

[Kong, 1998b] Kong, E. M., *Optimal Trajectories and Orbit Design for Separated Spacecraft*

Interferometry, Masters Thesis, Department of Aeronautics and Astronautics, Massachusetts Institute of Technology, 1998.

[Kong et al, 1999a] Kong, E. M. C., Miller, D. W., and Sedwick, R. J., *Exploiting Orbital Dynamics for Aperture Synthesis Using Distributed Satellite Systems: Applications to a Visible Earth Imager System*, Journal of the Astronautical Sciences, Vol. 47, Nos. 1 and 2, Jan - June 1999.

[Kong et al, 1999b] Kong, E.M.C., Miller, D.W. and Sedwick, R.J., *Exploiting Orbital Dynamics for Stellar Separated Spacecraft Interferometry*, American Control Conference, ACC99-I014-04, June 1999.

[Kong et al, 2000] Kong, E. M. C., and Miller, D. W., *Optimal Spacecraft Re-Orientation for Earth Orbiting Clusters: Applications to TechSat 21*, 51st International Astronautical Congress, IAF Paper No. IAF-00-A.4.06, 2-6 October 2000.

[Larson et al, 1998] Larson, W., and Wertz, J., *Space Mission Analysis an Design*, Microcosm, Inc., and Kluwer Academic Publishers, 2nd edition, 1998.

[Lawden, 1963] Lawden, D. F., *Optimal Trajectories for Space Navigation*, Butterworths, London, 1963.

[Linfield, 1997] Linfield, R., *Number of Sources DS3 Can Observe, as a Function of Spacecraft Power*, Jet Propulsion Laboratory Inter-office Memorandum 335.1-97-0.14, 16th May 1997.

[Magneticasoft, 2001] Magneticasoft, *Soft Ferromagnetic Materials (Soft Steel Like): Mathematical modeling of the Magnetization Curve*, http://www.magneticasoft.com/materials/ magnet1.html, accessed 28th December 2001.

[Martin et al, 1999] Martin, M., and Stallard, M. J., *Distributed Satellite Missions and Technologies - The TechSat 21 Program*, AIAA Paper No. 99-4479, 1999.

[Mathworks, 2001] The Mathworks Inc., *Optimization Toolbox For Use with Matlab® - User's Guide*, Version 2, 2001.

[Miller et al, 2002] Miller, D.W., Sedwick, R.J., and Kong, E.M.C., *Electromagnetic Formation Flight for Sparse Aperture Telescopes*, to be presented at the IEEE Aerospace Conference, March 2002

[Powers et al, 1997] Powers, M., Leitner, J., Hackney, E., Bell, K. D., Boucher, R., Roberston, L., Schrader, K., *Assessment of a large aperture telescope trade space and active optomechanical control architecture*, IEEE Aerospace Applications Conference Proceedings, Proceedings of the 1997 IEEE Aerospace Conference, p 197-229, Feb 1-2, 1997.

[Reichbach, 2000] Reichbach, J., *Micropropulsion System Selection for Precision Formation Flying Satellites*, Masters Thesis, Department of Aeronautics and Astronautics, Massachusetts Institute of Technology, 2001.

[Richards et al, 2001] Richards, A., How, J., Schouwenaars, T., and Feron, E., *Plume Avoidance Maneuver Planning Uisng Mixed Integer Linear Programming*, AIAA Guidance, Navigation, and Control Conference and Exhibit, Montreal, Canada, AIAA-2001-4091, August 2001.

[Schaub et al, 1999] Schaub, H., Alfriend, K., J_2 *Invariant Relative Orbits for Spacecraft Formations*, NASA GSFC Flight Mechanics and Estimation Conference, May 1999.

[Schweighart, 2001] Schweighart, S., *Development and Analysis of a High Fidelity Linearized J_2 Model for Satellite Formation Flying*, Masters Thesis, Department of Aeronautics and Astronautics, Massachusetts Institute of Technology, 2001.

[Sedwick et al, 1998] Sedwick, R. J., Kong, E. M. C., and Miller, D. W., *Exploiting Orbital Dynamics and Micropropulsion for Aperture Synthesis Using Distributed Satellite Systems: Applications to TechSat 21*, AIAA Paper No. 98-5289, 1998.

[Sedwick et al, 1999] Sedwick, R. J., Miller, D. W., and Kong, E. M. C., *Mitigation of Differential Perturbations in Clusters of Formation Flying Satellites*, Journal of the Astronautical Sciences, Vol. 47, Nos. 3 and 4, July - December 1999.

[Stachnik et al, 1984] Stachnik, R. V., Melroy, P., McCormack, E. F., Arnold, D., and Gezari, D. Y., *Multiplle Spacecraft Michelson Stellar Interferometry*, Proceedings of the Society of Photo-Optical Instrumentation Engineers, Instrumentation in Astronomy V, Vol. 445, 1984.

[Stephenson, 1998] Stephenson, R. L., Jr., *Comparative System Trades Between Structurally Connected and Separated Spacecraft Interferometers for the Terrestrial Planet Finder Mission*, Masters Thesis, Department of Aeronautics and Astronautics, Massachusetts Institute of Technology, 1998.

[Strang, 1993] Strang, G., *Introduction to Linear Algebra*, Wellesley-Cambridge Presses, 1993.

[Stoer et al, 1976] Stoer, J., and Bulirsch, R., *Introduction to Numerical Analysis*, Springer-Verlag, 1976.

[Surka, 1996] Surka, D. M., *A Comparison of Structurally Connected and Multiple Spacecraft Inteferometers*, Masters Thesis, Department of Aeronautics and Astronautics, Massachusetts Institute of Technology, 1996.

[Sutton, 1992] Sutton, G. P., *Rocket Propulsion Elements - an Introduction to the Engineering of Rockets*, John Wiley & Sons, Inc., 1992.

[Thompson et al, 1986] Thompson, A. R., Moran, J. M., Swenson, G. W. Jr., *Interferometry and Synthesis in Radio Astronomy*, 1986.

[Tillerson et al, 2001] Tillerson, M., and How, J. P., *Formation Flying Control in Eccentric Orbits*, AIAA Guidance, Navigation, and Control Conference and Exhibit, Montreal, Canada, AIAA-2001-4092, August 2001.

[Wang et al, 1996] Wang, P. K. C., and Hadaegh, F. Y., *Coordination and Control of Multiple Microspacecraft Moving in Formation*, Journal of the Astronautical Science, Vol. 44 No. 3, July - September 1996.

[Wang et al, 1999] Wang, P. K. C., Hadaegh, F. Y., and Lau, K., *Synchronized Formation Rotation and Attitude Control of Multiple Free-Flying Spacecraft*, Journal of Guidance, Control, and Dynamics, Vol. 22, No. 1, January - February 1999.

Appendix A

AUTOMATED CODE GENERATION FOR CONTROL MATRICES

The generation of the **A** and **B** control matrices for the EMFF concept presented in this thesis can be automated. In this appendix, the derivation of the components for the **A** and **B** matrices is presented. The associated Matlab code that provides these **A** and **B** matrices is also provided.

A.1 A and B Matrices Derivation

The organization of the state vector for this EMFF concept is given by Equation 5.63:

$$\vec{x} = \left[\overrightarrow{\Delta x_{1,2}} \; \ldots \; \overrightarrow{\Delta x_{1,M}} \; \vec{\varepsilon}_1 \; \ldots \; \vec{\varepsilon}_M \; \overrightarrow{\Delta \dot{x}_{1,2}} \; \ldots \; \overrightarrow{\Delta \dot{x}_{1,M}} \; \vec{\omega}_1 \; \ldots \; \vec{\omega}_M \right]^T \qquad (A.1)$$

where the positional variables are first listed, followed by the quaternion variables, and both of their rates. Using this organization, the **A** matrix is therefore made up of the following components:

$$
A = \begin{array}{cccc}
\left[\begin{array}{cccc}
0 & 0 & I & 0 \\
0 & A_{b,b} & 0 & A_{b,d} \\
A_{c,a} & A_{c,b} & 0 & 0 \\
A_{d,a} & A_{d,b} & 0 & A_{d,d}
\end{array}\right]
\end{array}
$$

Row indices (right): $1 \ldots 3M-3$ for $\overrightarrow{\Delta x}$; $3M-2 \ldots 7M-3$ for $\vec{\varepsilon}$; $7M-2 \ldots 10M-6$ for $\overrightarrow{\Delta \ddot{x}}$; $10M-5 \ldots 13M-6$ for $\vec{\omega}$.

Column indices (bottom): $1 \ldots 3M-3$ for $\overrightarrow{\Delta x}$; $3M-2 \ldots 7M-3$ for $\vec{\varepsilon}$; $7M-2 \ldots 10M-6$ for $\overrightarrow{\Delta \dot{x}}$; $10M-5 \ldots 13M-6$ for $\vec{\omega}$.

$$(A.2)$$

where the corresponding indices represent the entries in the **A** matrix, shown together with the corresponding state variables in vectorial form. The corresponding **B** matrix using the control notation given in Equation 5.64 is:

$$
B = \left[\begin{array}{c}
0 \\
0 \\
B_c \\
B_d
\end{array}\right]
$$

Row indices (right): $1 \ldots 3M-3$ for $\overrightarrow{\Delta \dot{x}}$; $3M-2 \ldots 7M-3$ for $\vec{\varepsilon}$; $7M-2 \ldots 10M-6$ for $\overrightarrow{\Delta \ddot{x}}$; $10M-5 \ldots 13M-6$ for $\vec{\omega}$.

Column indices (bottom): $1 \ldots N-1$ for $\vec{u}_1$; $N \ldots 2(N-1)$ for $\vec{u}_2$; $\ldots$; $2N-1 \ldots (M-1)(N-1)$, $(M-1)(N-1)+1 \ldots M(N-1)$ for $\vec{u}_M$.

$$(A.3)$$

The rest of this section is devoted to deriving the subscripted entries in the **A** and **B** matrices. We will begin with the first row in the **A** matrix and conclude with the last row in the **B** matrix.

A.1.1 Identity Entry (A Matrix)

The identity entry in the **A** matrix results from simply relating the time derivative variables on the left-hand side of the dynamics equation to the differential velocities defined in the state vector. As such, all the entries except for those corresponding to the velocity variables are equated to zero.

A.1.2 Quaternion Rates Entry (A Matrix)

The second set of rows in the **A** matrix is governed by the quaternion rate equations given by Equation 5.61. Expanding this equation in terms of the quaternion and angular rate variables, the quaternion rates for the m-th spacecraft can be expressed as:

$$\vec{\dot{\varepsilon}}_m = \frac{1}{2} \begin{bmatrix} -\varepsilon_3\omega_{2,B} + \varepsilon_2\omega_{3,B} + \varepsilon_4\omega_{1,B} \\ \varepsilon_3\omega_{1,B} - \varepsilon_1\omega_{3,B} + \varepsilon_4\omega_{2,B} \\ -\varepsilon_2\omega_{1,B} + \varepsilon_1\omega_{2,B} + \varepsilon_4\omega_{3,B} \\ -\varepsilon_1\omega_{1,B} - \varepsilon_2\omega_{2,B} - \varepsilon_3\omega_{3,B} \end{bmatrix}_m \qquad (A.4)$$

The $A_{b,b}$ entry in the **A** matrix is then obtained by taking the partial derivative of the quaternion rates with respect to the quaternion variables:

$$A_{\begin{bmatrix} 3M+4m-6\ :\ 3M+4m-3 \\ 3M+4m-6\ :\ 3M+4m-3 \end{bmatrix}} = \frac{\partial \vec{\dot{\varepsilon}}_m}{\partial \vec{\varepsilon}_m}$$

$$= \frac{1}{2} \begin{bmatrix} 0 & \omega_3 & -\omega_2 & \omega_1 \\ -\omega_3 & 0 & \omega_1 & \omega_2 \\ \omega_2 & -\omega_1 & 0 & \omega_3 \\ -\omega_1 & -\omega_2 & -\omega_3 & 0 \end{bmatrix}_{m,B} \qquad (A.5)$$

where the first row of the subscripted index corresponds to the row indices and the second corresponds to the column indices. Clearly, the $A_{b,b}$ entry is comprised of M number of 4 x 4 block diagonal matrices, with each corresponding to a spacecraft in the system. Similarly, the $A_{b,d}$ entry is obtained by taking the partial derivative with respect to the angular rates of the spacecraft:

$$
A_{\begin{bmatrix} 3M+4m-6 & : & 3M+4m-3 \\ 10M+3m-8 & : & 10M+3m-6 \end{bmatrix}} = \frac{\partial}{\partial \overrightarrow{\omega}_{m,B}} \overrightarrow{\dot{\varepsilon}}_m
$$

$$
= \frac{1}{2} \begin{bmatrix} \varepsilon_4 & -\varepsilon_3 & \varepsilon_2 \\ \varepsilon_3 & \varepsilon_4 & -\varepsilon_1 \\ -\varepsilon_2 & \varepsilon_1 & \varepsilon_4 \\ -\varepsilon_1 & -\varepsilon_2 & -\varepsilon_3 \end{bmatrix}_m
$$
(A.6)

where M number of 4 x 3 block diagonal matrices make up this entry.

A.1.3 Differential Acceleration Entry (A Matrix)

The next two entries in the **A** matrix come directly from the differential acceleration relationship between the spacecraft:

$$
\overrightarrow{\Delta \ddot{x}}_{1,m} = \frac{\overrightarrow{F}_m}{m_{sc_m}} - \frac{\overrightarrow{F}_1}{m_{sc_1}}
$$
(A.7)

The first entry ($A_{c,a}$) is simply the partial derivative with respect to the positional variables while the second ($A_{c,b}$) is with respect to the quaternion variables. Lets consider the partial with respect to the positional variables first.

The general indexing for the A matrix when the partial derivative taken with respect to the d-th positional state is given by:

$$
A_{\begin{bmatrix} 7M+3m-8 & : & 7M+3m-6 \\ 3d-5 & : & 3d-3 \end{bmatrix}} = \frac{\partial}{\partial \overrightarrow{\Delta x}_{1,d}} \overrightarrow{\Delta \ddot{x}}_{1,m}
$$
(A.8)

where both m and d are incremented from 2 to M respectively. This block of A matrix consists of a fully populated ($3M$ - 3) square matrix. The partial derivative of Equation A.8 is simply the summation of the partial derivatives of $\overrightarrow{F}_m$ and $\overrightarrow{F}_1$. From Equations 5.4 and 5.66, the force acting on the m-th spacecraft can be re-written as:

$$
\overrightarrow{F}_m = \sum_{\substack{n=1 \\ a \neq m}}^{N} \sum_{a=1}^{M} \sum_{b=1}^{N} \frac{k q_{mn} q_{ab}}{|\overrightarrow{r}_{ab,mn}|^3} \overrightarrow{r}_{ab,mn}
$$
(A.9)

The partial derivative of the force acting on the *m*-th spacecraft with respect to the position variables between the first spacecraft and the *d*-th spacecraft can be separated into effectively divided into two components: (1) when $m \neq d$ and (2) when $m = d$. For the first case, the partial derivative of Equation A.9 with respect to the $\overrightarrow{\Delta x_{1,d}}$ vector can be expanded to be:

$$
\frac{\partial}{\partial \overrightarrow{\Delta x_{1,d}}} \overrightarrow{F}_m = k \sum_{n=1}^{N} \sum_{b=1}^{N} q_{mn} q_{db} \left[\frac{1}{\left| \overrightarrow{r_{db,mn}} \right|^3} \frac{\partial}{\partial \overrightarrow{\Delta x_{1,d}}} (\overrightarrow{r_{db,mn}}) \right.
$$
$$
\left. + \overrightarrow{r_{db,mn}} \frac{\partial}{\partial \overrightarrow{\Delta x_{1,d}}} \left(\frac{1}{\left| \overrightarrow{r_{db,mn}} \right|^3} \right) \right]
$$

(A.10)

where the dependencies on $\overrightarrow{\Delta x_{1,d}}$ are observed only for the $\overrightarrow{r_{db,mn}}$ vector. The first partial derivative is simply the partial derivative of Equation 5.67 which results in the negative of a 3 x 3 identity matrix:

$$
\frac{\partial}{\partial \overrightarrow{\Delta x_{1,d}}} \overrightarrow{r_{db,mn}} = -I
$$

(A.11)

The second partial derivative in the equation is slightly more complicated. Using a series of chain rules, we find the resulting partial derivative is a function of the transpose of the $\overrightarrow{r_{db,mn}}$ vector and its magnitude. The step-by- step derivation of this partial derivative is given by:

$$
\frac{\partial}{\partial \overrightarrow{\Delta x_{1,d}}} \left(\frac{1}{\left| \overrightarrow{r_{db,mn}} \right|^3} \right) = \frac{-3}{\left| \overrightarrow{r_{db,mn}} \right|^4} \frac{\partial}{\partial \overrightarrow{\Delta x_{1,d}}} \left| \overrightarrow{r_{db,mn}} \right|
$$
$$
= \frac{-3}{\left| \overrightarrow{r_{db,mn}} \right|^4} \frac{\partial}{\partial \overrightarrow{\Delta x_{1,d}}} [\overrightarrow{r_{db,mn}}^T \cdot \overrightarrow{r_{db,mn}}]^{(1/2)}
$$
$$
= \frac{-3}{\left| \overrightarrow{r_{db,mn}} \right|^5} \frac{\partial}{\partial \overrightarrow{\Delta x_{1,d}}} [\overrightarrow{r_{db,mn}}^T \cdot \overrightarrow{r_{db,mn}}]
$$
$$
= \frac{3}{\left| \overrightarrow{r_{db,mn}} \right|^5} \overrightarrow{r_{db,mn}}^T
$$

(A.12)

Combining both the above equations, the partial derivative of the force acting on the *m*-th spacecraft taken with respect to $\overrightarrow{\Delta x_{1,d}}$ is:

$$\frac{\partial}{\partial \overrightarrow{\Delta x}_{1,d}} \overrightarrow{F}_m = k \sum_{n=1}^{N} \sum_{b=1}^{N} \frac{q_{mn} q_{db}}{\left| \overrightarrow{r}_{db,mn} \right|^3} \left[-I + 3 \frac{\overrightarrow{r}_{db,mn} \cdot \overrightarrow{r}_{db,mn}^{T}}{\left| \overrightarrow{r}_{db,mn} \right|^2} \right] \qquad \begin{array}{c} \text{for } d = 2 \text{ to } M \\ d \neq m \end{array} \qquad (A.13)$$

A similar derivation for the $m = d$ case results in the following:

$$\frac{\partial}{\partial \overrightarrow{\Delta x}_{1,d}} \overrightarrow{F}_d = k \sum_{n=1}^{N} \sum_{\substack{a=1 \\ a \neq d}}^{M} \sum_{b=1}^{N} \frac{q_{dn} q_{ab}}{\left| \overrightarrow{r}_{ab,dn} \right|^3} \left[I - 3 \frac{\overrightarrow{r}_{ab,dn} \cdot \overrightarrow{r}_{ab,dn}^{T}}{\left| \overrightarrow{r}_{ab,dn} \right|^2} \right] \qquad \begin{array}{c} \text{for } d = 2 \text{ to } M \\ d = m \end{array} \qquad (A.14)$$

which essentially fills up the diagonal block entries in the $A_{c,a}$ matrix. Each of these matrices is a 3 x 3 square matrix.

The partial derivative of $\overrightarrow{F}_1$ with respect to $\overrightarrow{\Delta x}_{1,d}$ can be obtained by substituting $m = 1$ in Equation A.13:

$$\frac{\partial}{\partial \overrightarrow{\Delta x}_{1,d}} \overrightarrow{F}_1 = k \sum_{n=1}^{N} \sum_{b=1}^{N} \frac{q_{1n} q_{db}}{\left| \overrightarrow{r}_{db,mn} \right|^3} \left[-I + 3 \frac{\overrightarrow{r}_{db,1n} \cdot \overrightarrow{r}_{db,1n}^{T}}{\left| \overrightarrow{r}_{db,1n} \right|^2} \right] \qquad \text{for } d = 2 \text{ to } M \qquad (A.15)$$

and together with Equations A.13 and A.14, this equation makes up the components of the $A_{c,a}$ matrix.

The components of the $A_{c,b}$ entry are again derived using the above process. In this case, the partial derivative is now with respect to quaternion variables of the d-th spacecraft. The corresponding indices that make up the $A_{c,b}$ entry are given by:

$$A_{\begin{bmatrix} 7M+3m-8 \, : \, 7M+3m-6 \\ 3M+4d-6 \, : \, 3M+4d-3 \end{bmatrix}} = \frac{\partial}{\partial \overrightarrow{\varepsilon}_d} \overrightarrow{\ddot{\Delta x}}_{1,m} \qquad (A.16)$$

so that $A_{c,b}$ is a fully populated $(3M - 3)$ x $4M$ matrix. Note that the index d now ranges from $d = 1$ to $d = 4$ since each spacecraft has its own set of quaternion variables to describe its attitude.

To determine the partial derivative in Equation A.16, the partial derivative of the Q_m and Q_a matrices in Equation 5.67 must first be determined:

$$
\frac{\partial}{\partial \varepsilon_{1,d}} Q_d = 2 \begin{bmatrix} \varepsilon_1 & \varepsilon_2 & \varepsilon_3 \\ \varepsilon_2 & -\varepsilon_1 & -\varepsilon_4 \\ \varepsilon_3 & \varepsilon_4 & -\varepsilon_1 \end{bmatrix}_d
\qquad
\frac{\partial}{\partial \varepsilon_{2,d}} Q_d = 2 \begin{bmatrix} -\varepsilon_2 & \varepsilon_1 & \varepsilon_4 \\ \varepsilon_1 & \varepsilon_2 & \varepsilon_3 \\ -\varepsilon_4 & \varepsilon_3 & -\varepsilon_2 \end{bmatrix}_d
$$

$$
\frac{\partial}{\partial \varepsilon_{3,d}} Q_d = 2 \begin{bmatrix} -\varepsilon_3 & -\varepsilon_4 & \varepsilon_1 \\ \varepsilon_4 & -\varepsilon_3 & \varepsilon_2 \\ \varepsilon_1 & \varepsilon_2 & \varepsilon_3 \end{bmatrix}_d
\qquad
\frac{\partial}{\partial \varepsilon_{4,d}} Q_d = 2 \begin{bmatrix} \varepsilon_4 & -\varepsilon_3 & \varepsilon_2 \\ \varepsilon_3 & \varepsilon_4 & -\varepsilon_1 \\ -\varepsilon_2 & \varepsilon_1 & \varepsilon_4 \end{bmatrix}_d
$$

(A.17)

where these partial derivatives are given in terms of the individual quaternion variables instead of the general vectorial form. Similar to the process used to determine the partial derivative with respect to the positional state variables, the partial derivative with respect to the quaternion variables can be shown to be:

$$
\frac{\partial}{\partial \varepsilon_{f,d}} \vec{F}_m = k \sum_{n=1}^{N} \sum_{b=1}^{N} \frac{q_{mn} q_{db}}{\left|\overrightarrow{r_{db,mn}}\right|^3} \left[-I + 3 \frac{\overrightarrow{r_{db,mn}} \cdot \overrightarrow{r_{db,mn}}^T}{\left|\overrightarrow{r_{db,mn}}\right|^2} \right] \cdot \frac{\partial}{\partial \varepsilon_{f,d}} Q_d \cdot \overrightarrow{r_{dN,db}}
$$

$$
\begin{aligned}
&\text{for } d = 1 \text{ to } M \\
&\quad\quad d \neq m \\
&\text{for } f = 1 \text{ to } 4
\end{aligned}
$$

(A.18)

and

$$
\frac{\partial}{\partial \varepsilon_{f,d}} \vec{F}_d = k \sum_{n=1}^{N} \sum_{\substack{a=1 \\ a \neq d}}^{M} \sum_{b=1}^{N} \frac{q_{dn} q_{ab}}{\left|\overrightarrow{r_{ab,dn}}\right|^3} \left[I - 3 \frac{\overrightarrow{r_{ab,dn}} \cdot \overrightarrow{r_{ab,dn}}^T}{\left|\overrightarrow{r_{ab,dn}}\right|^2} \right] \cdot \frac{\partial}{\partial \varepsilon_{f,d}} Q_d \cdot \overrightarrow{r_{dN,dn}}
$$

$$
\begin{aligned}
&\text{for } d = 1 \text{ to } M \\
&\quad\quad d = m \\
&\text{for } f = 1 \text{ to } 4
\end{aligned}
$$

(A.19)

where $\varepsilon_{f,d}$ corresponds to the f-th quaternion of the d-th spacecraft.

As for the force experienced by the first spacecraft, $\vec{F}_1$, the partial derivative of this term can again be determined from Equation A.18 when $d \neq m$ and from Equation A.19 when $d = m$.

A.1.4 Angular Acceleration Entry (A Matrix)

The angular acceleration of the m-th spacecraft is given by Equation 5.55:

$$\overrightarrow{\dot{\omega}_{m,B}} = I_{p,m}^{-1}\left[\sum_{n=1}^{N}\sum_{a=1}^{M}\sum_{b=1}^{N}(\overrightarrow{r_{mn}}\times Q_m^T\overrightarrow{F_{ab,mn}}) - \overrightarrow{\omega_m}\times I_{p,m}\overrightarrow{\omega_m}\right]_B \quad\quad (A.20)$$

$$a \neq m$$

which is written in terms of the *m*-th spacecraft body coordinates. The $\overrightarrow{r_{mn}}$ notation in the equation refers to positional vector of the *n*-th pole in the *m*-th spacecraft in terms of the spacecraft's body coordinate system, which is centered about the *N*-th node.

The $A_{d,a}$ entry in the A matrix is again obtained by taking the partial derivative of Equation A.20 with respect to the position state variables. The indices in the A matrix that correspond to this entry are given by:

$$A_{\left[\begin{matrix}10M+3m-8 \,:\, 10M+3m-6\\ 3d-5 \quad:\quad 3d-3\end{matrix}\right]} = \frac{\partial}{\partial\overrightarrow{\Delta x_{1,d}}}\overrightarrow{\dot{\omega}_{m,B}} \quad\quad (A.21)$$

where *m* ranges from 1 to *M*, and *d* is again from 2 to *M*. This essentially makes $A_{d,a}$ a fully populated 3*M* x (3*M* -3) matrix. As only the first portion of Equation A.20 is dependent upon the position variables, the linearization of the angular acceleration is simply:

$$\frac{\partial}{\partial\overrightarrow{\Delta x_{1,d}}}\overrightarrow{T_{m,B}} = k\sum_{n=1}^{N}\sum_{b=1}^{N}\overrightarrow{r_{mn}}\times Q_m^T\frac{q_{mn}q_{db}}{|\overrightarrow{r_{db,mn}}|^3}\left[-I+3\frac{\overrightarrow{r_{db,mn}}\cdot\overrightarrow{r_{db,mn}}^T}{|\overrightarrow{r_{db,mn}}|^2}\right] \quad\quad (A.22)$$

$$\text{for } d = 2 \text{ to } M$$
$$d \neq m$$

and

$$\frac{\partial}{\partial\overrightarrow{\Delta x_{1,d}}}\overrightarrow{T_{d,B}} = k\sum_{n=1}^{N}\sum_{a=1}^{M}\sum_{b=1}^{N}\overrightarrow{r_{dn}}\times Q_d^T\frac{q_{dn}q_{ab}}{|\overrightarrow{r_{ab,dn}}|^3}\left[I-3\frac{\overrightarrow{r_{ab,dn}}\cdot\overrightarrow{r_{ab,dn}}^T}{|\overrightarrow{r_{ab,dn}}|^2}\right] \quad\quad (A.23)$$

$$a \neq m$$

$$\text{for } d = 2 \text{ to } M$$
$$d = m$$

pre-multiplied with inverse of the inertia matrix of the respective spacecraft.

The second entry in the row is obtained by taking the partial derivative of Equation A.20 with respect to the quaternion variables of each spacecraft. This $A_{d,b}$ entry is given by:

$$A_{\begin{bmatrix} 10M + 3m - 8 \; : \; 10M + 3m - 6 \\ 3M + 4d - 6 \; : \; 3M + 4d - 3 \end{bmatrix}} = \frac{\partial \overrightarrow{\dot{\omega}}_{m, B}}{\partial \overrightarrow{\varepsilon}_d} \tag{A.24}$$

which is a fully populated $3M$ x $4M$ matrix that comprises:

$$\frac{\partial}{\partial \overrightarrow{\varepsilon}_{f, d}} \overrightarrow{T}_{m, B} = k \sum_{n = 1}^{N} \sum_{b = 1}^{N} \overrightarrow{r}_{mn} \times Q_m^T \frac{q_{mn} q_{db}}{\left| \overrightarrow{r}_{db, mn} \right|^3} \left[-I + 3 \frac{\overrightarrow{r}_{db, mn} \cdot \overrightarrow{r}_{db, mn}^T}{\left| \overrightarrow{r}_{db, mn} \right|^2} \right] \frac{\partial}{\partial \overrightarrow{\varepsilon}_{f, d}} Q_d \cdot \overrightarrow{r}_{mN, mn} \tag{A.25}$$

$$\text{for } d = 1 \text{ to } M$$
$$d \neq m$$

and

$$\frac{\partial}{\partial \overrightarrow{\varepsilon}_{f, d}} \overrightarrow{T}_{d, B} = k \sum_{n = 1}^{N} \sum_{\substack{a = 1 \\ a \neq m}}^{M} \sum_{b = 1}^{N} \overrightarrow{r}_{dn} \frac{q_{dn} q_{ab}}{\left| \overrightarrow{r}_{ab, dn} \right|^3} \left\{ \frac{\partial}{\partial \overrightarrow{\varepsilon}_{f, d}} Q_d^T \cdot \overrightarrow{r}_{ab, dn} \right.$$

$$\left. + Q_d^T \left[I - 3 \frac{\overrightarrow{r}_{ab, dn} \cdot \overrightarrow{r}_{ab, dn}^T}{\left| \overrightarrow{r}_{ab, dn} \right|^2} \right] \frac{\partial}{\partial \overrightarrow{\varepsilon}_{f, d}} Q_d \cdot \overrightarrow{r}_{mN, mn} \right\}$$

$$\text{for } d = 1 \text{ to } M$$
$$d = m \tag{A.26}$$

where both the d and m indices range from 1 to M, respectively.

Finally, the last entry in the A matrix is obtained by taking the partial derivative with respect to the angular rates of the spacecraft. This $A_{d,d}$ entry corresponds to:

$$A_{\begin{bmatrix} 10M + 3m - 8 \; : \; 10M + 3m - 6 \\ 10M + 3d - 8 \; : \; 10M + 3d - 6 \end{bmatrix}} = \frac{\partial \overrightarrow{\dot{\omega}}_{m, B}}{\partial \overrightarrow{\omega}_{d, B}} \tag{A.27}$$

which comprises M 3 x 3 block diagonal matrices since the m-th angular accelerations are only functions of the m-th angular rates. The partial derivative of Equation A.20 is the derivative of the second portion of the equation with respect to the angular rates:

$$\frac{\partial}{\partial \overrightarrow{\omega}_d}(\overrightarrow{\omega}_d \times I_{p,\,d}\overrightarrow{\omega}_d) = \begin{bmatrix} 0 & (I_3 - I_2)\omega_3 & (I_3 - I_2)\omega_2 \\ (I_1 - I_3)\omega_3 & 0 & (I_1 - I_3)\omega_1 \\ (I_2 - I_1)\omega_2 & (I_2 - I_1)\omega_1 & 0 \end{bmatrix}_d \qquad \begin{array}{c} \text{for } d = 1 \text{ to } M \\ d = m \end{array} \qquad (\text{A.28})$$

pre-multiplied with the inverse of the corresponding inertia matrix. For the case when $d \neq m$, the partial derivative is simply a 3 x 3 zero matrix.

A.1.5 Differential Acceleration Entry (B matrix)

The entries in the **B** matrix are obtained in a similar way to the linearization used in obtaining the **A** matrix. In this case, the linearization is with respect to the control variables, which are the strengths of the charges. Similar to most control problems, the control variables occur in the equation of motion relationships. As such, the rows corresponding to the time derivative of the position and angular variables are simply zero.

The entries that correspond to the partial derivative of the differential acceleration with respect to the control variables, grouped in terms of the d-th spacecraft, are given by:

$$B_{\begin{bmatrix} 7M + 3m - 8 & : 7M + 3m - 6 \\ (N-1)(d-1) + 1 : & (N-1)d \end{bmatrix}} = \frac{\partial}{\partial \overrightarrow{u}_d}\overrightarrow{\Delta\ddot{x}}_{1,\,m} \qquad (\text{A.29})$$

where N - 1 control variables are assumed for each spacecraft, since Equation 5.56 must also be satisfied. The partial derivative of the force equation with respect to the d-th control vector is given by:

$$\frac{\partial}{\partial q_{f,d}}\overrightarrow{\mathrm{F}_m} = k\frac{\partial}{\partial q_{f,d}}\left[\sum_{\substack{n=1 \\ a\neq m}}^{N}\sum_{a=1}^{M}\sum_{b=1}^{N}\frac{q_{mn}q_{ab}}{\left|\overrightarrow{\mathrm{r}_{ab,mn}}\right|^3}\overrightarrow{\mathrm{r}_{ab,mn}}\right]$$

$$= k\frac{\partial}{\partial q_{f,d}}\left[\sum_{\substack{n=1 \\ a\neq m}}^{N}\sum_{a=1}^{M}q_{mn}\left(\sum_{b=1}^{N-1}\frac{q_{ab}}{\left|\overrightarrow{\mathrm{r}_{ab,mn}}\right|^3}\overrightarrow{\mathrm{r}_{ab,mn}} + \frac{q_{aN}}{\left|\overrightarrow{\mathrm{r}_{aN,mn}}\right|^3}\overrightarrow{\mathrm{r}_{aN,mn}}\right)\right]$$

$$= k\frac{\partial}{\partial q_{f,d}}\left[\sum_{\substack{n=1 \\ a\neq m}}^{N}\sum_{a=1}^{M}q_{mn}\left(\sum_{b=1}^{N-1}\frac{q_{ab}}{\left|\overrightarrow{\mathrm{r}_{ab,mn}}\right|^3}\overrightarrow{\mathrm{r}_{ab,mn}} - \sum_{b=1}^{N-1}\frac{q_{ab}}{\left|\overrightarrow{\mathrm{r}_{aN,mn}}\right|^3}\overrightarrow{\mathrm{r}_{aN,mn}}\right)\right] \quad\text{(A.30)}$$

$$= k\frac{\partial}{\partial q_{f,d}}\left[\sum_{\substack{n=1 \\ a\neq m}}^{N}\sum_{a=1}^{M}\sum_{b=1}^{N-1}q_{mn}q_{ab}\left(\frac{\overrightarrow{\mathrm{r}_{ab,mn}}}{\left|\overrightarrow{\mathrm{r}_{ab,mn}}\right|^3} - \frac{\overrightarrow{\mathrm{r}_{aN,mn}}}{\left|\overrightarrow{\mathrm{r}_{aN,mn}}\right|^3}\right)\right]$$

$$= k\sum_{n=1}^{N}q_{mn}\left[\frac{\overrightarrow{\mathrm{r}_{df,mn}}}{\left|\overrightarrow{\mathrm{r}_{df,mn}}\right|^3} - \frac{\overrightarrow{\mathrm{r}_{dN,mn}}}{\left|\overrightarrow{\mathrm{r}_{dN,mn}}\right|^3}\right]$$

where f ranges from 1 to N-1 and d ranges from 1 to M, while maintaining the $d\neq m$ condition. For the cases when $d = m$, the partial derivative is:

$$\frac{\partial}{\partial q_{f,d}}\overrightarrow{\mathrm{F}_d} = k\sum_{\substack{a=1 \\ a\neq d}}^{M}\sum_{b=1}^{N}q_{ab}\left[\frac{\overrightarrow{\mathrm{r}_{ab,df}}}{\left|\overrightarrow{\mathrm{r}_{ab,df}}\right|^3} - \frac{\overrightarrow{\mathrm{r}_{ab,dN}}}{\left|\overrightarrow{\mathrm{r}_{ab,dN}}\right|^3}\right] \qquad \begin{aligned} &\text{for } f = 1 \text{ to } N-1 \\ &\text{for } d = 1 \text{ to } M \\ &\qquad d = m \end{aligned} \quad\text{(A.31)}$$

In both these cases, m ranges from 2 to M, as there are only M - 1 equations of motion that describe the differential acceleration variables.

A.1.6 Angular Acceleration Entry (B Matrix)

The $\mathbf{B}_d$ entry in the $\mathbf{B}$ matrix is obtained by taking the partial derivative of the torque equation with respect to the control variables. The entries in the $\mathbf{B}$ matrix that correspond to this partial derivative are given by:

$$B_{\begin{bmatrix} 10M + 3m - 8 & : & 10M + 3m - 6 \\ (N-1)(d-1) + 1 & : & (N-1)d \end{bmatrix}} = \frac{\partial}{\partial \overrightarrow{\mathrm{u}}_d} \dot{\overrightarrow{\omega}}_{m, B} \tag{A.32}$$

where again only N - 1 control variables are accounted for each spacecraft. The partial derivative with respect to the control variables is given by:

$$\frac{\partial}{\partial q_{f, d}} \overrightarrow{\mathrm{T}}_{m, B} = k \sum_{n=1}^{N} q_{mn} \left[\overrightarrow{\mathrm{x}}_{mn} \times Q_m^T \frac{\overrightarrow{\mathrm{r}}_{df, mn}}{\left| \overrightarrow{\mathrm{r}}_{df, mn} \right|^3} - \overrightarrow{\mathrm{x}}_{mN} \times Q_m^T \frac{\overrightarrow{\mathrm{r}}_{dN, mn}}{\left| \overrightarrow{\mathrm{r}}_{dN, mn} \right|^3} \right] \tag{A.33}$$

$$\text{for } f = 1 \text{ to } N - 1$$
$$\text{for } d = 1 \text{ to } M$$
$$d \neq m$$

and

$$\frac{\partial}{\partial q_{f, d}} \overrightarrow{\mathrm{T}}_{d, B} = k \sum_{a=1}^{M} \sum_{b=1}^{N} q_{ab} \left[\overrightarrow{\mathrm{x}}_{df} \times Q_d^T \frac{\overrightarrow{\mathrm{r}}_{ab, df}}{\left| \overrightarrow{\mathrm{r}}_{ab, df} \right|^3} - \overrightarrow{\mathrm{x}}_{dN} \times Q_d^T \frac{\overrightarrow{\mathrm{r}}_{ab, dN}}{\left| \overrightarrow{\mathrm{r}}_{ab, dN} \right|^3} \right] \tag{A.34}$$

$$\text{for } f = 1 \text{ to } N - 1$$
$$\text{for } d = 1 \text{ to } M$$
$$d = m$$

where M torque equations are differentiated with respect to M (N - 1) control variables.

This concludes the derivation for both the $\mathbf{A}$ and $\mathbf{B}$ control matrices. In the next section, the Matlab code developed to implement these equations is presented. With these $\mathbf{A}$ and $\mathbf{B}$ matrices, control topologies for the spacecraft with differing pole configurations can be investigated. More specifically, controllability issues for these systems can be examined, as done in Chapter 5.

A.2 Matlab Code For A & B Matrices Generation

The corresponding Matlab function written to generate the control matrices using the equations derived in the previous section is presented here. This code is not optimized for compactness or speed, but is provided as a possible implementation of the derivations obtained in the previous section.

A.2.1 Inputs

The Matlab function is called using the command line *AB_3d_gen_func(XYZ,xyz,epsilon,w,I,msc,k)* where the inputs to the function are given by the variables in parentheses. The makeup of these input variables using a two spacecraft system, each with three poles (including center node), is further discussed in this section.

XYZ variable

The *XYZ* variable is a *M* x 3 matrix that provides the location of each spacecraft in the system's inertial reference frame. More specifically, each row provides the coordinates of the *N*-th node of a spacecraft in the inertial reference frame. Each column in the matrix corresponds to the ordinate of the spacecraft in the cartesian coordinate system. As an example, the entry for the two spacecraft dipole case analyzed in Section 5.4.4 is:

```
XYZ(1,:) = [-37.5  0  0];
XYZ(2,:) = [ 37.5  0  0];
```

xyz variable

The *xyz* variable is a three-dimensional *N* x 4 x *M* matrix that provides information regarding the poles of each spacecraft. Each row in the matrix corresponds to the information for a particular node, beginning with the location of that node written in the spacecraft cartesian coordinate system. The last row in the matrix (N^{th}) represents the center node of the spacecraft, which also corresponds to the origin of the spacecraft coordinate system. The fourth column in the matrix gives the strength of the poles. Note that the sum of the elements in this column must equate to zero since Equation 5.56 must be satisfied. The third dimension of the matrix corresponds to the two dimensional matrices for the respective spacecraft. The *xyz* input for the two spacecraft with the dipoles aligned along the spacecraft's *x*-axis is given by:

```
xyz(:,:,1) = [.2135 0 0 24255; -.2135 0 0 -24255; 0 0 0 0];
xyz(:,:,2) = [.2135 0 0 24255; -.2135 0 0 -24255; 0 0 0 0];
```

epsilon variable

The *epsilon* variable gives the attitude orientation of all the spacecraft in the system. It is a *M* x 4 matrix with the rows representing information pertaining to the different spacecraft. Since a quaternion representation is used, four columns are required. In the case where both the space-craft's coordinate systems are aligned with the inertial coordinate system, the entry is given by:

```
epsilon(1,:) = [0 0 1 0];
epsilon(2,:) = [0 0 1 0];
```

w variable

The *w* variable is a *M* x 3 matrix that describes the angular rate of each spacecraft in its respective body coordinate system. For the example considered in Section 5.4.4, the angular rate input is given by:

```
w(1,:) = [0 0 0];
w(2,:) = [0 0 0];
```

I variable

The *I* variable is a *M* x 3 matrix that provides the principal mass moment of inertia of each space-craft. To simplify the mathematics, it is assumed that the body coordinate system of each space-craft is aligned with the axes of these principal moments of inertia. For the two spacecraft example, the spacecraft are each approximated to fill a two meter-cubed volume. As such, the mass moment of inertia in each axis is simply $\frac{2}{3}m_{sc}$ and the *I* entry is given by:

```
I(1,:) = [414 414 414];
I(2,:) = [414 414 414];
```

msc variable

The *msc* variable is a *M* x 1 vector that lists the masses of the spacecraft. For the two spacecraft TPF example, the mass entry is simply:

```
msc(1,1) = [621];
msc(2,1) = [621];
```

k variable

The *k* variable corresponds to the conversion factor that arises from the use of electric poles to model the magnetic poles. From Equation 5.10, the *k* variable for the example considered here is:

```
k = 1.0217e-005;
```

A.2.2 Outputs

The outputs from the Matlab *AB_3d_gen_func* are the **A** and B control matrices. The A matrix corresponds to the dynamic matrix and is a size 13*M* - 6 square matrix. The B matrix is a 13*M* - 6 x *M*(*N* - 1) matrix, with each column corresponding to a control variable in the system.

A.2.3 Matlab Code

```
function [A,B] = AB_3d_gen_func(XYZ,xyz,epsilon,w,I,msc,k);

%    Function AB_3d_gen_func
%
%    Program written to generate A and B matrices
%    using quaternions to describe the spacecraft's attitude
%
%    Written by Edmund Kong
%
%    State vector is ordered by:
%    {dx12 dy12 dz12 dx13 dy13 dz13 .... dx1M dy1M dz1M e11 e12 e13 e14
%     e21 e22 e23 e24 ... eM1 eM2 eM3 eM4 dx12dot dy12dot dz12dot ...
%     dx1Mdot dy1Mdot dz1mdot w11 w12 w13 .... wM1 wM2 wM3}
%
%    dx1d - delta x from spacecraft 1 to spacecraft d
%    edf - spacecraft d quaternion f (f: 1 to 4)
%    dx1ddot - velocity component of dx1d
%    w - angular velocity in body coordinates
%
%    N - number of poles per spacecraft (includes center of spacecraft)
%    M - number of spacecraft in the array
%
%    Hence total number of states is 13M-6
%    3M-3 position states
%    4M quaternion states
%    3M-3 velocity states
%    3M angular velocity states
%
%    Inputs
%    I - principal inertia matrix - M x 3 matrix
%    XYZ - XYZ location of spacecraft IRF M x 3 matrix
%    xyz - location and charge of poles in body coordinates - N x xyz x M
%        - N - pole #, xyz - location - fourth column is charge, M - order of s/c
%        - N-th pole is zero location - center of s/c
%    epsilon - spacecraft attitude in quaternion - M x 4 matrix
%    msc - mass of spacecraft 1 x M matrix
%    w - spacecraft angular rate - M x 3 matrix
%    k - electric charge to magnetic charge conversion
%

[N,O,M] = size(xyz);  %   M - number of spacecraft

%    Generate A matrix
A = zeros(13*M-6);
A(1:3*(M-1),7*M-2:10*M-6) = eye(3*M-3);

%    Consider differentiation of F1 wrt to states  % m = 1
xyz1m = zeros(3,1);
delm = zeros(3,4);
[Qm,dQdel1m,dQdel2m,dQdel3m,dQdel4m] = quat_ret(epsilon(1,1:4));

%    Diffential wrt diffential xyz & quaternions
for dcount = 2:M
    xyz1d = XYZ(dcount,:)' - XYZ(1,:)';
    [Qd,dQdel1d,dQdel2d,dQdel3d,dQdel4d] = quat_ret(epsilon(dcount,1:4));
    dx = 0;
    del = zeros(3,4);
    for ncount = 1:N
        rmn = xyz(ncount,1:3,1)';
        qmn = xyz(ncount,4,1);
        for bcount = 1:N
```

```
            rdb = xyz(bcount,1:3,dcount)';
            qdb = xyz(bcount,4,dcount);
            rdbmn = xyz1m - xyz1d + Qm*rmn - Qd*rdb;
            rdbmnmag = sqrt(sum(rdbmn.^2));
            dTdx = (eye(3) - 3*rdbmn*rdbmn'/rdbmnmag^2)*qdb*qmn/rdbmnmag^3;
            dx = dx - dTdx;
            del(:,1) = del(:,1) - dTdx*dQdel1d*rdb;
            del(:,2) = del(:,2) - dTdx*dQdel2d*rdb;
            del(:,3) = del(:,3) - dTdx*dQdel3d*rdb;
            del(:,4) = del(:,4) - dTdx*dQdel4d*rdb;
            delm(:,1) = delm(:,1) + dTdx*dQdel1m*rmn;
            delm(:,2) = delm(:,2) + dTdx*dQdel2m*rmn;
            delm(:,3) = delm(:,3) + dTdx*dQdel3m*rmn;
            delm(:,4) = delm(:,4) + dTdx*dQdel4m*rmn;
        end
    end
    dF1(1:3,(dcount-2)*3+[1:3]) = dx;
    dF1(1:3,3*(M-1)+(dcount-1)*4+[1:4]) = del;
end
dF1(1:3,3*(M-1)+[1:4]) = delm;

%   Filling in the A matrix
for dcount = 1:M
    xyz1d = XYZ(dcount,:)' - XYZ(1,:)';
    dxd = zeros(3);
    deld = zeros(3,4);
    dTxd = zeros(3);
    dTdeld = zeros(3,4);
    [Qd,dQdel1d,dQdel2d,dQdel3d,dQdel4d,dedw] = quat_ret(epsilon(dcount,1:4));
    Imat = zeros(3);
    Imat(1,1) = I(dcount,1);
    Imat(2,2) = I(dcount,2);
    Imat(3,3) = I(dcount,3);
    for acount = 1:M
        if (acount~=dcount)
            dxa = zeros(3);
            del = zeros(3,4);
            dTxa = zeros(3);
            dTdela = zeros(3,4);
            xyz1a = XYZ(acount,:)' - XYZ(1,:)';
            [Qa,dQdel1a,dQdel2a,dQdel3a,dQdel4a] = quat_ret(epsilon(acount,1:4));
            for ncount = 1:N
                rdn = xyz(ncount,1:3,dcount)';
                qdn = xyz(ncount,4,dcount);
                for bcount = 1:N
                    rab = xyz(bcount,1:3,acount)';
                    qab = xyz(bcount,4,acount);
                    rabdn = xyz1d - xyz1a + Qd*rdn - Qa*rab;
                    rabdnmag = sqrt(sum(rabdn.^2));

                    dTdx = (eye(3) - 3*rabdn*rabdn'/rabdnmag^2)*qab*qdn/rabdnmag^3;
                    at = Qd'*dTdx;

                    if (dcount~=1)
                        if (acount~=1)
                            dxa = dxa - dTdx;
                        end
                        dxd = dxd + dTdx;
                        del(:,1) = del(:,1) - dTdx*dQdel1a*rab;
                        del(:,2) = del(:,2) - dTdx*dQdel2a*rab;
                        del(:,3) = del(:,3) - dTdx*dQdel3a*rab;
                        del(:,4) = del(:,4) - dTdx*dQdel4a*rab;
                        deld(:,1) = deld(:,1) + dTdx*dQdel1d*rdn;
                        deld(:,2) = deld(:,2) + dTdx*dQdel2d*rdn;
                        deld(:,3) = deld(:,3) + dTdx*dQdel3d*rdn;
                        deld(:,4) = deld(:,4) + dTdx*dQdel4d*rdn;
                        dTxd(:,1) = dTxd(:,1) + cross(rdn,at(:,1));
                        dTxd(:,2) = dTxd(:,2) + cross(rdn,at(:,2));
                        dTxd(:,3) = dTxd(:,3) + cross(rdn,at(:,3));
                    end
                    if (acount~=1)
                        dTxa(:,1) = dTxa(:,1) - cross(rdn,at(:,1));
                        dTxa(:,2) = dTxa(:,2) - cross(rdn,at(:,2));
                        dTxa(:,3) = dTxa(:,3) - cross(rdn,at(:,3));
                    end
                    dTdela(:,1) = dTdela(:,1) - cross(rdn,at*dQdel1a*rab);
```

```
                    dTdela(:,2) = dTdela(:,2) - cross(rdn,at*dQdel2a*rab);
                    dTdela(:,3) = dTdela(:,3) - cross(rdn,at*dQdel3a*rab);
                    dTdela(:,4) = dTdela(:,4) - cross(rdn,at*dQdel4a*rab);
                    at2 = qab*qdn/rabdnmag^3*dQdel1d'*rabdn + at*dQdel1d*rdn;
                    dTdeld(:,1) = dTdeld(:,1) + cross(rdn,at2);
                    at2 = qab*qdn/rabdnmag^3*dQdel2d'*rabdn + at*dQdel2d*rdn;
                    dTdeld(:,2) = dTdeld(:,2) + cross(rdn,at2);
                    at2 = qab*qdn/rabdnmag^3*dQdel3d'*rabdn + at*dQdel3d*rdn;
                    dTdeld(:,3) = dTdeld(:,3) + cross(rdn,at2);
                    at2 = qab*qdn/rabdnmag^3*dQdel4d'*rabdn + at*dQdel4d*rdn;
                    dTdeld(:,4) = dTdeld(:,4) + cross(rdn,at2);
                end
            end
            if dcount~=1
                if acount~=1
                    A((dcount-2)*3+7*M-3+[1:3],3*(acount-2)+[1:3]) = ...
                        dxa/msc(dcount) - dF1(1:3,(acount-2)*3+[1:3])/msc(1);
                end
                A((dcount-2)*3+7*M-3+[1:3],4*(acount-1)+3*M-3+[1:4]) = ...
                    del/msc(dcount) - dF1(1:3,(acount-1)*4+3*M-3+[1:4])/msc(1);
            end
            if acount~=1
                A((dcount-1)*3+10*M-6+[1:3],3*(acount-2)+[1:3]) = inv(Imat)*dTxa;
            end
            A((dcount-1)*3+10*M-6+[1:3],4*(acount-1)+[1:4]+3*M-3) = inv(Imat)*dTdela;
        end
    end
    if (dcount~=1)
        A((dcount-2)*3+7*M-3+[1:3],(dcount-2)*3+[1:3]) = dxd/msc(dcount) - ...
            dF1(1:3,(dcount-2)*3+[1:3])/msc(1);
        A((dcount-2)*3+7*M-3+[1:3],4*(dcount-1)+3*M-3+[1:4]) = deld/msc(dcount) ...
            - dF1(1:3,4*(dcount-1)+3*M-3+[1:4])/msc(1);
        A((dcount-1)*3+10*M-6+[1:3],(dcount-2)*3+[1:3]) = inv(Imat)*dTxd;
    end
    A(10*M-6+[1:3]+3*(dcount-1),3*M-3+[1:4]+4*(dcount-1)) = inv(Imat)*dTdeld;

    ddwd(1,:) = (I(dcount,3)-I(dcount,2))*[0 w(dcount,3) w(dcount,2)];
    ddwd(2,:) = (I(dcount,1)-I(dcount,3))*[w(dcount,3) 0 w(dcount,1)];
    ddwd(3,:) = (I(dcount,2)-I(dcount,1))*[w(dcount,2) w(dcount,1) 0];
    A(10*M-6+[1:3]+3*(dcount-1),10*M-6+[1:3]+3*(dcount-1)) = -inv(Imat)*ddwd;

    dede(1,:) = [0 w(dcount,3) -w(dcount,2) w(dcount,1)];
    dede(2,:) = [-w(dcount,3) 0 w(dcount,1) w(dcount,2)];
    dede(3,:) = [w(dcount,2) -w(dcount,1) 0 w(dcount,3)];
    dede(4,:) = [-w(dcount,1) -w(dcount,2) -w(dcount,3) 0];
    A(3*M-3+[1:4]+4*(dcount-1),3*M-3+[1:4]+(dcount-1)*4) = 1/2*dede;

    A(3*M-3+[1:4]+4*(dcount-1),10*M-6+[1:3]+3*(dcount-1)) = 1/2*dedw;
end
A(7*M-2:13*M-6,1:7*M-3) = k*A(7*M-2:13*M-6,1:7*M-3);

%   Generating B matrix
B = zeros(13*M-6,(N-1)*M);

%   Generate with respect to M = 1
%   for m = d = 1
[Qd] = quat_ret(epsilon(1,1:4));
xyz1d = zeros(3,1);
rdN = xyz(N,1:3,1)';
for ncount = 1:N-1
    rdn = xyz(ncount,1:3,1)';
    dFBdd = 0;
    for acount = 2:M
        xyz1a = XYZ(acount,:)' - XYZ(1,:)';
        [Qa] = quat_ret(epsilon(acount,1:4));
        raN = xyz(N,1:3,acount)';
        raNdn = xyz1d - xyz1a + Qd*rdn - Qa*raN;
        raNdnmag = sqrt(sum(raNdn.^2));
        raNdN = xyz1d - xyz1a + Qd*rdN - Qa*raN;
        raNdNmag = sqrt(sum(raNdN.^2));
        for bcount = 1:N-1
            rab = xyz(bcount,1:3,acount)';
            qab = xyz(bcount,4,acount);
            rabdN = xyz1d - xyz1a + Qd*rdN - Qa*rab;
            rabdn = xyz1d - xyz1a + Qd*rdn - Qa*rab;
            rabdNmag = sqrt(sum(rabdN.^2));
```

```
                rabdnmag = sqrt(sum(rabdn.^2));
                dFBdd = dFBdd + qab*(rabdn/rabdnmag^3 - rabdN/rabdNmag^3 - ...
                    raNdn/raNdnmag^3 + raNdN/raNdNmag^3);
            end
        end
        dF1B(1:3,ncount) = dFBdd;
end

%   for m ~= d
[Qd] = quat_ret(epsilon(1,1:4));
xyz1d = zeros(3,1);
rdN = xyz(N,1:3,1)';
for acount = 2:M
    xyz1a = XYZ(acount,:)' - XYZ(1,:)';
    [Qa] = quat_ret(epsilon(acount,1:4));
    raN = xyz(N,1:3,acount)';
    raNdN = xyz1d - xyz1a + Qd*rdN - Qa*raN;
    raNdNmag = sqrt(sum(raNdN.^2));
    for bcount = 1:N-1
        rab = xyz(bcount,1:3,acount)';
        qab = xyz(bcount,4,acount);
        dFBdd = 0;
        rabdN = xyz1d - xyz1a + Qd*rdN - Qa*rab;
        rabdNmag = sqrt(sum(rabdN.^2));
        for ncount = 1:N-1
            rdn = xyz(ncount,1:3,1)';
            qdn = xyz(ncount,4,1);
            raNdn = xyz1d - xyz1a + Qd*rdn - Qa*raN;
            rabdn = xyz1d - xyz1a + Qd*rdn - Qa*rab;
            raNdnmag = sqrt(sum(raNdn.^2));
            rabdnmag = sqrt(sum(rabdn.^2));
            dFBdd = dFBdd + qdn*(rabdn/rabdnmag^3 - rabdN/rabdNmag^3 - ...
                raNdn/raNdnmag^3 + raNdN/raNdNmag^3);
        end
        dF1B(1:3,(N-1)*(acount-1)+bcount) = dFBdd;
    end
end

%   Filling in B matrix
for dcount = 1:M
    [Qd] = quat_ret(epsilon(dcount,1:4));
    xyz1d = XYZ(dcount,:)' - XYZ(1,:)';
    rdN = xyz(N,1:3,dcount)';
    Imat = zeros(3);
    Imat(1,1) = I(dcount,1);
    Imat(2,2) = I(dcount,2);
    Imat(3,3) = I(dcount,3);
    for ncount = 1:N-1
        rdn = xyz(ncount,1:3,dcount)';
        dFBdd = 0;
        dTBdd = 0;
        for acount = 1:M
            if acount~= dcount
                xyz1a = XYZ(acount,:)' - XYZ(1,:)';
                [Qa] = quat_ret(epsilon(acount,1:4));
                raN = xyz(N,1:3,acount)';
                raNdn = xyz1d - xyz1a + Qd*rdn - Qa*raN;
                raNdnmag = sqrt(sum(raNdn.^2));
                raNdN = xyz1d - xyz1a + Qd*rdN - Qa*raN;
                raNdNmag = sqrt(sum(raNdN.^2));
                for bcount = 1:N-1
                    rab = xyz(bcount,1:3,acount)';
                    qab = xyz(bcount,4,acount);
                    rabdN = xyz1d - xyz1a + Qd*rdN - Qa*rab;
                    rabdn = xyz1d - xyz1a + Qd*rdn - Qa*rab;
                    rabdNmag = sqrt(sum(rabdN.^2));
                    rabdnmag = sqrt(sum(rabdn.^2));
                      dTBdd = dTBdd + qab*(cross(rdn,Qd'*(rabdn/rabdnmag^3 - raNdn...
                    /raNdnmag^3)) + cross(rdN,Qd'*(raNdN/raNdNmag^3-rabdN/rabdNmag^3)));
                        if dcount~= 1
                            dFBdd = dFBdd + qab*(rabdn/rabdnmag^3 - rabdN/rabdNmag^3...
                            - raNdn/raNdnmag^3 + raNdN/raNdNmag^3);
                        end
                end
            end
        end
    end
```

```
        if dcount~= 1
            B(7*M-3+3*(dcount-2)+[1:3],(N-1)*(dcount-1)+ncount) = ...
                dFBdd/msc(dcount) - dF1B(1:3,(N-1)*(dcount-1)+ncount)/msc(dcount);
        end
        B(10*M-6+3*(dcount-1)+[1:3],(N-1)*(dcount-1)+ncount) = inv(Imat)*dTBdd;
    end
end
B = k*B;

for dcount = 1:M
    [Qd] = quat_ret(epsilon(dcount,1:4));
    xyz1d = XYZ(dcount,:)' - XYZ(1,:)';
    rdN = xyz(N,1:3,dcount)';
    Imat = zeros(3);
    Imat(1,1) = I(dcount,1);
    Imat(2,2) = I(dcount,2);
    Imat(3,3) = I(dcount,3);
    for acount = 1:M
        if acount~=dcount
            xyz1a = XYZ(acount,:)' - XYZ(1,:)';
            [Qa] = quat_ret(epsilon(acount,1:4));
            raN = xyz(N,1:3,acount)';
            raNdN = xyz1d - xyz1a + Qd*rdN - Qa*raN;
            raNdNmag = sqrt(sum(raNdN.^2));
            for bcount = 1:N-1
                rab = xyz(bcount,1:3,acount)';
                dFBdd = 0;
                dTBdd = 0;
                rabdN = xyz1d - xyz1a + Qd*rdN - Qa*rab;
                rabdNmag = sqrt(sum(rabdN.^2));
                for ncount = 1:N-1
                    rdn = xyz(ncount,1:3,dcount)';
                    qdn = xyz(ncount,4,dcount);
                    raNdn = xyz1d - xyz1a + Qd*rdn - Qa*raN;
                    rabdn = xyz1d - xyz1a + Qd*rdn - Qa*rab;
                    raNdnmag = sqrt(sum(raNdn.^2));
                    rabdnmag = sqrt(sum(rabdn.^2));
                    dTBdd = dTBdd + qdn*(cross(rdn,Qd'*(rabdn/rabdnmag^3-raNdn/...
                    raNdnmag^3)) + cross(rdN,Qd'*(raNdN/raNdNmag^3-rabdN/rabdNmag^3)));
                    if dcount~= 1
                        dFBdd = dFBdd + qdn*(rabdn/rabdnmag^3 - rabdN/rabdNmag^3 ...
                            - raNdn/raNdnmag^3 + raNdN/raNdNmag^3);
                    end
                end
                if dcount~= 1
                    B(7*M-3+3*(dcount-2)+[1:3],(acount-1)*(N-1)+bcount) = ...
                        dFBdd/msc(dcount)- dF1B(1:3,(acount-1)*(N-1)+bcount)/msc(dcount);
                end
              B(10*M-6+3*(dcount-1)+[1:3],(acount-1)*(N-1)+bcount) = inv(Imat)*dTBdd;
            end
        end
    end
end


% ------------------------------------------------------------------------------------------------------------
%
function [Qd,dQdel1d,dQdel2d,dQdel3d,dQdel4d,dedw] = quat_ret(epsilon)

%   Function written to return the quaternion related variables needed to
%   calculate the A and B matrices
%
%   Written by Edmund Kong
%   Created on 30th November 2001
%
%   Inputs
%   epsilon - quaternion values of the d-th spacecraft (1x4 matrix)
%
%   Outputs
%   dQdel#d - #:1 to 4 - partial derivative of Q wrt quaternion variables
%           - 4 3x3 matrices
%   Qd - quaternion rotation matrix

%
e1d = epsilon(1);
e2d = epsilon(2);
```

```
e3d = epsilon(3);
e4d = epsilon(4);

dQdel1d = 2*[e1d e2d e3d;e2d -e1d -e4d;e3d e4d -e1d];
dQdel2d = 2*[-e2d e1d e4d; e1d e2d e3d; -e4d e3d -e2d];
dQdel3d = 2*[-e3d -e4d e1d; e4d -e3d e2d; e1d e2d e3d];
dQdel4d = 2*[e4d -e3d e2d; e3d e4d -e1d; -e2d e1d e4d];

Qd(1,1:3) = [e1d^2-e2d^2-e3d^2+e4d^2, 2*(e1d*e2d-e3d*e4d), 2*(e1d*e3d+e2d*e4d)];
Qd(2,1:3) = [2*(e1d*e2d+e3d*e4d), -e1d^2+e2d^2-e3d^2+e4d^2, 2*(e2d*e3d-e1d*e4d)];
Qd(3,1:3) = [2*(e1d*e3d-e2d*e4d), 2*(e2d*e3d+e1d*e4d), -e1d^2-e2d^2+e3d^2+e4d^2];

dedw = [e4d -e3d e2d; e3d e4d -e1d; -e2d e1d e4d; -e1d -e2d -e3d];
```